Graduate School ETD Form 9
(Revised 01/14)

PURDUE UNIVERSITY
GRADUATE SCHOOL
Thesis/Dissertation Acceptance

This is to certify that the thesis/dissertation prepared

By Clinton Edward Thompson

Entitled
Quantum Physics Inspired Optical Effects in Evanescently Coupled Waveguides

For the degree of Doctor of Philosophy

Is approved by the final examining committee:

Dr. Gautam Vemuri

Dr. Ricardo Decca

Dr. Yogesh Joglekar

Dr. Zhe-Yu Ou

Dr. David Nolte

To the best of my knowledge and as understood by the student in the *Thesis/Dissertation Agreement. Publication Delay, and Certification/Disclaimer (Graduate School Form 32)*, this thesis/dissertation adheres to the provisions of Purdue University's "Policy on Integrity in Research" and the use of copyrighted material.

Dr. Gautam Vemuri

Approved by Major Professor(s): _____

Approved by: Dr. Ricardo Decca 04/15/2014

Head of the Department Graduate Program Date

QUANTUM PHYSICS INSPIRED OPTICAL EFFECTS IN EVANESCENTLY COUPLED WAVEGUIDES

A Dissertation

Submitted to the Faculty

of

Purdue University

by

Clinton Edward Thompson

In Partial Fulfillment of the

Requirements for the Degree

of

Doctor of Philosophy

May 2014

Purdue University

West Lafayette, Indiana

To Cassie, the love of my life

ACKNOWLEDGMENTS

First and foremost, I wish to thank my advisor Dr. Gautam Vemuri. His door has always been open to me and has always taken the time to answer my questions the best he can.

I would also like to thank Dr. Yogesh Joglekar for not only taking the time to serve on my committee but also for providing insight and advice when my results were not easily interpretable.

I feel privileged to have had the opportunity to work with both of them.

I would also like to thank Dr. Ricardo Decca and Dr. Jeff Ou for serving on my committee. I also must thank Dr. David Nolte for being on my committee and making the drive from West Lafayette.

Finally, I would like to thank Jeff Carvell and Steve Carpenter for being the best friends a guy could have.

TABLE OF CONTENTS

LIST OF FIGURES

Figure Page

Figure Page

Figure Page

ABSTRACT

Thompson, Clinton Edward Ph.D., Purdue University, May 2014. Quantum Physics Inspired Optical Effects in Evanescently Coupled Waveguides . Major Professor: Gautam Vemuri.

The tight-binding model that has been used for many years in condensed matter physics, due to its analytic and numerical tractability, has recently been used to describe light propagating through an array of evanescently coupled waveguides. This dissertation presents analytic and numerical simulation results of light propagating in a waveguide array. The first result presented is that photonic transport can be achieved in an array where the propagation constant is linearly increasing across the array. For an input at the center waveguide, the breathing modes of the system are observed, while for a phase displaced, asymmetric input, phase-controlled photonic transport is predicted. For an array with a waveguide-dependent, parity-symmetric coupling constant, the wave packet dynamics are predicted to be tunable. In addition to modifying the propagation constant, the coupling between waveguides can also be modified, and the quantum correlations are sensitive to the form of the tunneling function.

In addition to modifying the waveguide array parameters in a structured manner, they can be randomized as to mimic the insertion of impurities during the fabrication process. When the refractive indices are randomized and real, the amount of light that localizes to the initial waveguide is found to be dependent on the initial waveguide when the waveguide coupling is non-uniform. In addition, when the variance of the refractive indices is small, light localizes in the initial waveguide as well as the parity-symmetric waveguide. In addition to real valued disorder, complex valued disorder can be introduced into the array through the imaginary component of the refractive

index. It is shown that the two-particle correlation function is qualitatively similar to the case when the waveguide coupling is real and random, as both cases preserve the symmetry of the eigenvalues. Lastly, different input fields have been used to investigate the quantum statistical aspects of Anderson localization. It is found that the fluctuations in the output intensity are enhanced and the entropy of the system is reduced when disorder is present in the waveguides.

1. INTRODUCTION

The tight-binding model has been used extensively in condensed matter physics since its introduction in 1954, due to its numerical and analytical tractability [1]. It assumes that the electron is tightly bound to an atom on the lattice and has limited interactions with the surrounding atoms through tunneling from atom to atom [2]. In recent years, arrays of evanescently coupled waveguides have become a paradigm for the realization of the one-dimensional tight-binding model. Historically, light and matter have been considered two different entities. The use of a condensed matter model to describe light is a result of the advent of technology that is used to fabricate the waveguides. The propagation constant is determined by the height and the width of the waveguide while distance between the centers of adjacent waveguides determine the coupling constant. The on-site potential for the particle is analogous to the propagation constant and the tunneling amplitude is analogous the coupling constant for light.

One process that is used to fabricate the waveguides is the use of molecular beam epitaxy. It works by depositing mono-atomic layers of atoms onto a substrate until a desired thickness of the material is achieved. The composition of the material is altered, as the material is deposited in such a manner as to form three distinct layers as shown in Figure 1.1. Experimentally, aluminum gallium arsenide has been used for the waveguides as 1.5 microns is below half the band gap of the middle layer that has 18% aluminum and additionally, this minimizes the loss of light. The bottom layer is the thickest, as it prevents light from interacting with the substrate on which the material is deposited. Another experimental consideration is the application of a capping layer of gallium arsenide to prevent the array from oxidizing. The shape of the waveguides are created during the lithography and etching process [3].

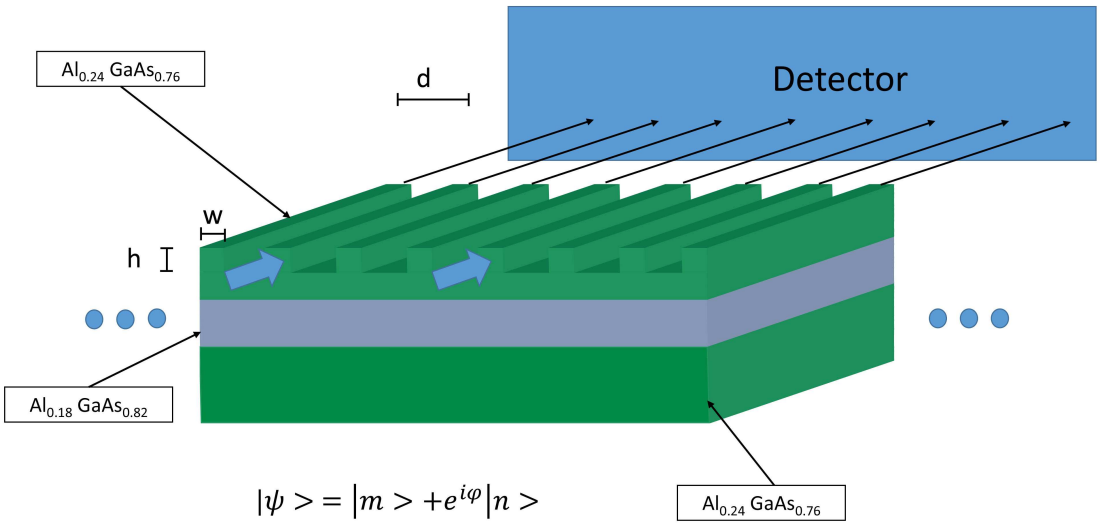

Fig. 1.1. Schematic of an array of evanescently coupled optical waveguides. The array is typically comprised of three layers that are deposited via molecular beam epitaxy. This allows mono-atomic control of the thickness in addition to the relative composition of each layer. The propagation constant, β_j, is determined by the height h and the width w of the waveguide while distance d between the centers of adjacent waveguides determine the coupling constant, C_j. The speed along a particular waveguide is constant as the index of refraction is time invariant when the intensity of the input light is sufficiently low enough that nonlinear effects are fully suppressed. The on-site potential for the particle is analogous to the propagation constant and the tunneling amplitude is analogous the coupling constant for light. The arrows represent the input at waveguides m and n, where the relative phase between the two inputs is φ.

As a result of having full control over the experimental parameters, the light propagating along a single waveguide can be described by the paraxial approximation of the Helmholtz equation and the coupling between adjacent waveguides can be described using coupled mode theory [4]. The longitudinal component of the paraxial equation that describes the spatial evolution of light propagating through an array of single-mode evanescently coupled waveguides is

$$i\frac{dE_j}{dz} = \beta_j E_j + C_j(E_{j+1} + E_{j-1}) \tag{1.1}$$

where E_j is the complex magnitude of the electric field in the j^{th} waveguide, β_j is the propagation constant, and C_j is the coupling constant between waveguides j and $j+1$. Note that both β_j and C_j are determined by the geometry a single waveguide as

$$\beta_j = \sqrt{\left(\frac{\omega}{c}\right)^2 - k_j^2} \tag{1.2}$$

and

$$C_j = (n_{j+1}^2 - n_b^2)\frac{k_0^2}{2\beta_j}\int\int u_{j+1}(x,y)u_j(x,y)dxdy \tag{1.3}$$

where ω is the angular frequency of the incident light, c is the speed of light in vacuum, u_j is the cross-sectional profile for the electric field in waveguide j, and k_j is the cutoff wavenumber in the waveguide that characterizes the propagating mode [5, 6]. Note that n_{j+1} and n_b are refractive indices for waveguide $j+1$ and the barrier between adjacent waveguides, respectively.

The tight-binding Hamiltonian, in secod quantized form, that describes the time evolution of a a particle on a lattice is [2]

$$H = \hbar\sum_{j=1}^{N}\left[V_j a_j^\dagger a_j + T_j(a_{j+1}^\dagger a_j + a_j^\dagger a_{j+1})\right] \tag{1.4}$$

where V_j is the on-site potential, T_j is the tunneling amplitude between sites j and $j+1$, and $a_j^\dagger$ (a_j) is the creation (annihilation) operator for the j^{th} site. The Heisenberg equation, which describes the evolution of the particle's wavefunction, is

$$i\frac{da_j}{dt} = [a_j, H] = V_j a_j + T_j(a_{j+1} + a_{j-1}) \tag{1.5}$$

and is isomorphic to Eq. (1.1) where the coupling, C_j, for light is analogous to the particle tunneling, T_j, while the propagation constant, β_j, is analogous to the on-site potential, V_j. As a result of this isomorphism, one can observe quantum and condensed matter phenomena in a fully classical system as the intensity distribution, $I_j = |E_j|^2$, is identical to probability distribution $P_j = a_j^\dagger a_j$.

One advantage to using light is that the intensity distribution can be measured directly while probability distribution of a particle on a lattice is measured indirectly, typically through the conductance of the material [7]. Another advantage is that the phenomena can be observed over a length of a few centimeters for light instead of a few microns for electrons [8]. Silberberg and co-workers have shown that adjusting the incident angle of the input light controls the diffraction of the light in the array, and this allows for a diffractionless array [3]. In addition, photons do not have a Coulomb interaction and the decoherence noise in the arrays is negligible [9]. For an electron on a tight-binding lattice, the system would need to be as cold as possible to ensure that the decoherence time from the phonons is maximized [7]. Additionally, one can sample the entire energy band using photons, as a photon injected into a single waveguide can be described by a linear combination of all the energy eigenstates. However, for electrons, only the electrons with energies near the Fermi energy can be sampled as they are easiest to promote (demote) from the valance (conduction) band to the conduction (valance) band [10]. Lastly, waveguide arrays allow for the investigation of boundary effects as the number of waveguides in an array $N \lesssim 100$ wheress for an electron on a lattice, the number of lattice sites is $N > 10^9$ [2].

Waveguide arrays can also be used to explore wave packet dynamics that are described by Hamiltonians that are non-Hermitian but $\mathcal{PT}$-symmetric. Traditionally, it has been thought that for the Hamiltonian to describe a quantum mechanical system, it has to be Hermitian, as it guarantees both real eigenvalues and probability conservation. However, Bender and co-workers have shown that for real eigenvalues, the Hamiltonian does not necessarily have to be Hermitian, provided it is $\mathcal{PT}$-symmetric [11]. The parity operator $\mathcal{P}$ performs a parity inversion, $(\mathbf{r}, \mathbf{p}) \to (-\mathbf{r}, -\mathbf{p})$

and if $H(\mathbf{r},\mathbf{p}) = H(-\mathbf{r},-\mathbf{p})$, the Hamiltonian is parity-symmetric. Note that $\mathbf{r}$ is the position vector and $\mathbf{p}$ is the momentum vector. The time-reversal operator, $\mathcal{T}$, reverses the motion of a particle, $\mathbf{r}(t) \rightarrow \mathbf{r}(-t)$ and $\mathbf{p}(t) \rightarrow -\mathbf{p}(-t)$. Applying the time-reversal operator to a Hamiltonian H results in $H(\mathbf{r},\mathbf{p}) \rightarrow H^*(\mathbf{r},-\mathbf{p})$ as the time-reversal operator also changes sign of the complex part of the Hamiltonian [12]. They have shown that as long as a Hamiltonian remains unchanged after applying both $\mathcal{P}$ and $\mathcal{T}$ operators, it can have real eigenvalues [13].When the eigenvalues become complex, the $\mathcal{PT}$-symmetric phase breaks and this has been experimentally observed in waveguide arrays.

This non-Hermiticity is introduced through gain and loss that can be experimentally accessed through the imaginary component of the index of refraction. The imaginary component of the propagation constant is then $\mathrm{Im}[\beta_j] = i\gamma_j$ where positive (negative) values of γ_j correspond to gain (loss), respectively. To maintain the $\mathcal{PT}$-symmetry, the gain and loss has to be balanced in the array and the gain has to be below the $\mathcal{PT}$-symmetric threshold, $|\gamma_j| < \gamma_c$. Guo and co-workers have been able to achieve this by using a two-channel array comprised of aluminum gallium arsenide with chromium deposited on one of the waveguides. The use of chromium introduces loss into the waveguide on which it was deposited, and results in an array with loss in one channel while the other channel remains unchanged. As this is an unbalanced system in terms of gain and loss, they have noticed that more light went to the unchanged waveguide when the rate of loss was increased [14]. Rüter and co-workers have been able to achieve a two-channel array where the gain and loss is balanced, using iron doped lithium niobate where the loss is introduced in one channel through the iron, and the gain is introduced by pumping the lithium niobate in the other channel. They have noticed that the light oscillates between the two waveguides when eigenvalues are purely real. Also, they have observed that increasing the gain, such that the $\mathcal{PT}$-symmetric phase is broken, results in the light going to the gain channel and the intensity growing exponentially [15].

In addition to $\mathcal{PT}$-symmetry breaking, many other quantum and condensed matter phenomena have been predicted and/or observed in waveguide arrays. It has been shown that light propagating through an array of evanescently coupled waveguides is an implementation of a quantum random walk [16, 17]. A quantum random walk is the quantum analog of classical random walk in that the person or object starts with some initial state and this state evolves after flipping a coin and moving accordingly. They differ in that the current state for a quantum random walk is a superposition of all possible states. The two types of random walks have identical outcomes for the first two trials, but start to differ from each other after the third [18].

Another phenomenon that has been experimentally observed in a waveguide array is a classical analog of the quantum Zeno effect. The Zeno effect is the successive observations of the system that prevents the quantum state from decaying. Biagioni and co-workers have been able to observe the classical analog by creating a semi-infinite array. They have found that more light remains in the initial waveguide when compared to a uniform array [19]. In addition to the Zeno effect, an optical analog of Zener tunneling has been observed in waveguide arrays [20]. Zener tunneling is the resulting interband transition of an electron when a constant force is applied in the presence of a lattice [21]. A photonic analog of the Aharonov-Bohm effect has also been observed in waveguide arrays [22]. The Aharonov-Bohm effect shows the importance of the electromagnetic potentials in quantum mechanics [23].

In addition, waveguide arrays allow for the observation of phenomena that are difficult to observe in an electronic system. One such phenomenon is a photonic analog of the Dirac zitterbewegung, which has been predicted to occur in an array where the propagation constant is periodically modulated across the array [24]. The Dirac zitterbewegung is the oscillatory solution to the Dirac equation for a relativistic electron that is a result of the interference between positive and negative energy states [25]. It is advantageous to use light to study the Dirac zitterbewegung as the amplitude of the electron is on the order of its Compton wavelength [26]. Another phenomenon where it is advantageous to use waveguide arrays is Bloch oscillations.

Bloch oscillations are the oscillations of the electron that result from a constant tranverse force being applied to it in a periodic potential [27]. These have been achieved in waveguide arrays by placing a constant temperature gradient across the array, which mimics the force [28]. In addition, they are hard to observe in electronic systems, because of both the scattering of the electrons by the phonons and Zener tunneling [2].

Another advantage of using light is the nonlinear response of the system to the intensity of the incident light. Using this nonlinearity, there have been predictions and observations that are described by a discrete nonlinear Schröndinger equation of the form

$$i\frac{dE_j}{dz} = \beta_j E_j + C_j(E_{j+1} + E_{j-1}) + \eta|E_j|^2 E_j \tag{1.6}$$

where η is the Kerr coeffecient describing the nonlinear response of the array [29–31]. Morandotti and co-workers have observed discrete solitons that exhibit dynamics that are not present in continuous systems. They have found that by not centering the incident light on a waveguide, the soliton can acquire transverse momentum and therefore, propagate both longitudinally and transversely through the array [31]. In addition to solitons, Bludov and co-workers have predicted the occurrence of rogue waves in the waveguide array. They have numerically found that by non-uniformly exciting all of the waveguides with a smooth intensity profile, a rogue wave will occur in the central waveguide [32]. X-waves, which are similar to rogue waves, are another type of wave that has been observed in a nonlinear waveguide. The signature of this type of wave is that intensity peaks in the central waveguide and is maximized when an x-structure is formed in the intensity evolution [33].

This dissertation focuses on the evolution of light inside an array that can be described by the tight-binding model. In Chapter 2, a model for how phase-controlled photonic transport can be achieved in a waveguide array is discussed. The analytical treatment of this model is described in terms of light propagating through an infinite waveguide array. Comparisons are made of this model with the model for directed transport with atoms, and the similarities and differences are discussed in detail.

Chapter 3 presents the wave packet dynamics for light propagating through an array that has a non-uniform but parity-symmetric coupling between adjacent waveguides. It is shown how the wave packet dynamics are tuned through the coupling as the coupling modifies the eigenvalue spectrum for the array. These wave packet dynamics are then compared to the case when the coupling between adjacent waveguides is uniform. The effect of disorder in the medium on the wave packet evolution is discussed in Chapter 4. One important aspect that is discussed is how the light localizes as a function of disorder for non-uniform coupling between adjacent waveguides. In addition, the effects of disorder on the eigenvalue spectrum and the quantum statistics of the output light for different input fields on the eigenvalue spectrum are explored. A summary of the work presented in this dissertation is provided in Chapter 5. Finally, the computer program used to perform the numerical calculations is provided in the Appendix.

2. PHASE-CONTROLLED PHOTONIC TRANSPORT

Directed transport in the absence of a force has been studied extensively after Smoluchowski proposed a gedanken experiment for perpetual motion in 1912 [34]. This directed motion is called ratchet motion after the ratchet tool. The ratchet tool consists of a gear that is free to rotate clockwise and counterclockwise while the pawl allows rotation in only one direction as Figure 2.1 shows. Richard Feynman showed that Smoluchowski's gedanken experiment violates thermodynamics and therefore, it is not possible to achieve perpetual motion. Feynman used an example of a weather vane in a box containing a gas that is connected to a ratchet and pawl that is meant to perform work on a system. He argued that gas molecules would bombard the vane from all directions and when the pawl is in the up position, the wheel could turn in either direction due to the variability of the molecular velocities. Therefore, the gear is equally likely to turn in either direction and the net result is that the gear does not rotate if the entire system is at the same temperature. For this system to perform net work, work must be done on the system to ensure that it does not achieve thermal equilibrium [35]. This has led to the concept of Brownian motors, which can extract energy from non-equilibrium sources [36].

The ratchet motion that Brownian motors display is a result of both an asymmetric potential and the presence of an external noise. Magnasco has shown that if a particle is in an asymmetrical potential in the absence of noise, the particle has zero net drift speed. However, if a particle is subject to an external noise while in this asymmetric potential, it has a non-zero drift speed [37]. An example of an asymmetrical potential that has been used for the ratchet motion is a saw-tooth potential that is shown in Figure 2.2

One such system that displays ratchet motion is a biological motor such as a protein motor. A protein motor accelerates the conversion of adenosine triphosphate

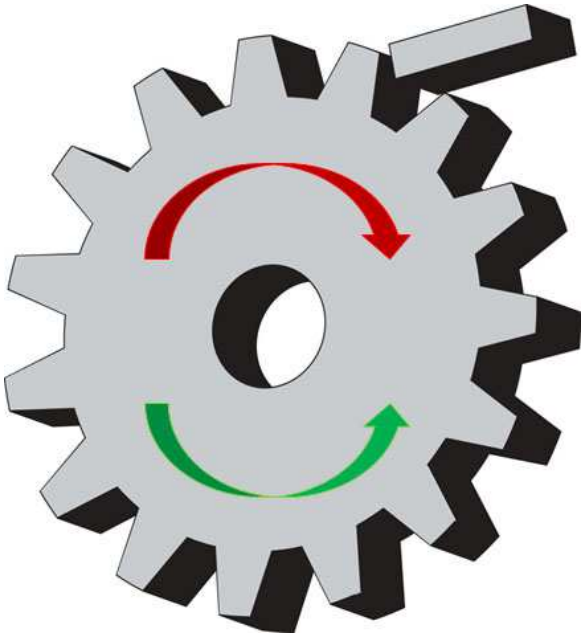

Fig. 2.1. Schematic of a gear and pawl that comprise a ratchet. The gear is free to rotate clockwise and counter-clockwise while the pawl allows rotation in only one direction. Note that for this figure, counter-clockwise rotation is allowed, denoted by the green arrow, and clockwise rotation is not allowed, denoted by the red arrow

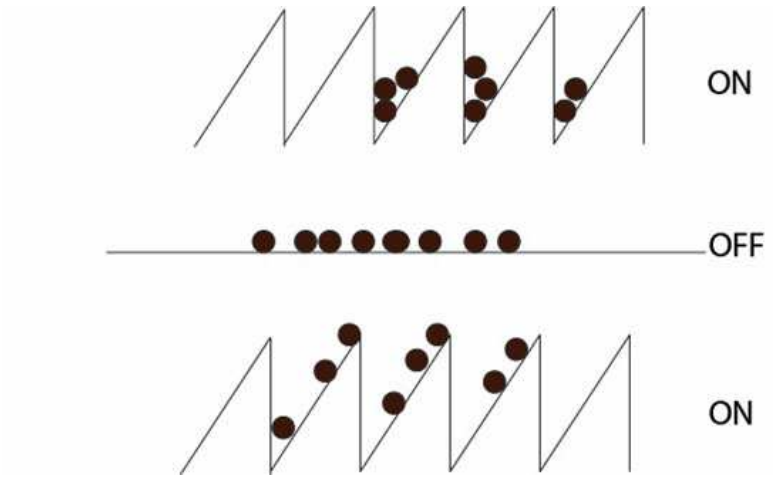

Fig. 2.2. An example of a how ratchet motion is obtained in a saw-tooth potential. The saw-tooth potential is asymmetrical such that when it is on, the particles will collect in its minimum that is offset from the center of the adjacent peaks. This allows the particles to move in the presence of noise when the potential is off while turning on the potential results in the some of the particles now being in the minimum immediately to the left of the initial minimum. Flashing the potential on and off will result in a net drift of particles to the left.

(ATP) to adenosine diphosphate (ADP). Energy is released during the conversion and this energy is used to make the biopolymer move. These protein motors are responsible for intracellur transport as well as muscle action [38]. In addition to protein motors, there are devices that utilize this ratchet motion. One such device is a deoxyribonucleic acid (DNA) pump that can be used for genotyping. Bader and co-workers have been able to achieve this by inter-locking two platinum electrodes on a silicon substrate. By applying a voltage across the electrodes when a solution containing DNA molecules is injected into the device, the two electrodes create a saw-tooth potential. The ratchet effect is achieved by flashing the potential on and off. They have found that the diffusion constant for the DNA molecules depends both on the size of the system and the separation of the two electrodes [39].

In addition to classical systems, the ratchet motion has also been observed in quantum systems. The ratchet motion that arises in quantum systems does not need the presence of external noise to exhibit ratchet motion, unlike classical systems [40]. Cold atoms have been used to observe ratchet motion in a quantum system when the optical fields is detuned far from resonance. Salger and co-workers have created a rubidium Bose-Einstein condensate (BEC) and then exposed it to an asymmetric flashing potential. Figure 2.3 shows an example of an asymmetrical potential that can be used to achieve directed transport of electrons. When the potential is on, the electrons localize at the minima of the potential. As a result, the wavefunctions for the electrons are centered on the minima and are narrow, while the volume of the electron clouds are reduced as the electrons are localized to the minima. When the potential is turned off, the electron clouds expand as well as the electrons' wavefunctions as potential is no longer confining the electrons to its minima. When the potential is turned back on, the electrons now have a non-zero probability to be found in the minima that are to the left of their initial positions, denoted by the yellow part of the distribution when the potential is off. The net result of flashing the potential on and off is a net drift of particles to the left in this case.

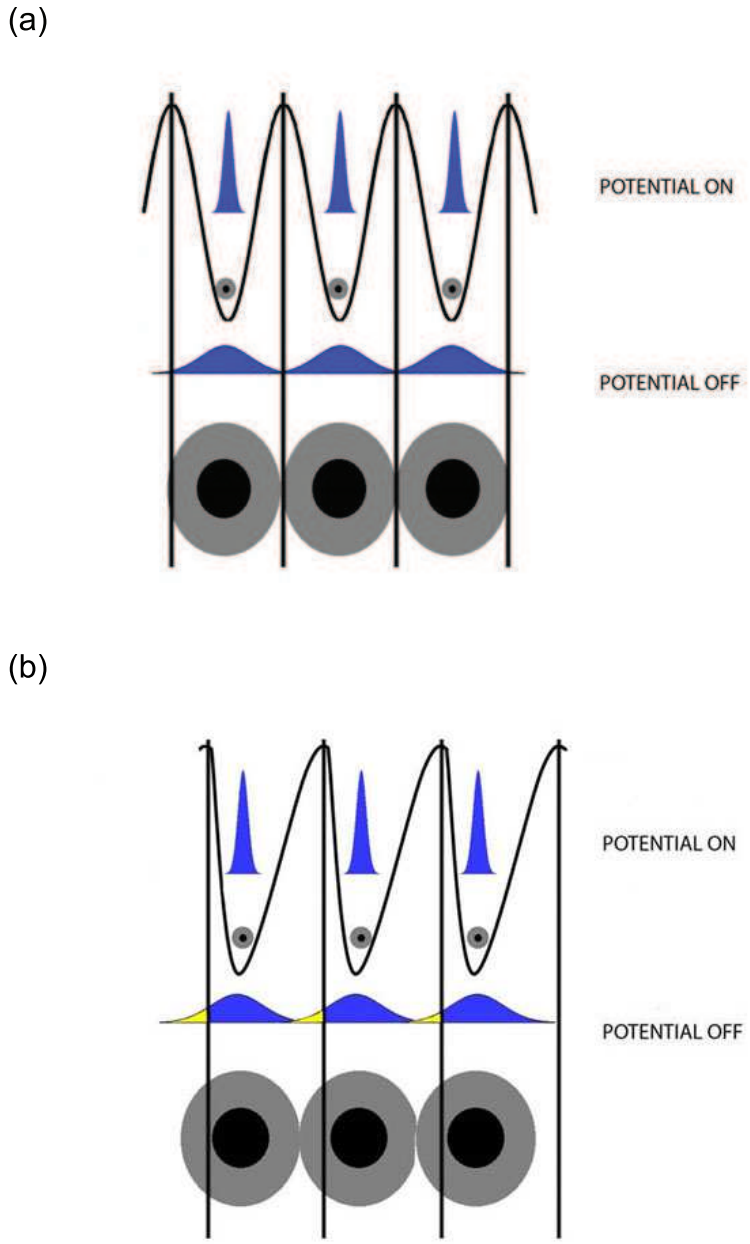

Fig. 2.3. A rachet results from the asymmetry of the potential and initial density distribution. If the potential (black) and the distribution (blue) are symmetric (a), there is no net motion of the particles (gray and black circles). However, if the potential is not symmetrical with respect to the distribution (b), there is a net flow of particles to the left; following [41].

In addition to BECs, Linke and co-workers have been able to observe ratchet motion in semiconductor heterostructures using quantum confinement of the electrons. The currents that arise result from the low energy and high energy electrons flowing in opposite directions. Confining electrons to asymmetric conducting channels whose width is comparable to the Compton wavelength of the electron and applying a source-drain voltage, results in a rocking ratchet for the electrons [42].

This chapter presents a proposed model for photonic transport in an array of evanescently coupled waveguides that utilizes a linearly varying refractive index across the array, and the excitation of two adjacent waveguides. This type of input allows for effects that are not seen when a single waveguide or many waveguides are excited simultaneously. By altering the relative phase between the adjacent inputs, a ratchet motion can be achieved. In addition, the direction of transport for the photons can be altered towards either the increasing refractive index or the decreasing refractive index side. This ratchet effect and control over of the direction of transport is a consequence of quantum interference arising from the relative phase difference between the two inputs.

The results are reminiscent of the quantum ratchet that has been studied theoretically and experimentally in BECs [43]. The distinction between the ratchet like behavior proposed here, versus the BEC ratchet, is that the directed motion of light in a preferred direction arises from interference due to the phase-displaced inputs. Therefore, while classical ratchets usually rely on an asymmetric potential with a symmetric input, the model presented here has a symmetric potential and an asymmetric input.

2.1 Theoretical Model

In this section, photonic transport through an array of uniformly coupled waveguides, as shown in Figure 2.4, is of interest. In addition to the array having uniform coupling between adjacent waveguides, the propagation constant is linearly increasing

across the array, which is analogous to applying a DC electric field across the lattice for an electron in a periodic potential. The Hamiltonian for this system is

$$H = \hbar \sum_j j\beta a_j^\dagger a_j + \hbar C \sum_j (a_{j+1}^\dagger a_j + a_{j-1}^\dagger a_j) \tag{2.1}$$

where the individual waveguides in the array are labeled by the index j, and $j = 0$ is the center waveguide as show in Figure 2.4. The difference in propagation constants for adjacent waveguides is β, C is the coupling between adjacent waveguides, and $a_j^\dagger$ (a_j) is the creation (annihilation) operator.

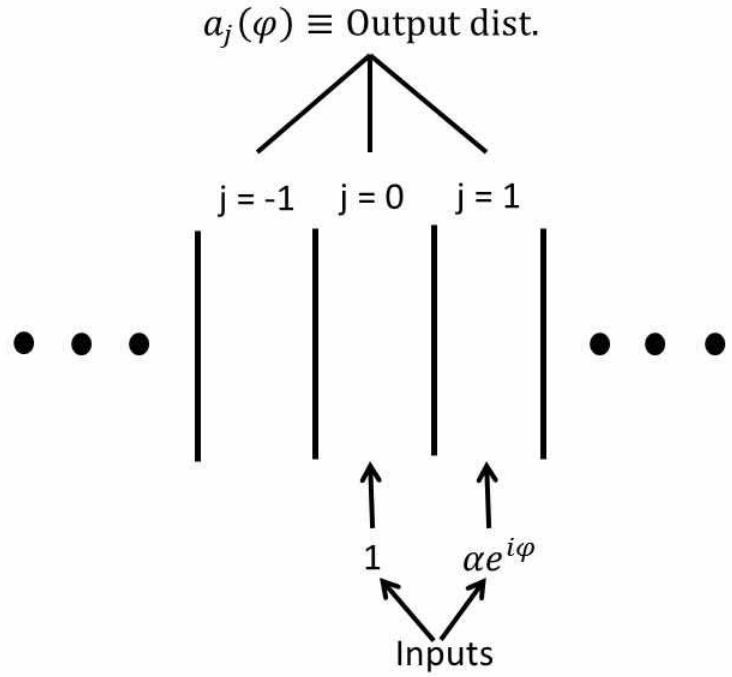

Fig. 2.4. A large waveguide array with the input fields shown.

The operators are described by the Heisenberg equations,

$$\frac{da_j}{dz} = -ij\beta a_j - iC(a_{j+1} + a_{j-1}) \tag{2.2}$$

and with use of Fourier relations

$$a_j = \frac{1}{\sqrt{2\pi}} \int_{-\pi}^{\pi} \tilde{a}(k) e^{ikj} dk \tag{2.3}$$

$$\tilde{a}(k) = \frac{1}{\sqrt{2\pi}} \sum_j a_j e^{-ikj}, \tag{2.4}$$

Eq. (2.2) can be written in Fourier space as

$$\frac{d\tilde{a}(k)}{dz} = -2iC\tilde{a}(k) \cos\, k - i\beta \left(\frac{\partial}{\partial(-ik)} \right) \tilde{a}(k). \tag{2.5}$$

As a result of the linearity of the operators, the annihilation operator for waveguide j can be written in terms of an input-output relation

$$a_j(z) = \sum_l G_{j,l}(z) a_l(z = 0) \tag{2.6}$$

where $G_{j,l}$ is the Green's function that is given by [44]

$$G_{j,l}(z) = \exp \left[i\beta z + \frac{i(j-l)(\beta z - \pi)}{2} \right] J_{l-j} \left[\frac{4C}{\beta} \sin \left(\frac{\beta z}{2} \right) \right] \tag{2.7}$$

where J is the Bessel function of the first kind, l is the input location, z is the propagation distance, and j is the waveguide index. Peschel and co-workers obtained Eq. (2.7) by solving Eq. (2.5) using the assumption that the array is infinite, taking the Fourier transform, and then applying the initial conditions [28].

For a single photon input at the center waveguide, $l = 0$, the intensity as a function of propagation distance is

$$I_j = |G_{j,0}|^2 = J_j^2 \left[\frac{4C}{\beta} \sin \left(\frac{\beta z}{2} \right) \right]. \tag{2.8}$$

Note that the argument of the Bessel function is periodic, which results in the intensity evolution exhibiting the breathing modes of the system, see Figure 2.5. The period of the Bessel function is $4\pi/\beta$ and the spread of the wave packet is controlled through the ratio C/β. Figure 2.5(a) shows that for $C/\beta = 4$ the wavepacket reaches the edges of the array and eventually delocalizes. When $C/\beta = 1.5$, the breathing modes of the system are visible as the wavepacket does not reach edges of the array, as it is

confined to a central region of the array consisting of approximately nine waveguides. In addition, the period of the breathing modes is approximately 10 coupling lengths, see Figure 2.5(b). For $C/\beta = 1$, Figure 2.5(c) shows that the wavepacket is confined to a central region of the array consisting of approximately five waveguides and the period of the breathing modes is approximately 7 coupling lengths. Therefore the distance over which the breathing modes of the system are visible is dependent on the ratio C/β as the reflections at the boundaries generate interference that delocalizes the wavepacket. The longer the wave packet remains in the central region of the array, the longer the distance over which the breathing modes exist. To gain some insight into these breathing modes, Bloch oscillations are now examined. They that occur for an electron in a periodic potential in the presence of an external DC electric field when the number of sites is infinite. The force that acts on the electron is $-eE = \hbar\frac{dk}{dt}$ where e is the charge of a proton and E is the amplitude of the applied electric field. The position of the electron is oscillatory due to the presence of the lattice, $x(t) = -\frac{2C}{eE}\cos(\frac{aeEt}{\hbar})$ where a is the distance between lattice sites and the initial position is $x(t=0) = 0$ [2]. If the lattice is not present, the electron uniformly accelerates in one direction given by the DC electric field.

The input conditions on the field amplitude for this model are

$$a_j(t=0) = \delta_{j,0} + \alpha\delta_{j,1}e^{i\varphi} \tag{2.9}$$

where α is the amplitude of the adjacent input and φ is the relative phase difference between the two inputs.Note that for the following analysis, α is assumed to be real. The array index is assumed to run from $j = -\infty$ to ∞ (see Figure 2.4), where $j = 0$ is the middle waveguide. The $|a_j|^2$ plays the role of density distributions as the intensity distribution is identical to the probability distribution. For photonic transport to be achieved, analogous mean energy, $\langle E\rangle$ and mean momentum, $\langle p\rangle$ both have to be linear in the propagation distance, z. The kinetic energy term in Eq. (2.5) involves the first derivative of k. This can be explained by examining a system with a narrow momentum distribution such as for a BEC. The first term in the expansion of p^2 about the mean momentum is linear in p, which in coordinate space representation

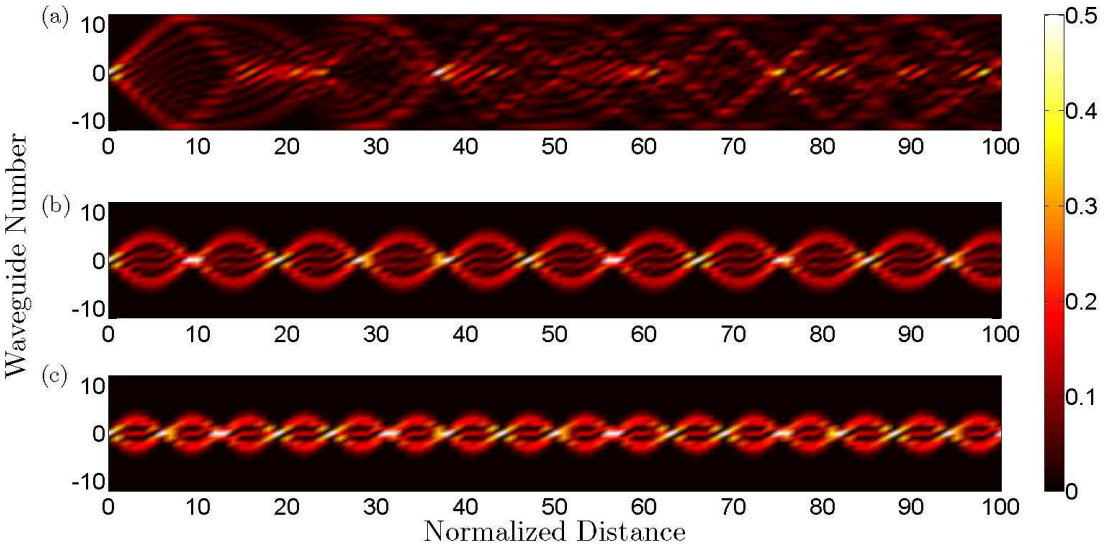

Fig. 2.5. Intensity evolution as a function of normalized distance for an array of $N = 25$ waveguides. The ratio of C/β is (a) 4, (b) 1.5, and (c) 1. Note that the spread increases with C/β and the visibility of the system's breathing modes decrease with distance, because the system is finite and the boundaries generate interference when the light reflects off them. Thus, when the light is confined to the central region of the array, the breathing modes are visible for a much longer distance than for a wave packet that reaches the edges of the array.

is $-i\hbar d/dx$. As the potential term in Eq. (2.5) is symmetric, this is analogous to a symmetrical potential in coordinate space that ratchet motion requires. Thus, Fourier space is analogous to coordinate space and site space is analogous to momentum space. This is advantageous as the natural space for the waveguide array is site space.

To study photonic transport, $\langle j \rangle$ and $\langle j^2 \rangle$ must be calculated, as these are analogous to the mean momentum and mean energy, respectively. The expectation values for the mean site and mean energy are calculated as $\langle j \rangle = \sum_{j=-\infty}^{\infty} jI_j$ and $\langle j^2 \rangle = \sum_{j=-\infty}^{\infty} j^2 I_j$. The output intensity for the j^{th} waveguide, I_j, is

$$\begin{aligned} I_j &= |G_{j,0}|^2 + |\alpha G_{j,1}|^2 + \alpha G_{j,0} G_{j,1}^* e^{-i\varphi} + \alpha G_{j,0}^* G_{j,1} e^{i\varphi} \\ &= |J_j \left[\frac{4C}{\beta} \sin\left(\frac{\beta z}{2}\right) \right]|^2 + |\alpha J_{1-j} \left[\frac{4C}{\beta} \sin\left(\frac{\beta z}{2}\right) \right]|^2 \\ &\quad - 2\alpha J_j \left[\frac{4C}{\beta} \sin\left(\frac{\beta z}{2}\right) \right] J_{1-j} \left[\frac{4C}{\beta} \sin\left(\frac{\beta z}{2}\right) \right] \\ &\quad \times \sin\left(\frac{\beta z}{2} - \varphi\right) \end{aligned} \tag{2.10}$$

and this is identical to the probability of detecting a photon at waveguide j as a result of the isomorphism that exists between the longitudinal component of the Helmholtz equation and the Heisenberg equation for the annihilation operator, a_j.

Using properties of the Bessel functions, the average site position is written as

$$\sum_{j=-\infty}^{\infty} jI_j = |\alpha|^2 + \frac{4\alpha C}{\beta} \sin\left(\frac{\beta z}{2}\right) \sin\left(\frac{\beta z}{2} - \varphi\right) \tag{2.11}$$

and a similar expression for the analog of the mean energy is given by

$$\begin{aligned} \sum_{j=-\infty}^{\infty} j^2 I_j = |\alpha|^2 &+ \frac{4\alpha C}{\beta} \sin\left(\frac{\beta z}{2}\right) \sin\left(\frac{\beta z}{2} - \varphi\right) \\ &+ \frac{1 + |\alpha|^2}{2} \left(\frac{4C}{\beta} \sin\left(\frac{\beta z}{2}\right) \right)^2 . \end{aligned} \tag{2.12}$$

For small values of z, the average position, Eq. (2.11), is proportional to $-\alpha \sin(\varphi) z$, which shows that the direction of transport for the photons is dependent on the relative phase of the inputs. The mean energy is also linear in z and the interference term for the mean position is also present in the expression for the mean energy.

This shows that ratchet-like motion of the light exists for small values of z when a phase-displaced input is used. The asymmetry that is necessary for the ratchet motion exists in the overall Hamiltonian, though the intrawaveguide interaction term is symmetric. The oscillatory solutions for both the mean momentum and mean energy result from the fact that the potential is non-flashing as these oscillatory solutions are not seen in systems that utilize a flashing potential as the flashing of the potential prevents the particles' direction of motion from changing.

2.2 Results

This section describes the results showing photonic transport that can arise in a waveguide array when phase-displaced inputs are utilized. For all results shown, the inputs are at the $j = 0$ and $j = 1$ waveguides. The coupling length,$1/C$, is chosen as the characteristic distance for the system. Figure 2.6 shows the intensity evolution given by Eq. (2.10) for adjacent phase-displaced inputs. Note the asymmetry along the j-axis, as this results from the phase-displaced inputs. The transport is now noticeable as a relative phase difference, φ, controls which side of the j-axis has more intensity. For values of φ between 0° and 180°, the majority of the intensity remains on the negative side of the j-axis while values between 180° and 360° remains on the positive side.

Figure 2.7(a) shows the behavior of $\langle j \rangle$ as a function of the propagation distance within a waveguide for $\varphi = 37°$. Note that the profiles are oscillatory, indicating that the direction of the transport within a waveguide is periodically alternating. However, for very small values of z denoted by a black circle, the slope of the curve is negative, indicating a deflection to the low index side of the array. When the relative phase is taken to 217°, as in Figure 2.7(b) the deflection of photons is now to the high index side.

Figure 2.8(a) shows the behavior of energy as a function of propagation distance and once again the profiles are oscillatory. When the phase is taken to 217°, as in Figure 2.8(b), both the momentum and energy show periodic oscillations, but the deflection of photons is now to the high index side denoted by black circles. The oscillatory motion of the beam results from the fact that the potential is non-flashing as these oscillations are not seen in systems that utilize a flashing potential as the flashing of the potential prevents the particles' direction of motion from changing.

The novelty of this approach is that the direction of transport is controllable for a constant, non-flashing potential. In addition, the potential is always present while the potential used to obtained ratchet motion in a BEC is a flashing [43]. Note that

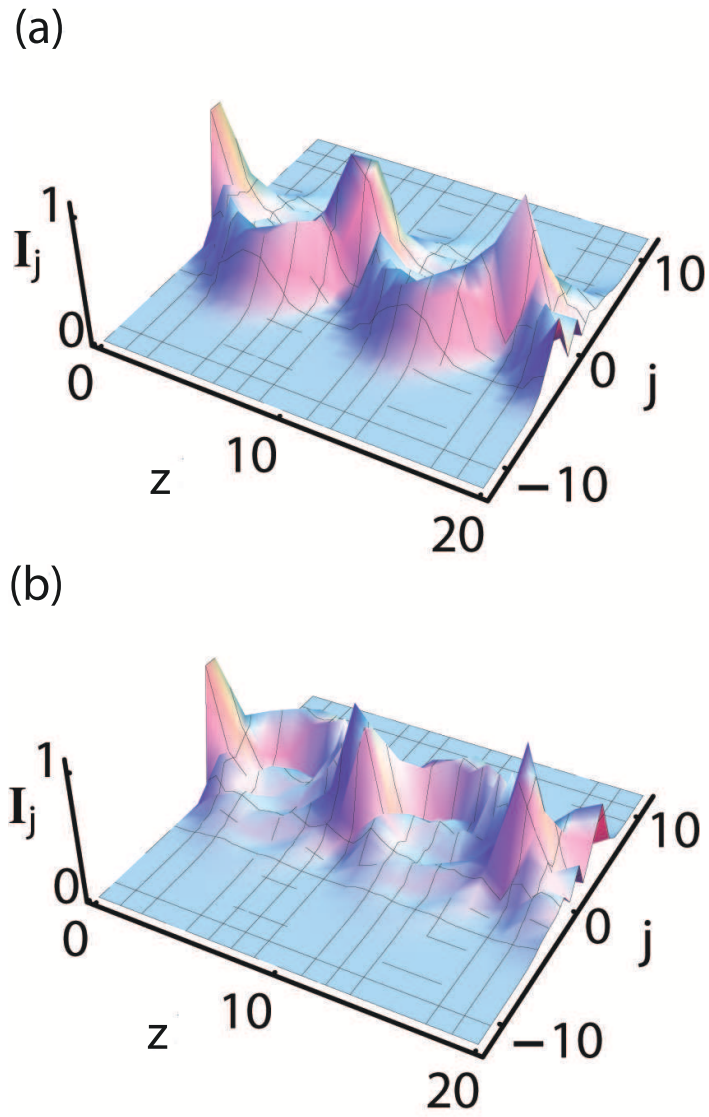

Fig. 2.6. Output intensity distribution, I_j, as a function of z for $j = -12, ..., 12$. The values of the parameters are $\beta/C = 0.73$ and $\alpha = 1$ with (a) $\varphi = 37°$ and (b) $\varphi = 217°$. The asymmetry in the intensity evolution is a result of relative phase difference between the two inputs.

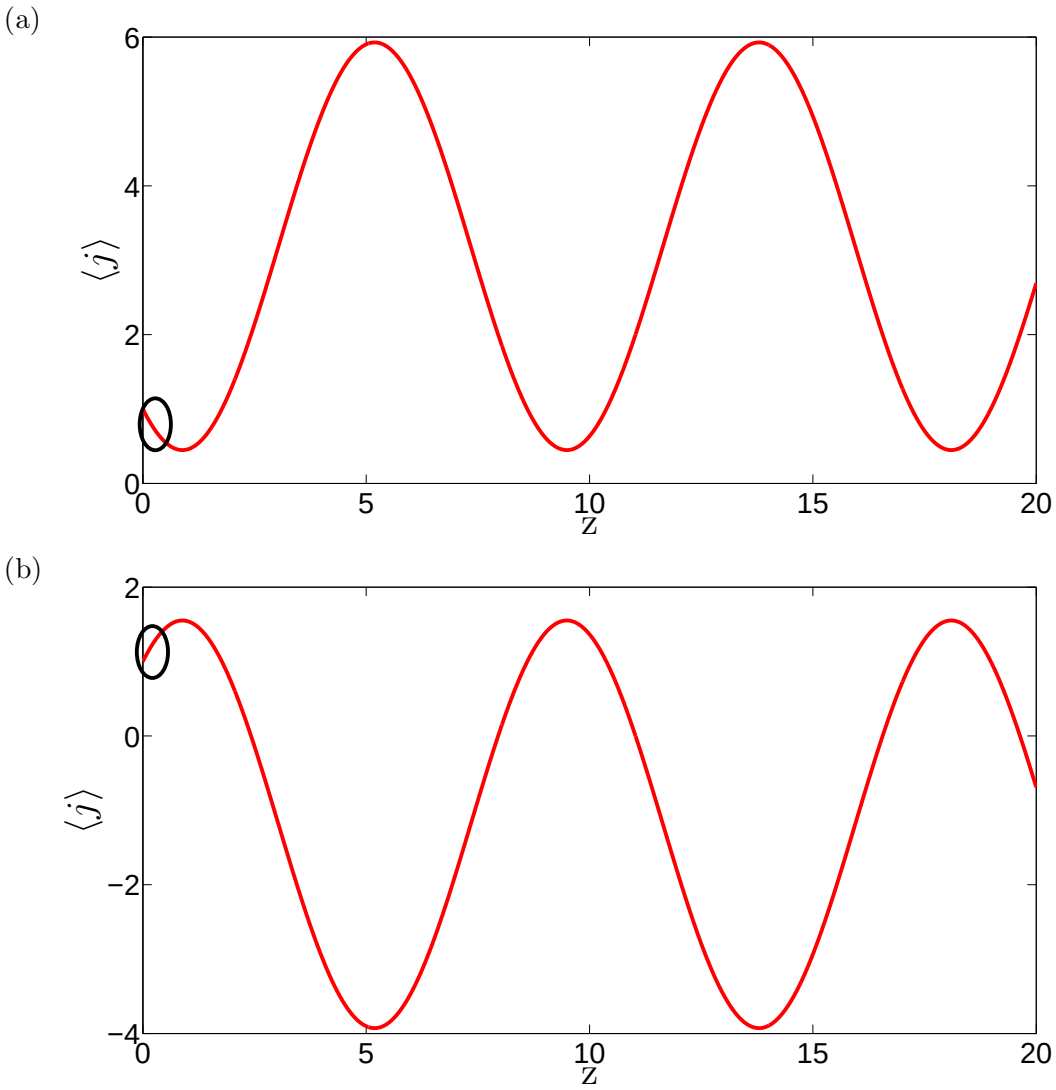

Fig. 2.7. Plots showing ratchet like behavior for the momentum. The values of the parameters are $\alpha = 1$, $\beta/C = 0.73$, with (a) $\varphi = 37°$ and (b) $\varphi = 217°$. The black circle denotes the regions where the mean momentum is linear in z.

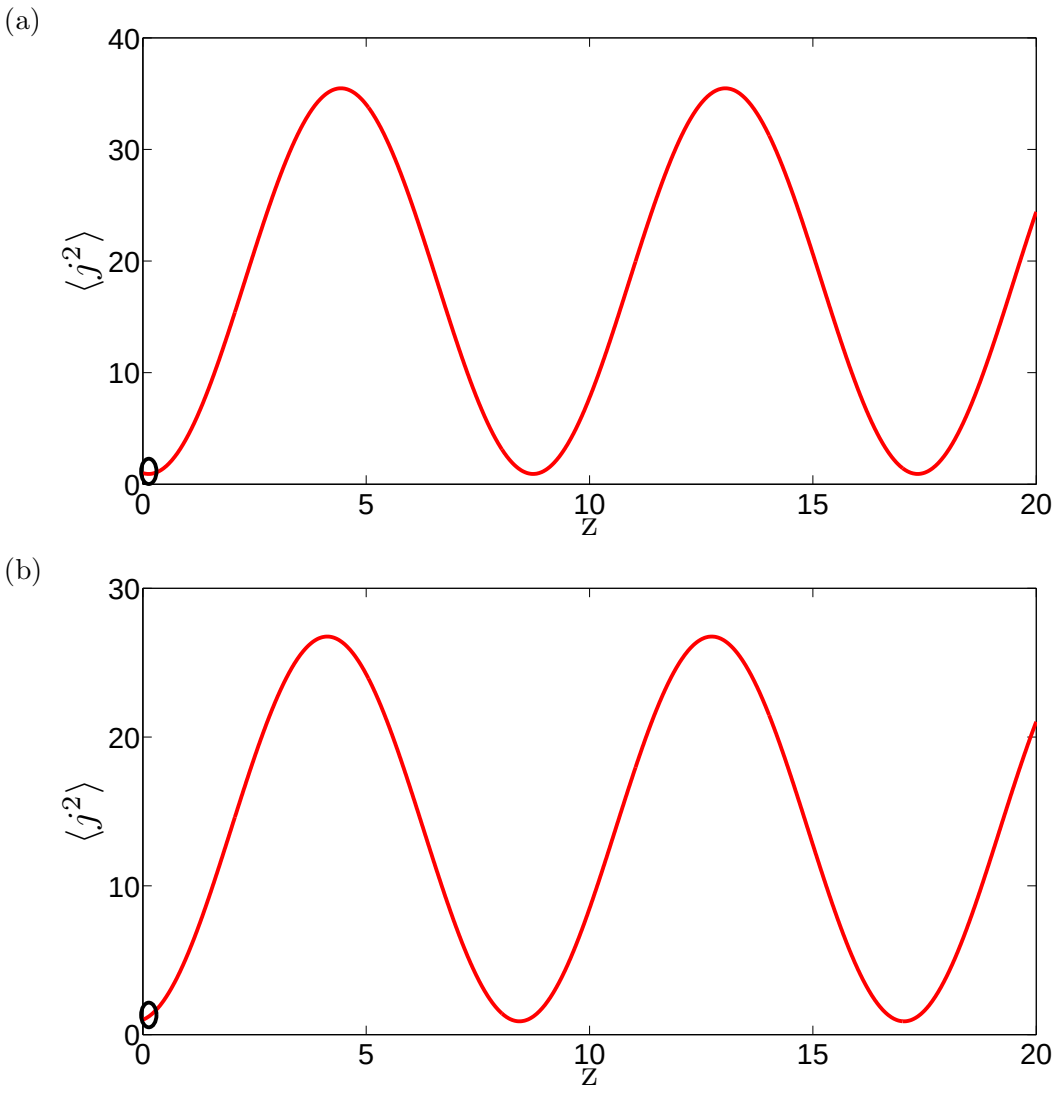

Fig. 2.8. Plots showing ratchet like behavior for the energy. The values of the parameters are $\alpha = 1$, $\beta/C = 0.73$, with (a) $\varphi = 37°$ and (b) $\varphi = 217°$. The black circle denote the regions where the mean energy is linear in z.

even though the model assumes an infinite array, the results are still valid with an finite array, given that the wave packet does not interact with the boundaries.

2.3 Conclusion

In conclusion, this chapter presented a description of a model achieving photonic transport in an all-optical system. The model that has been presented in this chapter utilized the tight-binding model and assumed that the propagation constant was linearly increasing across an array with uniform waveguide coupling. In Fourier space, the potential and kinetic energy terms are interchanged; therefore, the potential was symmetric. This resulted in the Fourier space being analogous to coordinate space and site space being analogous to momentum space. This was advantageous to studying directed transport as this is the natural measurement space of the system.

For a single excited waveguide, the breathing modes of the system were visible in the intensity evolution. This was analogous to applying a constant voltage across a lattice for an electron and observing Bloch oscillations. Exciting adjacent waveguides introduced the interference between the two inputs through the relative phase and amplitude of the second input. Because of this interference, both the mean momentum and mean energy were linear in z for short propagation distances. Thus, the key element in the model for obtaining photonic transport was exciting adjacent waveguides and having a relative phase difference between the inputs.

3. TUNABLE WAVEGUIDE ARRAYS

In the previous chapter, the linear propagation constant was linearly increased across the array, as this was analogous to applying a constant transverse force to an electron in a periodic potential. In addition applying a transverse force, one can modify the effective mass, m^*, of the electron by modifying the coupling between lattice sites as $\frac{1}{m^*} \propto \frac{d^2C(k)}{dk^2}$. For waveguide arrays, this is easily done during the fabrication process, as varying the distance between waveguides modifies the coupling between adjacent waveguides. This chapter focuses on the wave packet dynamics in arrays with non-uniform, position-dependent waveguide coupling profiles, as they have not been extensively studied. One such position-dependent waveguide coupling profile that has been examined is

$$C_n = \sqrt{n} \tag{3.1}$$

where n is the waveguide index number and this waveguide coupling profile has been used to examine Glauber-Fock lattices. Since the preferential direction for light to tunnel is the same throughout the array, the light goes to the side with largest waveguide index number [45]. In general, when the waveguide coupling is not parity-symmetric, the light prefers to go to one side of the array over the other. The parity-symmetry of the array implies mirror-symmetry about its center. One such coupling function that is parity-symmetric is

$$C_\alpha(j) = C[j(N-j)]^{\alpha/2} \tag{3.2}$$

where j is the waveguide index number, N is the total number of waveguides, and α is the parameter that describes the coupling profile of the waveguides. The coupling function $C_\alpha(j)$ describes the coupling of waveguides j and $j+1$. Joglekar and Saxena showed that for $\alpha \geq 0$, the system has only extended states while for $\alpha < 0$, the system has both localized and extended states [46]. This form of the coupling profile has been

experimentally achieved by Bellec and co-workers for $\alpha = 1$ by having a separation distance $d_{j,j+1} \sim -\ln(\sqrt{j(N-j)})\beta^{-1}$ between adjacent waveguides, where β is the linear propagation constant for each waveguide [47].

The shapes of the waveguide coupling profiles are shown in Figure 3.1. For $\alpha > 0$, the profile has a maximum at the center of the array while for $\alpha < 0$, the profile has a minimum at the center. This means that the light prefers to be at the center of the array for values of $\alpha > 0$ as the light tunnels in the direction of the greatest waveguide coupling. For negative values of α, the light prefers to be at the edges of the array as the coupling is the greatest at the edges. This α-dependent coupling profile can be experimentally achieved by symmetrically increasing (decreasing) the center-to-center distance between adjacent waveguides for negative (positive) values of α. For $\alpha = 0$, the coupling is uniform throughout, as there exists no preferential direction for the light to tunnel and this is commonly referred to as a periodic array.

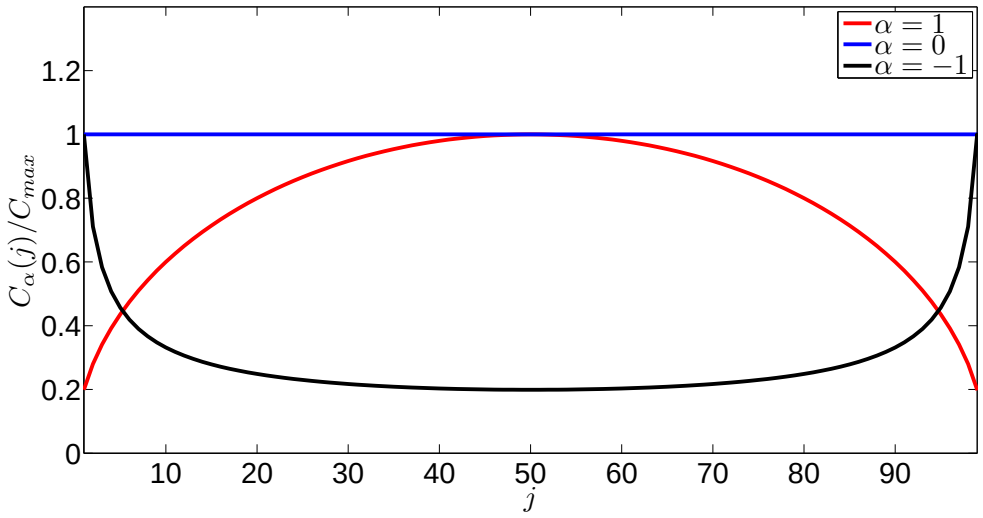

Fig. 3.1. Coupling profile, $C_\alpha(j) = C[j(N-j)]^{\alpha/2}$, as a function of the waveguide index number, j, for $\alpha = 1$ (red), $\alpha =$ (blue), and $\alpha = -1$ (black). For $\alpha = 0$, the coupling profile is constant as the waveguides are uniformly coupled. For values of $\alpha > 0$, the profile will have a maximum at the center of the array while for $\alpha < 0$, the profile will have minimum at the center. The number of waveguides in the array is $N = 100$.

3.1 Tight-Binding Model

The tight-binding Hamiltonian describing the propagation of light in an array whose waveguide coupling is described by Eq. (3.2) is

$$H = \hbar \sum_j C_\alpha(j)(a_{j+1}^\dagger a_j + a_j^\dagger a_{j+1}) \tag{3.3}$$

where the linear propagation constant is the same for each waveguide and is set to zero as it is irrelevant. The energy bandwidth of the system, $\Delta_\alpha^{(0)}$, is defined as the energy difference between maximum energy, E_{max} and the minimum energy, E_{min}. The inverse of the bandwidth is chosen as the characteristic time-scale for the system, $\tau_\alpha(N) = \hbar/\Delta_\alpha(N)$, as the wave packet dynamics occur on physically different time scales for different values of α. Joglekar and Saxena showed that the bandwidth scales as $\Delta_\alpha(N) \sim \hbar C N^\alpha$ for $\alpha > 0$ and $\Delta_\alpha \sim \hbar C N^{-|\alpha|/2}$ for $\alpha < 0$ [46]. When $N \to \infty$, the coupling term for $j = \frac{N}{2}$ ($j = 1$) dominates Eq. (3.3) for $\alpha > 0$ ($\alpha < 0$). The value of τ_α decreases inversely with α; therefore, values of $\alpha > 0$ correspond to physically short times, while values of $\alpha < 0$ correspond to physically long times. Additionally, α controls the shape of the energy spectrum, see Figure 3.2. The energy spectrum is symmetric about $E_n = 0$ for each value of α. For $\alpha = 0$ (green line), the energy spectrum is given by $E_n = 2C\cos\left(\frac{n\pi}{N+1}\right)$, where the analogous Bloch momentum is $k_n = \frac{n\pi}{(N+1)a}$ and a is the lattice constant. When $\alpha = 1$ (red line), the energy spectrum is linear and for $\alpha = 2$ (blue line), the energy spectrum is nearly linear in shape. Note when $\alpha = -1$ (black line), there exist bound states at the edges of the array which correspond to the energies that are near the ends of the energy spectrum [46].

3.2 Wave Packet Dynamics

To investigate how the shape of the energy spectrum influences the wave packet dynamics, the time-dependent wave function is calculated as

$$|\psi(t)\rangle = e^{-i\frac{Ht}{\hbar}}|j\rangle \tag{3.4}$$

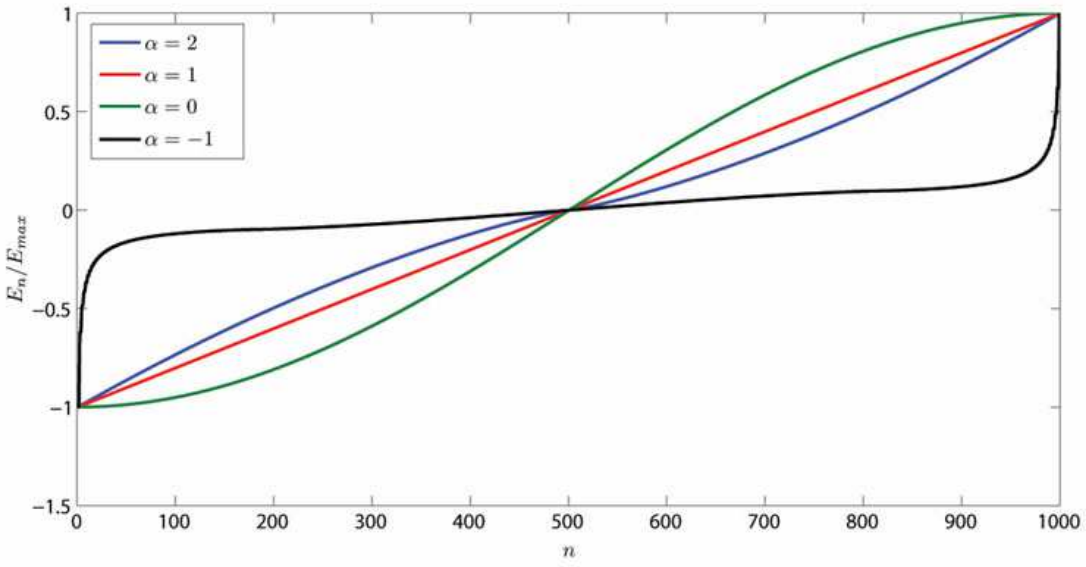

Fig. 3.2. Energy spectra for $\alpha = 2$ (blue), $\alpha = 1$ (red), $\alpha = 0$ (green), and $\alpha = -1$ (black). The energy spectrum for $\alpha = 0$ is $E_n = 2\hbar C\cos(n\pi/N+1)$ and is linear for $\alpha = 1$. For $\alpha = 2$, the energy spectrum is nearly linear while for $\alpha = -1$, the energy spectrum is relatively flat in the middle and nearly vertical at the edges, which correspond to bound states at the edges of the array. For any value of α, the energy spectrum is symmetric about $E_n = 0$, which is a consequence of the tight-binding model [2].

where j is the waveguide index number of the initial waveguide where a single photon is injected, and probability to detect a photon at waveguide k is $P_k = |\langle k|\psi(t)\rangle|^2$. Note that the probility distribution is identical to the intensity distribution of light in the array. Figure 3.3 shows that for values of $\alpha < 0$, there exists bound states at the edges of the array as part of the wave packet localizes at the edges [46]. The initial position is $j = 5$ and the array consists of 100 waveguides. Even though there are bound states at the edges of the array, part of the light propagates towards the other side of the array. This is a result of both bound states and extended states existing in the system for $\alpha < 0$. The rate of spread for the wave packet is α dependent, as for $\alpha = -1$ shown in Figure 3.3(a), part of the light is reflected off of the farthest edge at approximately $t = 530\tau_\alpha$ while for $\alpha = -2$ and $\alpha = -3.31$, the light has yet to

reach the farthest edge when $t = 800\tau_\alpha$, as shown in Figures 3.3(b) and 3.3(c). This results in the waveguide coupling decreasing with α as the $C_\alpha(j) \to 0$ as $\alpha \to -\infty$, which results in a decreasing rate of wave packet expansion.

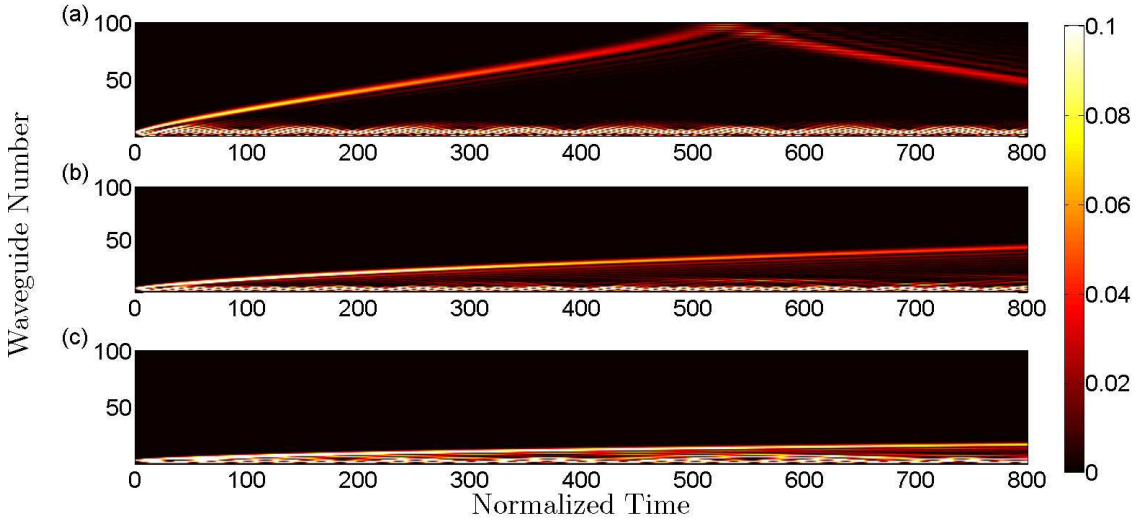

Fig. 3.3. Wave packet evolution as a function of the normalized time, t/τ_α, for (a) $\alpha = -1$, (b) $\alpha = -2$, and (c) $\alpha = -3.31$. The number of waveguides is 100 and the initial waveguide is $j = 5$. Note that there exists bound states at the edges of the array for $\alpha < 0$.

To investigate the spread of the wave packet further, the wavepaceket is now initially at the center of the array. Figure 3.4(b) shows that for a periodic array, the light reaches the edges of the array in the smallest amount of normalized time due to the uniform coupling of the array, and delocalizes due to the interference created by the reflections at the boundaries. For $\alpha = -1$, the wave packet eventually delocalizes as its energy spectrum is nonlinear, as shown in Figure 3.4(c). The rate of delocalization is significantly smaller than for $\alpha = 0$, as the waveguide coupling is significantly smaller. Figure 3.4(a) shows that when $\alpha = 1$, the wave packet undergoes periodic reconstruction as its energy spectrum is linear with a spacing of $\Delta E = 2\hbar C$ between adjacent energy levels [46, 48]. This is analogous to a harmonic oscillator, which has constant spacing between energy levels of $\Delta E = \hbar\omega$. This periodic wave

packet reconstruction is a general result for any quantum system that has a linear energy spectrum.

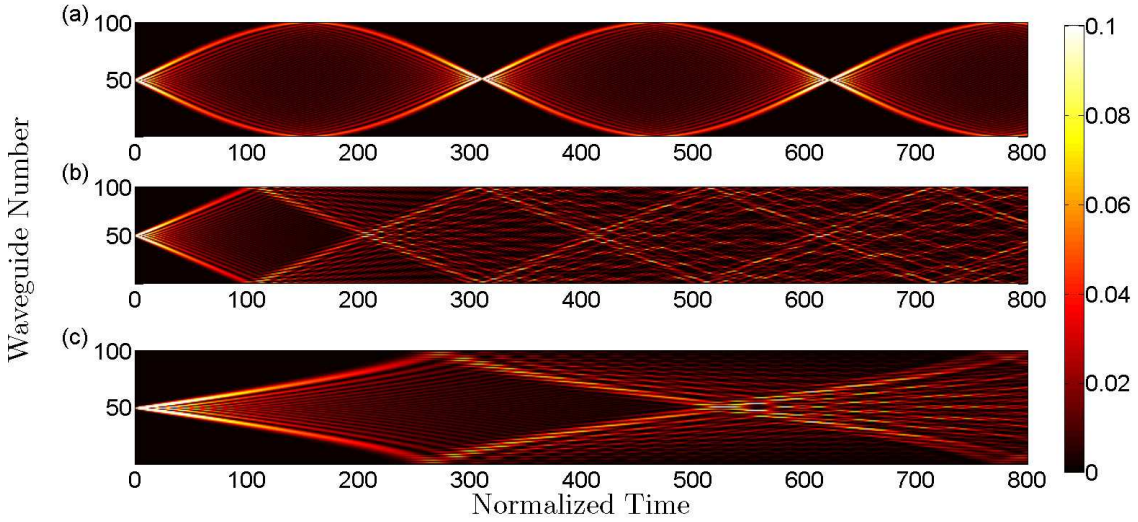

Fig. 3.4. Wave packet evolution as a function of the normalized time, t/τ_α, for (a) $\alpha = 1$, (b) $\alpha = 0$, and (c) $\alpha = -1$. The number of waveguides is 100 and the initial waveguide is $j = 50$. Note that periodic reconstruction for $\alpha = 1$ is the result of the linear energy spectrum. The wave packet reaches the edges of the array in the smallest amount of normalized time for a periodic array, as the waveguide coupling is uniform throughout. For $\alpha \neq 1$, the wave packet eventually delocalizes as a result of the interference that is created by the reflections at the edges of the array.

The location of where this periodic reconstruction occurs is dependent on the location of the initial waveguide. Figure 3.5 shows that for a wave packet that is initially at waveguide j, it reconstructs at waveguide $N + 1 - j$. For a initial position of $j = 5$, the wave packet reconstructs at waveguide $N + 1 - j = 96$ and this reconstruction alternates between these two waveguides, as shown in Figure 3.5(a). This reconstruction occurs first at the parity-symmetric waveguide, $N + 1 - j$, and then at the initial waveguide regardless of the initial position, as shown in Figures 3.5(b) and 3.5(c) with inputs at $j = 23$ and $j = 37$, respectively. The location of the wave packet reconstruction is a result of the fraction of the wave packet that

goes to the high waveguide index side and the fraction that goes to low index side having the same path lengths. The periodic reconstruction is robust in the presence of the boundaries of the array due to its linear energy spectrum, as the wave packet reconstructs after it reflects back towards the center of the array. When $\alpha \neq 1$, the interference from the edges of the array delocalize the wave packet.

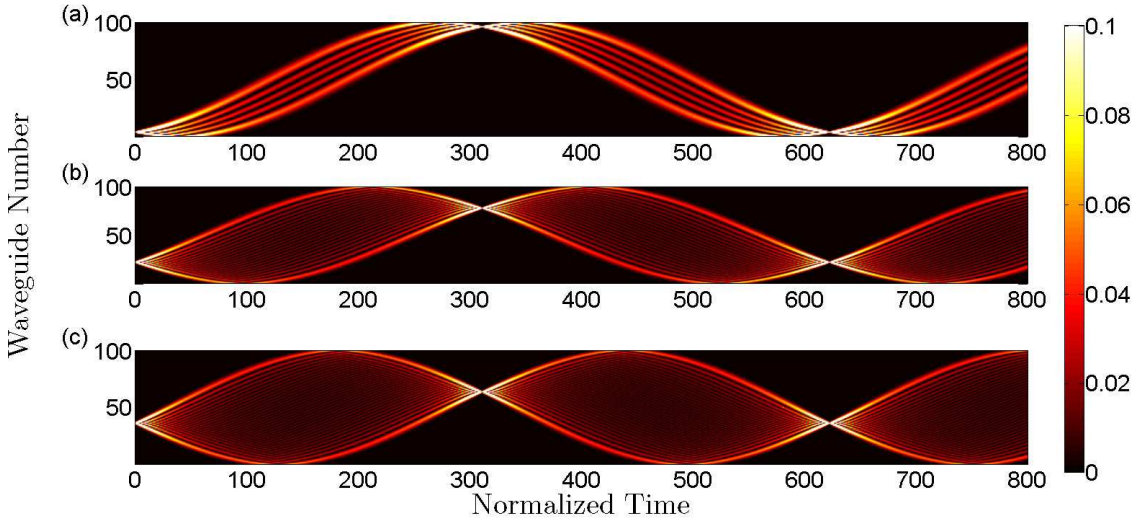

Fig. 3.5. Wave packet evolution as a function of the normalized time, t/τ_α with $\alpha = 1$. The number of waveguides in the array is $N = 100$ and the initial waveguide is (a) $j = 5$, (b) $j = 23$, and (c) $j = 37$. The location of the wave packet reoconstruction alternates between the initial waveguide j and its mirror-symmetric counterpart, $N+1-j$. In addition, this periodic reconstruction is robust in a finite array and the wave packet will not delocalize, unlike values of $\alpha \neq 1$.

The effects of the boundaries for $\alpha = 0$ can be seen in the expression for the probability amplitude A_j. For an infinite array, the probability amplitude for waveguide j is

$$A_j(t) = i^{j-j_0} J_{j-j_0}(2Ct) \tag{3.5}$$

where j_0 is the initial location in the array, J is the Bessel function of the first kind, and the probability to detect light in waveguide j is $P_j(t) = |A_j(t)|^2$ [4]. The presence of a single edge is seen in the expression for a semi-infinite array

$$A_j(t) = i^{j-j_0} J_{j-j_0}(2Ct) + i^{j+j_0} J_{j+j_0}(2Cz) \tag{3.6}$$

where the second term is due to the reflection at the edge [49]. When a second edge is present, Makris and Christodoulides showed that the expression for the probability amplitude can be obtained using the method of images [50].

The method of images for light propagating in a finite waveguide array is analogous to an electron between two conducting planes that are grounded. To satisfy the boundary conditions at the planes, an infinite number of image charges are paired in such a manner as to satisfy these conditions. The boundary conditions for light are that the electric fields at the edges of the array are zero, i.e. $A_0 = A_{N+1} = 0$. This results from the fact that the tight-binding model that describes the propagation of the light, Eq. (3.3), is lossless. Figure 3.6 shows the configuration of images for an array of $N = 2$ waveguides with a single input (green arrow) at the left waveguide. As the signs of the charges alternate for the two conducting planes, the phases of the fields alternate between 0 and π. The relative phases of the input and images are denoted by the direction they are pointing. Arrows pointing up denote a phase of 0 while arrows pointing down denote a phase of π relative to the input. The black lines represent the edges of the array where the fields are required to be zero. This method is only valid in the space between the two black lines, which is advantageous as the space between the lines is the physical waveguide array.

The probability amplitude for waveguide j is given by

$$\begin{aligned} A_j(t) &= i^{j-j_0} J_{j-j_0}(2Ct) + i^{j+j_0} J_{j+j_0}(2Ct) \\ &+ \sum_{r=-\infty}^{r=-1} \left(i^{-(2N+2)r} [i^{j-j_0} J_{j-j_0-(2N+2)r}(2Ct) + i^{j+j_0} J_{j+j_0-(2N+2)r}(2Ct)] \right) \\ &+ \sum_{r=1}^{r=\infty} \left(i^{-(2N+2)r} [i^{j-j_0} J_{j-j_0-(2N+2)r}(2Ct) + i^{j+j_0} J_{j+j_0-(2N+2)r}(2Ct)] \right) \end{aligned} \tag{3.7}$$

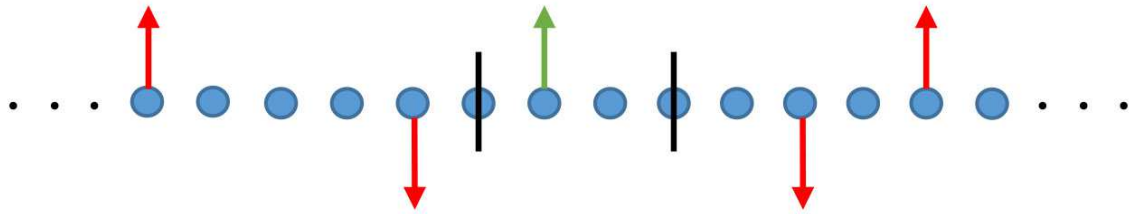

Fig. 3.6. Configuration of image charges for a periodic infinite array. The initial input is the green array and the images are the red arrows. The array of interest consists of $N = 2$ waveguides and the black lines correspond to the locations where the fields are required to be zero.

where r is the index of the image pair [50]. The third and fourth terms are a result of the infinite number of images that are needed to ensure that the boundary conditions are satisfied when a second edge is present. The number of terms that need to be kept increase with the number of reflections from the edges of the array. The intensity due to the interference that is created by the reflections, $I_{interference}$, is given by

$$I_{interference} = \sum_{j=1}^{N} \left[|A_j|^2 - \sum_{r=-\infty}^{r=\infty} \left(J^2_{j-j_0-(2N+2)r}(2Ct) + J^2_{j+j_0-(2N+2)r}(2Ct) \right) \right] \tag{3.8}$$

where only the cross terms from Eq. (3.7) remain in $I_{interference}$. The maximum value is greater for an input at the edge than at the center of the array and interference decreases until it reaches a steady state value of approximately $\frac{1}{N}$, as shown in Figure 3.7. This steady state value is independent of the initial location as the wave packet is delocalized due to the reflections at the boundaries. In addition, this method of images can be used with any array that has parity-symmetric waveguide coupling. However, the analytic form of A_j changes with the form of the coupling function.

In addition to a single input, two waveguides can be simultaneously excited to create a state of the form

$$|\psi\rangle = \frac{1}{\sqrt{2}}(|j\rangle + e^{i\varphi}|k\rangle) \tag{3.9}$$

where j and k are waveguide index numbers where a single photon is injected into each site, and φ is the relative phase between the two inputs. This leads to interference patterns in the intensity evolution. Figure 3.8 shows intensity evolution for an initial

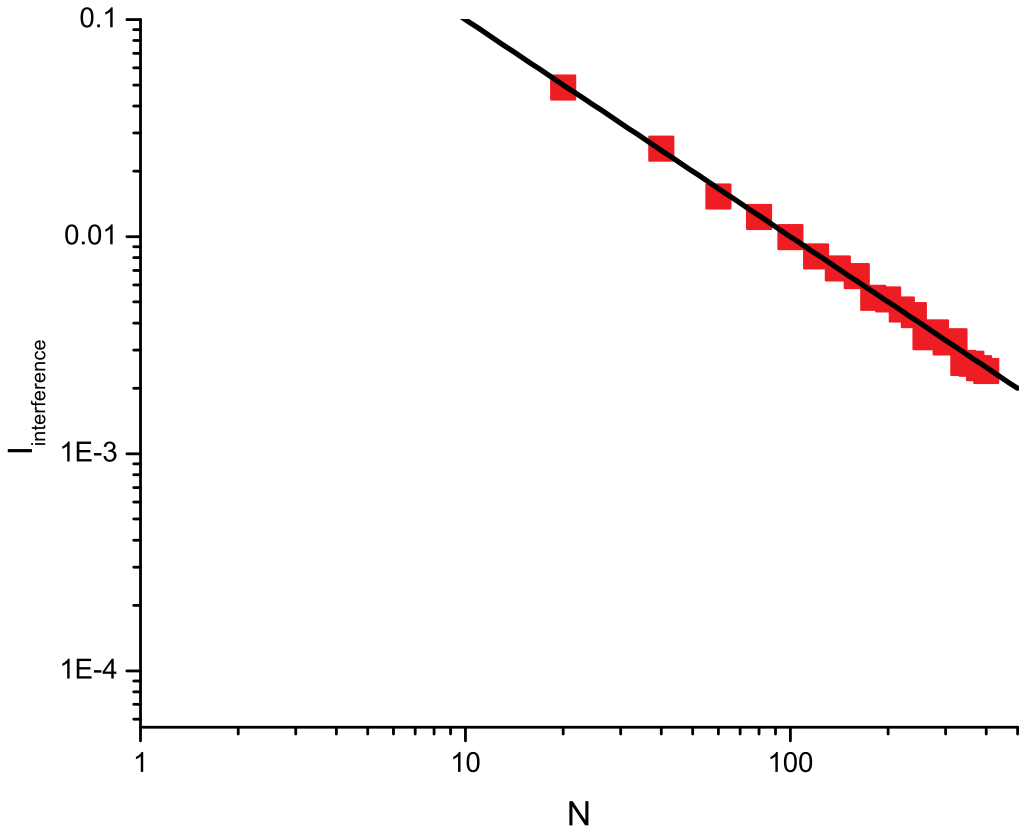

Fig. 3.7. $I_{interference}$ versus N when the wave packet has reached a steady state. The red squares are the calculated data points from Eq. (3.8) and the black line represents $I_{interference} = \frac{1}{N}$, which is agreement with the results from Eq. (3.8). The number of image pairs is $1,500$, $Ct = 10,000$, and $\alpha = 0$.

state of $|\psi\rangle = \frac{1}{\sqrt{2}}(|40\rangle + |60\rangle)$ where the relative phase between the two inputs is zero. Figure 3.8(a) shows that for $\alpha = 1$, the windows where the interference pattern is visible are periodic as a result of the periodic wave packet reconstruction that results from the linear energy spectrum. For $\alpha \neq 1$, the interference pattern is not visible at long times due to the wave packet delocalizing because of the interference created by

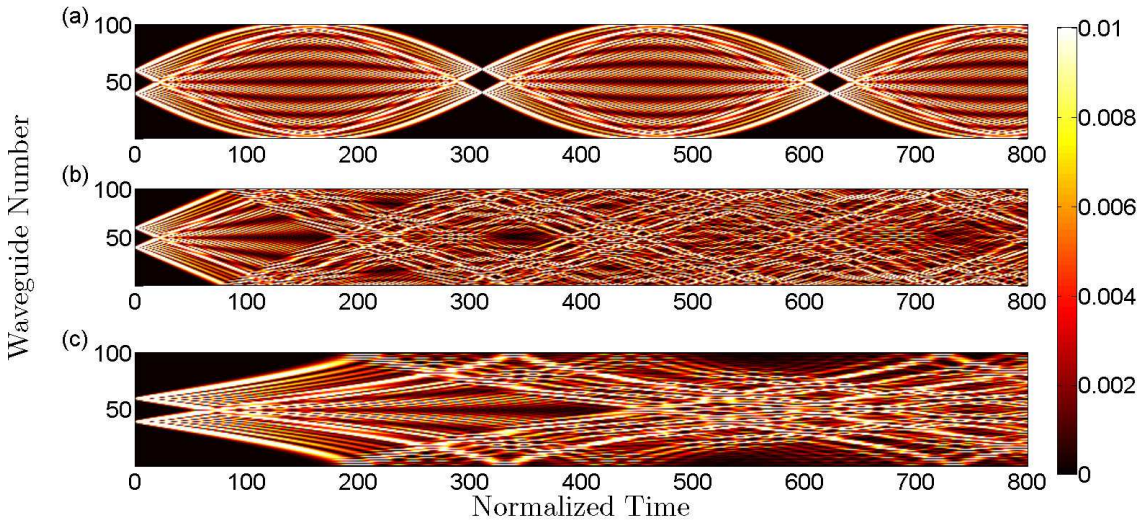

Fig. 3.8. Wave packet evolution as a function of the normalized time, t/τ_α, for (a) $\alpha = 1$, (b) $\alpha = 0$, and (c) $\alpha = -1$. The number of waveguides is 100 and the initial state is $|\psi\rangle = \frac{1}{\sqrt{2}}(|40\rangle + |60\rangle)$. Note that interference pattern that is visible only remains visible for $\alpha = 1$ as the wave packet delocalizes for $\alpha \neq 1$.

the array boundaries, as shown in Figures 3.8(b) and 3.8(c). This results from the energy spectrum being nonlinear for $\alpha \neq 1$.

3.3 Two-Particle Correlations

In addition to the interference patterns that are visible in the intensity evolution when two waveguides are initially excited, nontrivial quantum correlations are formed. The correlation function that is of interest is the two-particle (number) correlation defined as [51]

$$\Gamma_{pq} = \langle a_p^\dagger a_q^\dagger a_q a_p \rangle. \tag{3.10}$$

Silberberg and co-workers have experimentally explored these correlations in a periodic lattice using Hanbury Brown-Twiss (HBT) intensity-intensity correlations measurements [52]. These intensity-intensity correlation measurements were developed in 1956 by Robert Hanbury Brown and Richard Q. Twiss as a way to measure the

size of the star Sirius [53] and are heavily used in quantum optics [54]. For an array of waveguides, the HBT correlation measurements give the probability of detecting a photon at one waveguide while simultaneously detecting a second photon at another waveguide when two photons are injected simultaneously into the array. The HBT correlation measurements contain information about the quantum statistics of the particle; therefore, they can be used to differentiate between fermions and bosons. The correlation matrix that contains all the possible final states is

$$\Gamma_{pq} = |U_{pj}U_{qk} \pm U_{pk}U_{qj}|^2 \tag{3.11}$$

where U_{pk} is the unitary time-evolution operator and the initial waveguides are j and k. Note that $\pm$ corresponds to bosons and fermions, respectively. Lahini and co-workers have studied the quantum correlations extensively in a periodic lattice. They found initial separation of the states has a dramatic affect on the quantum correlations, which are encoded classical intensity-intensity correlations. The quantum correlations assume that the light that is detected at wavaeguides j and k come from different input whereas the classical correlations allow the possibility that the light detected could come from the same input. Injecting two photons into the same waveguide results in the quantum correlations being just the product of the probability distributions. When the photons are in adjacent waveguides, they bunch together and go to the same side of the array. However, when there is a waveguide separating the initial waveguides, the photons are either both at the edges of the array or both at the center of the array. This stark difference in quantum correlations is attributed to the $\pi/2$ phase difference between adjacent waveguides. For two electrons at adjacent lattice sites, they go to opposite sides of the lattice, and if there is a site separating them, one goes to the edge while the other one stays in the central region of the lattice. Thus, the type of particle produces a stark contrast in the two-particle correlations even though the probability distributions for a single particle are identical regardless of the type of particle [52].

When $\alpha = 1$, there exist windows when both bosons and fermions are localized near an edge when particles are initially at sites $j = 1$ and $j = 2$. Figure 3.9(a)

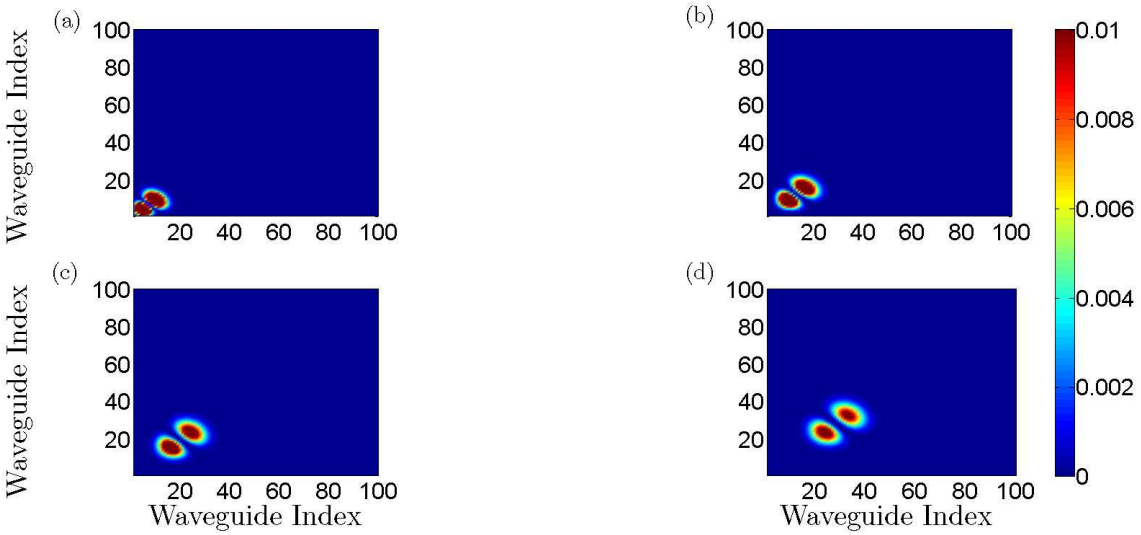

Fig. 3.9. Two-particle quantum correlations for bosons that are initially at sites $j = 1$ and $j = 2$ at times of (a) $t/\tau_\alpha = 50$, (b) $t/\tau_\alpha = 70$, (c) $t/\tau_\alpha = 90$, and (d) $t/\tau_\alpha = 110$. The waveguide array consists of $N = 100$ waveguides and $\alpha = 1$. The bosons are localized at all times and the location of where the bosons localizes oscillates back and forth between the lower left and upper right corners.

shows that when $t/\tau_\alpha = 50$ and the number of lattice sites is $N = 100$, the bosons are localized near the initial positions of the particles due to the periodic wave packet reconstruction. As the time evolves further, the two regions where the bosons localize move towards the opposite edge of the array. In addition, as the regions move towards the center of the array, they expand as a result of the spreading of the wave packet, as shown in Figures 3.9(b)-(d). Figure 3.10(a) shows that for $t/\tau_\alpha = 50$, the fermions localize near the initial positions. Note that a nodal region exists along the diagonal that goes from the bottom left corner to the upper right corner as the two fermions cannot be found at the same site due to the Pauli exclusion principle. Similar to the case when the particles are bosons, the localized regions move towards the other edge of the array and the area of the regions expands, as shown in Figures 3.10(b)-(d). In addition, the correlations are periodic in time regardless of the quantum statistics of

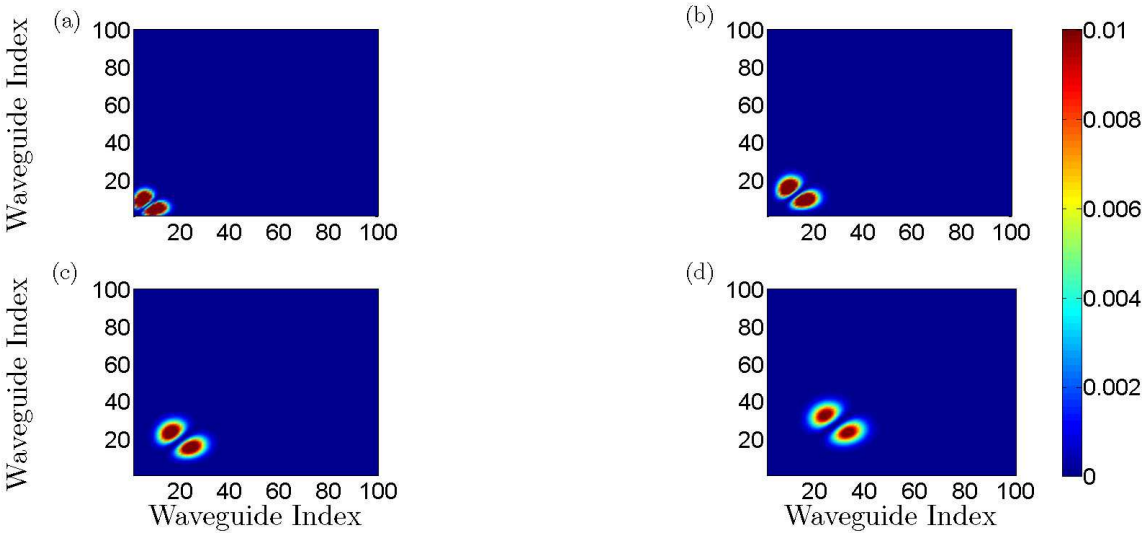

Fig. 3.10. Two-particle quantum correlations for fermions that are initially at sites $j = 1$ and $j = 2$ at times of (a) $t/\tau_\alpha = 50$, (b) $t/\tau_\alpha = 70$, (c) $t/\tau_\alpha = 90$, and (d) $t/\tau_\alpha = 110$. The waveguide array consists of $N = 100$ waveguides and $\alpha = 1$. The fermions are localized at all times and the location of where the fermions localizes oscillates back and forth between the lower left and upper right corners.

the particle as the wave packet undergoes periodic reconstruction that results from the linear energy spectrum for $\alpha = 1$.

For $\alpha = 2$, the energy spectrum is nearly linear, see Figure 3.2, and even though the wave packet dynamics are similar to the dynamics when $\alpha = 1$, the quantum correlations are very different. For two bosons at initially at sites, $j = 1$ and $j = 2$, the wave packet attempts reconstruction multiple times, until the interference from the boundaries delocalizes the wave packet. When the wave packet attempts the reconstruction a second time, the bosons are then localized near the initial sites. Figure 3.11(a) shows that a nodal region forms near the lower left hand corner separating the two regions where the particles are localized when $t/\tau_\alpha = 140$. As time evolves, this nodal region expands as the localized region that is farthest from the edge moves toward the center of the array and expands, as shown in Figure 3.11(b)-(d). When the particles are fermions, one localizes to the edge of the lattice while the other one

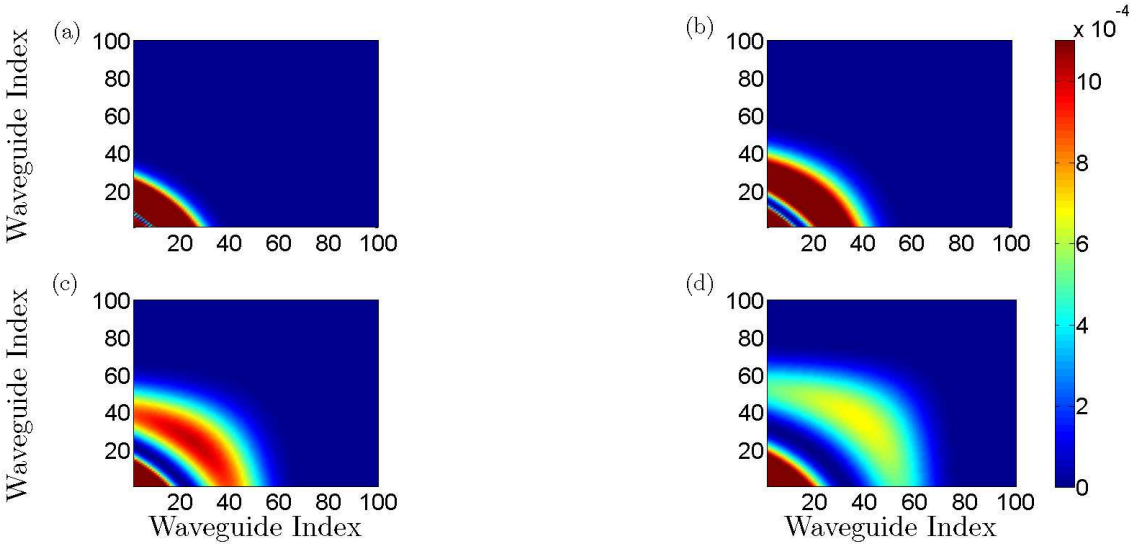

Fig. 3.11. Two-particle quantum correlations for bosons that are initially at sites $j = 1$ and $j = 2$ at times of (a) $t/\tau_\alpha = 140$, (b) $t/\tau_\alpha = 175$, (c) $t/\tau_\alpha = 200$, and (d) $t/\tau_\alpha = 225$. The energy spectrum is nearly linear as $\alpha = 2$ and the number of sites is $N = 100$. The bosons are localized near there initial positions as the wave packet attempts to reconstruct. The correlations show that a nodal region forms and seperates two areas where the correlation matrix is non-zero. As time evolves, the outer area and the nodal region both expand.

is in an extended state that is time-dependent, as shown in Figure 3.12(a). For a time of $t = 175\tau_\alpha$, the span is approximately 20 sites, while for times of $t/\tau_\alpha = 200$ and $t = 225\tau_\alpha$, the span is approximately 40 waveguides, as shown in Figures 3.12(b)-(d). In addition to the span of the extended states being time-dependent, the separation of the two fermions is also time-dependent as the separation increases with span of the extended state.

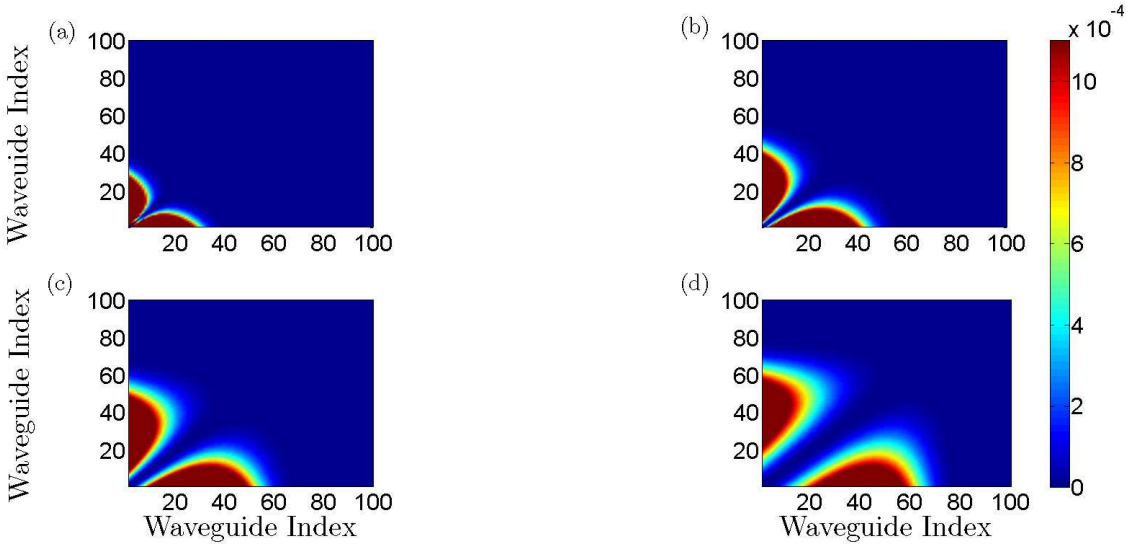

Fig. 3.12. Two-particle quantum correlations for fermions that are initially at sites $j = 1$ and $j = 2$ at times of (a) $t/\tau_\alpha = 140$, (b) $t/\tau_\alpha = 175$, (c) $t/\tau_\alpha = 200$, and (d) $t/\tau_\alpha = 225$. The energy spectrum is linear as $\alpha = 1$ and the number of site is $N = 100$. One fermion localizes near an edge while the other fermion is in an extended state. The range of this extended state as well as the area of localization are both time-dependent.

3.4 Conclusion

In this chapter, the evolution of light in a waveguide array with a waveguide coupling profile of $C_j = C(N(N-j))^{\alpha/2}$ has been explored. This lead to wave packet dynamics that have not been seen in traditional models as site-dependent waveguide coupling models have not been extensively explored. The parameter α was used to tune the wave packet dynamics as it controlled both the energy bandwidth, Δ_α and the shape of the energy spectrum.

Since the coupling strength varies with α, the inverse of the bandwidth was chosen as the characteristic time scale of the system. For $\alpha = 0$, the wave packet spread was the greatest in terms of the normalized time as the waveguide coupling was uniform throughout. When $\alpha = 1$, the wave packet underwent periodic reconstruction, which resulted from the linear energy spectrum of the system. This periodic reconstruction alternated between the initial waveguide and its parity-symmetric counterpart. When two waveguides were simultaneously excited and $\alpha = 1$, the interference pattern that was produced was also periodic. In addition, this periodic reconstruction was robust as the wave packet did not delocalize due the interference as it did for $\alpha \neq 1$.

Lastly, two-particle (number) correlation has been investigated for different values of α for both fermions and bosons. The correlations were found to be sensitive to both the shape of the energy spectrum and to the type of particle. For $\alpha = 1$, windows existed when both types of particles were localized near an edge and the area to which they localize was periodic in time as the energy spectrum was linear. When $\alpha = 2$, the correlations for fermions and bosons had stark differences. For fermions, there existed windows when one fermion was localized and the other was in an extended state. However, the correlations showed a nodal region for bosons and this nodal region separated two regions where the bosons localized.

4. DISORDER INDUCED LOCALIZATION

For many years it was thought that the introduction of disorder, i.e. impurities, into a metal would cause its conductivity to undergo a slow transition from a conductor to an insulator following the Drude model [2]. The Drude model was introduced in 1900 by Paul Drude to explain electrical transport properties [55]. According to the Drude model, the introduction of disorder into the metal decreases the electron's mean free time between collisions, which results in a lower conductance for the metal [2]. In 1958, P. W. Anderson introduced a new model for how introduction of disorder changes the electrical conduction. He proposed that for a critical amount of disorder, the metal undergoes a sharp transition from a conductor to an insulator. For a disorder free metal, the electron is free to move in any direction. With the introduction of disorder, scatterers are present in the model. These scatterers create closed paths for the electrons such that it will return to its initial position. The closed path and its time-reversed counterpart constructively interfere and as the number of scatterers increase, the probability for the electron to remain at its initial location increases. This results in the conductivity of the metal decreasing as the electron starts to localize to its initial position. Ioffe and Regel predicted that this transition occurs when the mean free path length is smaller than the electron's Compton wavelength [56]. Abraham and co-workers showed that only when the number of dimensions for the material exceeds two does the material undergo a true phase transition [57].

This localization, known as Anderson localization, is the result of the interference from all possible scattering paths and is a wave phenomenon [23]. For an infinite one-dimensional lattice, the electron localizes instantaneously for an infinitesimal amount of disorder in the lattice. When the lattice is finite, the electron does not localize instantaneously for a given disorder. This results from a finite number of scatterers and a finite disorder strength. Increasing the number of scatterers or the disorder

strength decreases the amount of time it takes the electron to localize [58]. The two main assumptions Anderson made were that the particles are non-interacting and that the disorder was time-invariant [59]. If the disorder is time dependent, the localization breaks down and classical diffusion is achieved [60] and this has been experimentally observed [61].

Anderson localization, a wave phenomenon, has been observed in a wide range of systems and has been studied extensively in the last 50 years [62]. One such system where Anderson localization has been experimentally observed is acoustic propagation in water. Weaver and co-workers used two inhomogeneous parallel plates and a point source to generate an acoustic wave; they found a concentration of energy around the point source that is slow to decay [63]. In addition to acoustic systems, Anderson localization has also been observed in ultracold atoms. Aspect and Inguscio observed Anderson localization in a potassium-39 BEC by obtaining a speckle pattern of the BEC. The disorder was introduced through the arrangement of the lasers that created the optical lattice [64]. Another system that can exhibit Anderson localization is a photonic crystal [65, 66].

In recent years, Lahini and co-workers observed Anderson localization in an array of evanescently coupled waveguides where the waveguides are uniformly spaced. They introduced disorder through the index of refraction for each waveguide by randomly adding impurities during the fabrication process. This resulted in the linear propagation constant being randomized and time-invariant. They experimentally achieved averaging over different realizations by injecting light into the farthest waveguide to left and recorded the output distribution. They then excited the adjacent waveguide on the right and recorded the intensity distribution and they repeated this process until every waveguide was individually excited. By averaging all of the output intensity distributions together, they achieved a disorder averaged intensity profile. They observed that as the disorder is increased in the array, the ballistic propagation of the light is suppressed and light localizes to the initial waveguide [67].

In addition to observing the intensity profile when the light undergoes localization, they have also investigated the effects of disorder on the energy spectrum. They used the Hanbury Brown-Twiss (HBT) correlations to gain information about the symmetry of the energy spectrum. This results in the randomization of either the propagation constant or the waveguide coupling as they produce similar intensity distributions. They observed that oscillations in the HBT correlations correspond to a symmetric energy spectrum. They found that randomizing the waveguide coupling constant preserves the symmetry while randomizing the linear propagation constant destroys this symmetry [68]. They have also investigated the dependence that the HBT correlations have on the quantum statistics of particle when there is disorder present as the probability profiles for both fermions and bosons are identical when a single particle is on the lattice. They found that signatures of the quantum statistics of particles survive the scattering from the disorder. The fermions exhibit a flat interparticle distance probability while the interparticle probability is oscillatory for bosons.

This chapter focuses on the effects that time-invariant disorder has on the evolution of a wave packet propagating through an array of evanescently coupled waveguides. In particular, the evolution in an array with a non-uniform, parity-symmetric waveguide coupling is of interest as the disorder free dynamics are tunable through the coupling profile. Additionally, how non-Hermitian but $\mathcal{PT}$-symmetric disorder affects the symmetry of the energy spectrum is investigated. Lastly, the quantum statistics of the output light are investigated for different input fields. The normalized variance and the site-to-site correlations are of interest for the different input fields.

4.1 Tight-Binding Model

In this section, light propagating in an array of N single-mode, evanescently coupled waveguides is described by a tight-binding Hamiltonian given by

$$\hat{H} = \sum_{j=1}^{N} \beta_j a_j^\dagger a_j + \sum_{j=1}^{N-1} C_\alpha(j)(a_{j+1}^\dagger a_j + a_j^\dagger a_{j+1}) \tag{4.1}$$

where β_j is the linear-propagation constant at site j, $\hbar = 1$, and $C(j)$ is the coupling constant between waveguides j and $j+1$. The parity symmetric coupling function of the form from the previous chapter

$$C_\alpha(j) = C[j(N-j)]^{\alpha/2}. \tag{4.2}$$

is chosen. The Hermitian disorder is introduced through random variations of the linear propagation constant β_j. The mean value of β_j is irrelevant as long as it is the same for each waveguide. Thus, it is set to zero. To investigate how the form of the disorder distribution affects the rate of localization, the intensity profiles for a uniform distribution of the form

$$P(\beta_j) = \begin{cases} \frac{1}{2\Delta} & \text{if } \beta_j \leq \Delta \\ 0 & \text{if } \beta_j > \Delta \end{cases} \tag{4.3}$$

and a Gaussian distribution of the form

$$P(\beta_j) = \frac{1}{\sqrt{2\pi\sigma^2}} \exp\left(\frac{-\beta_j^2}{2\sigma^2}\right) \tag{4.4}$$

are compared for a given propagation time. Figure 4.1(a) shows the output intensity profile for a propagation time of $Ct = 20$, $\alpha = 0$, and no disorder present in the array. The number of waveguides in the array is $N = 100$, with $\alpha = 0$, and the initial position in the array is $j = 50$. This shows that the light undergoes ballistic propagation as the outer lobes of the profiles have the highest intensity and this is a signature of a quantum random walk [18]. Figure 4.1(b) shows when $\Delta = \sigma$, more light is localized to the initial waveguide for a Gaussian distribution (blue solid line) described by Eq. (4.4), than for a uniform distribution (red dashes) described by

Eq. (4.3). This results from disorder strength being unequal as the variance of the uniform distribution, $\frac{\Delta^2}{3}$, being a third of the variance for the Gaussian distribution, σ^2, if $\Delta = \sigma$. Figure 4.1(c) shows that they produce identical intensity profiles when the disorder strength is the same as both distributions have equal variances, $\frac{\Delta^2}{3} = \sigma^2$. Thus, the disorder induced localization is independent of the type of distribution given that it has the same mean and variance.

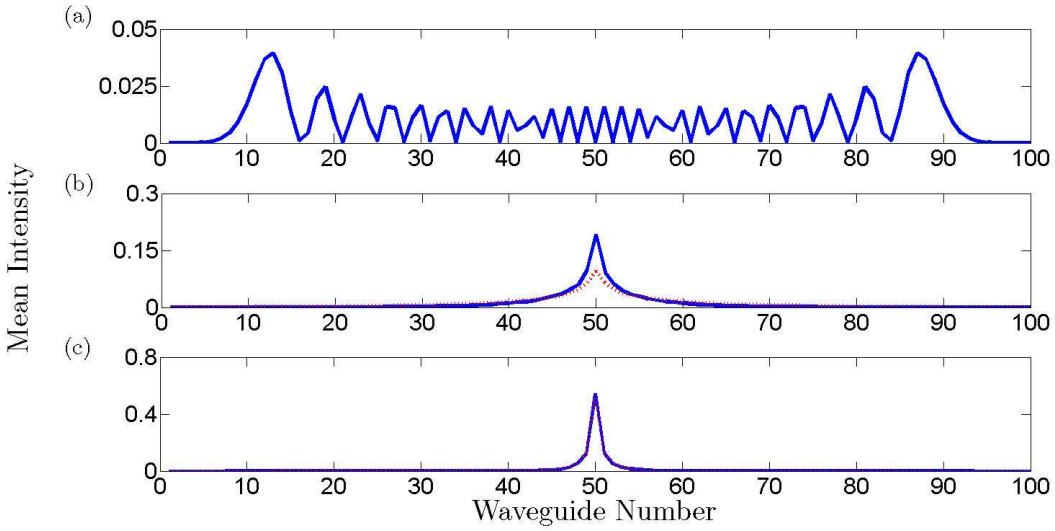

Fig. 4.1. Mean intensity versus waveguide number for an input at the 50^{th} waveguide, a propagation time of $Ct = 20$, a waveguide array consisting of $N = 100$ with $\alpha = 0$, and the number of disorder realizations $N_r = 10^3$. Note that panel (a) shows the ballistic propagation that arises from the discrete nature of a disorder free array and is a hallmark signature of a quantum random walk [18]. When the variances of different distributions are unequal, a higher amount of light localizes for the distribution with the larger variance as panel (b) shows. The intensity profile for a rectangular distribution (red dashes) with a variance of $\frac{C^2}{3}$ is plotted against the intensity profile a Gaussian distribution (blue solid line) with a variance of C^2. The variance for the Gaussian distribution is higher, which results in more light remaining in the initial waveguide. When the variances for the distributions are equal, the intensity profiles are indistinguishable as panel (c) shows when both variances are $9C^2$. Note that the means of both distributions are set to zero.

As the mean and variance characterize a Gaussian distribution, it is the distribution that is used for the rest of the chapter unless noted otherwise and the random disorder is generated using the Box-Mueller algorithm with zero mean and the desired variance [69]. Note that as the coupling strength increases with α, a given amount of physical disorder localizes a smaller amount of light as α increases. Therefore, the disorder strength is normalized to the disorder free energy bandwidth, $\Delta_\alpha^{(0)}$. As mentioned in the previous chapter, $\Delta_\alpha^{(0)} \sim N^\alpha$ for $\alpha \geq 0$ and $\Delta_\alpha^{(0)} \sim N^{-|\alpha|/2}$ for $\alpha < 0$. In addition, the inverse of the bandwidth is chosen as the characteristic time-scale for the system, $\tau_\alpha(N) = \frac{1}{\Delta_\alpha(N)}$, as the wave packet dynamics occur on physically different time scales. The number of disorder realizations is varied to show that results are independent of the number of realizations once a sufficient amount of averaging is reached.

4.2 Wave Packet Evolution in the Presence of Disorder

This section begins by investigating the effect a non-uniform, parity-symmetric coupling has on the localization of light inside the waveguide array. This is done by calculating the α dependence of the fraction of the total light intensity that remains in the initial waveguide for two different disorder strengths. In addition, the input location of the light in the array is varied, as the relative coupling strength is position-dependent. This allows for investigation into whether a global variable, such as the energy bandwidth, or a local variable, such as the local coupling constant is the proper choice for the disorder strength scale.

The top panel of Figure 4.2 shows the fraction of total intensity that remains in the initial waveguide as a function of α for $N = 100$, initial waveguides $j_0 = 50$ (blue circles) and $j_0 = 15$ (red squares), and disorder strength $\sigma/\Delta_\alpha^{(0)} = 3$. When the initial waveguide is near the center of the array, for $\alpha < 0$, the localized fraction rapidly saturates as $|\alpha|$ increases, whereas for $\alpha \geq 0$, the localized fraction is approximately independent of α because relative coupling strength is nearly identical, $C_\alpha(50) \approx$

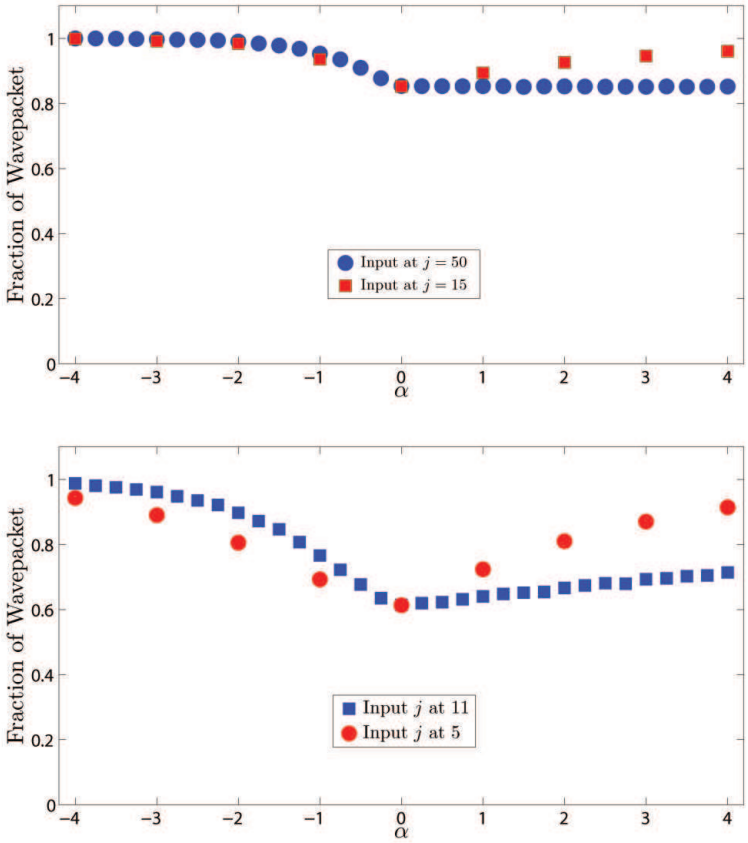

Fig. 4.2. The top panel shows the steady state intensity localized to the initial waveguide as a function of α for an array with $N = 100$ waveguides and $N_r = 10^6$ disorder realizations. The input is $j_0 = 50$ (blue circles) and $j_0 = 15$ (red squares), and the disorder strength is higher than the bandwidth $\sigma/\Delta_\alpha^{(0)} = 3$. The localized fraction is weakly dependent upon α as the relative coupling strength is nearly identical, $C_\alpha(50) \approx C_\alpha(51)$. When the input is moved away from the center, the relative coupling strength difference between adjacent waveguides becomes more pronounced for $\alpha > 0$. The fraction of the total intensity that remains in the initial waveguide increases with α as the relative coupling strength difference increases with α when $\alpha > 0$. The bottom panel shows corresponding results for an array with $N = 37$ waveguides, $N_r = 10^5$ disorder realizations, and a weaker disorder $\sigma/\Delta_\alpha^{(0)} = 1$. The localized fraction as a function of α depends acutely on different initial input, $j_0 = 11$ (blue squares) and $j_0 = 5$ (red squares), when the input locations are relatively close to the boundary. Again, this results from relative coupling strength difference being more pronounced between adjacent waveguides.

$C_\alpha(51)$. When the initial waveguide is near the edge, $j_0 = 15$, a clear dependence of the localized fraction on the coupling exponent α is visible. The bottom panel of Figure 4.2 shows the localized fraction as a function of α for a smaller disorder strength $\sigma/\Delta_\alpha^{(0)} = 1$, with a smaller number of waveguides $N = 37$ and different input waveguide locations $j_0 = 11$ (blue circles) and $j_0 = 5$ (red squares). In general, the α-dependence of the steady state localized fraction is sensitive to the proximity of the initial waveguide to an edge of the array as the relative coupling strength difference is more pronounced at the edges of the array. This result shows that the local variable coupling constant $C_\alpha(j_0)$ and not the clean-system energy bandwidth $\Delta_\alpha^{(0)}$, is the proper scale for the disorder strength. When $\sigma \gg \Delta_\alpha^{(0)}$, the localized intensity fraction in the initial waveguide is independent of α as the disorder completely suppresses the disorder free wave packet dynamics.

To examine the boundary effects when a weak disorder, $\sigma/\Delta_\alpha^{(0)} = 0.05$ is present in the array, the input location is near one edge of the array, $j_0 = 15$, with $N = 100$ waveguides. In addition, the dependence of the disorder averaged intensity profile on the value of α is of particular interest. Figure 4.3 shows that initially, the disorder free wave packet dynamics are visible for t/τ_α as the scattering is insufficient to completely suppress the spread. When $\alpha = 0$, the light localizes in initial waveguide with approximately twice the uniformly distributed intensity, where $I_{j_0} = 0.02$ and $I_{unif} = 1/N = 0.01$, as shown in Figure 4.3(a). Figure 4.3(b) shows that when $\alpha = 1$, the wave packet attempts periodic reconstruction twice before it localizes. Note that in contrast to the uniform array, the wave packet localizes in the initial waveguide and its parity-symmetric waveguide. This two-channel localization is the result of the competition between the destructive interference from the disorder and the constructive interference from the reflections at the boundaries. This two-channel localization is also present for $\alpha = 2$ and is a generic feature of the coupling profile having parity-symmetry, as shown in Figure 4.3(c). The relative intensities of the two channels can be varied with the disorder strength and increasing the disorder strength further results in the peak at the parity-symmetric waveguide vanishing.

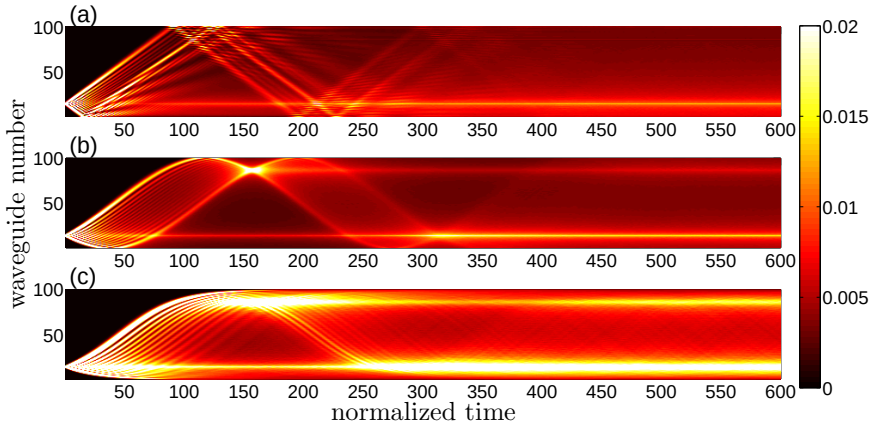

Fig. 4.3. α-dependent disorder averaged intensity $I(j,t)$ for an input at $j_0 = 15$ in an array with $N = 100$ waveguides, a weak disorder $\sigma/\Delta_\alpha^{(0)} = 0.05$, and $N_r = 10^6$ disorder realizations. The horizontal axis in each panel indicates time in units of the characteristic time, τ_α. Panel (a) shows exponential localization with a single peak at the initial waveguide when the array has uniform,$\alpha = 0$, coupling. Panels (b) and (c) show corresponding results for $\alpha = 1$ and $\alpha = 2$ respectively. In each case, the reconstruction attempts are followed by emergence of steady state intensity profile $I(j)$ that has two peaks, one at the input waveguide j_0 and the other at its parity-symmetric counterpart, $N + 1 - j_0$. The relative weights at the two peaks can be tuned by the varying the weak disorder.

This two-channel localization is achievable in an array with uniform coupling, $C_\alpha(j) = C$, by decreasing the size of the array as the interference from the boundaries is approximately $1/N$. Figures 4.4(a)-4.4(c) show the intensity evolution for an initial position of j_0 in an array with $N = 20$ waveguides that are uniformly coupled with $N_r = 2,000$ disorder realizations. When the disorder, $\sigma = 0.04C$, is much smaller than the energy bandwidth, $\Delta^{(0)} \approx 4C$, the light partially localizes in the initial waveguide, j_0, as well as in the parity-symmetric waveguide, $N + 1 - j_0$. This results from the constructive interference that results from reflecting multiple times off the edges of the array as Figures 4.4(a) and 4.4(d) show. Increasing the disorder further results in the amount of light in the parity-symmetric waveguide decreasing, as more light localizes in the initial waveguide due to the increase in the scattering that the light undergoes, see Figures 4.4(b)-4.4(d). Figure 4.5 shows the disorder averaged intensity evolution in an array with $\alpha = -1$ when a weak disorder is present in the array, $\sigma = 0.0125\Delta_\alpha^{(0)}$, and the number of disorder realizations is $N_r = 1,000$. In addition, when the array is free of disorder, bound states exists at the edges and these bound states are suppressed by the interference from the disorder. Additionally, the light localizes at the initial waveguide, $j_0 = 3$, and its parity-symmetric counterpart, $N + 1 - j_0 = 18$. This two channel localization is observable in any waveguide array with parity-symmetric waveguide coupling when the disorder is weak, $\sigma \ll \Delta_\alpha^{(0)}$.

To further investigate how the boundaries affect the wave packet evolution in the presence of disorder, periodic boundary conditions are now applied to the waveguide array such the light can tunnel directly from waveguide $j = 1$ to waveguide $j = N$, which is denoted by C_N. Figures 4.6(a)-(c) show the intensity evolutions when the waveguide coupling uniform throughout the array, $C_N = C$. This is analogous to the reflection coefficient at the array boundaries being zero, as the light is no longer reflected towards center of the array when it reaches the edges of the array. The initial location is $j_0 = 3$ in an array with $N = 20$ waveguides. Figure 4.6(a) shows that for a disorder of $\sigma/C = 0.04$, the light partially localizes at the initial waveguide, j_0, and the anti-podal waveguide, $\frac{N}{2} + j_0$ with $N_r = 1,000$ disorder realizations. The location

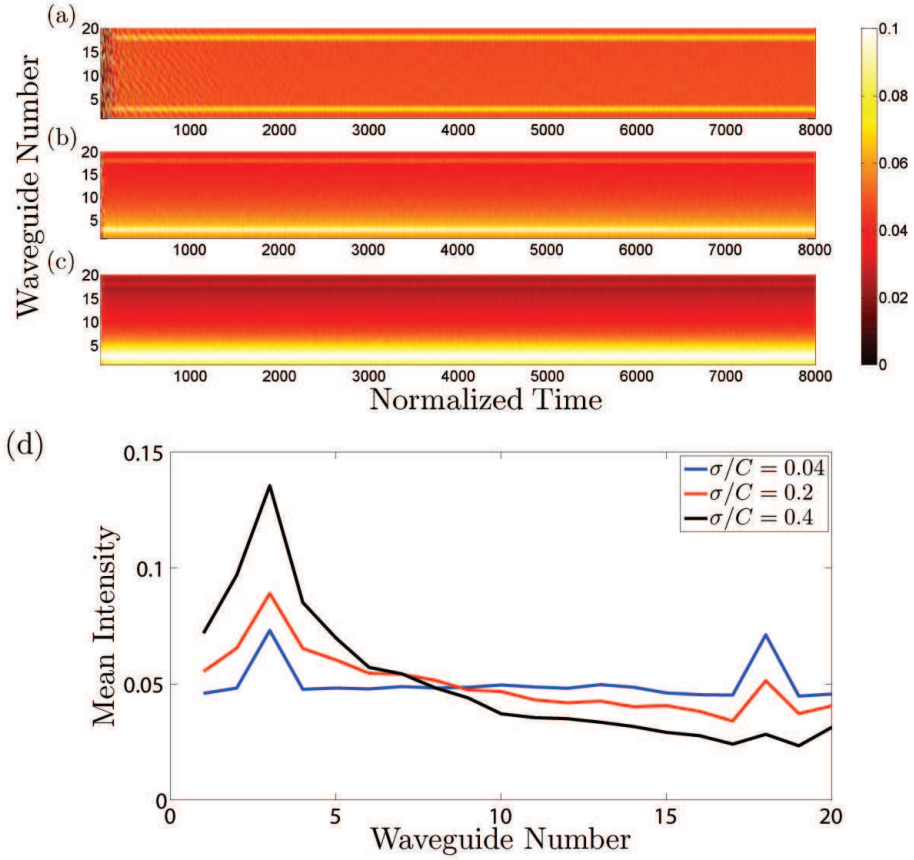

Fig. 4.4. Disorder averaged intensity evolutions with $N = 20$ waveguides for disorder strengths of (a) $\sigma/C = 0.04$, (b) $\sigma/C = 0.2$, and (c) $\sigma/C = 0.4$. The initial state is $|\psi(t = 0)\rangle = |j_0 = 3\rangle$. Panel (d) shows the steady state intensity profiles for $\sigma/C = 0.4$ (blue line), $\sigma/C = 0.2$ (red line), and $\sigma/C = 0.04$ (black line). Note that will localize in the initial waveguide, $j_0 = 3$, and its parity-symmetric waveguide, $N + 1 - j_0 = 18$, due to the constructive interference from the light reflecting off the edges of the array. As the disorder increases, less light reaches the edges of the array and the amount of light that is localized at the parity-symmetric waveguide decreases while the amount that is localized to the initial waveguide increases. Note that the total intensity is conserved at all times as the waveguide array is assumed to be lossless.

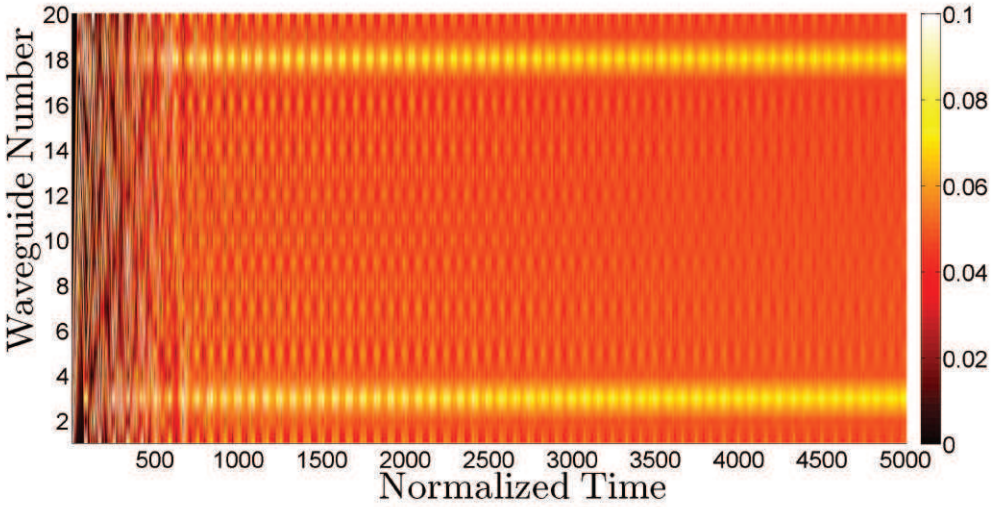

Fig. 4.5. Disorder averaged intensity evolution with $\alpha = -1$ and $\sigma = 0.0125\Delta_{\alpha}^{(0)}$ for an input at $j_0 = 3$. Note that the light localizes at the initial waveguide and the parity-symmetric waveguide $N+1-j_0 = 18$. This two channel localization results from the competition between the constructive interference from the edges of the array and the destruction interference from the disorder.

of this second peak results from the constructive interference between the two paths that light will take to transverse the array as both paths have identical path lengths. In addition, the interference pattern from the two paths remains visible for a weak disorder, as shown in Figure 4.6(d). Increasing the disorder decreases the amount of light that can propagate without scattering, which results in the intensity at the anti-podal waveguide decreasing, as shown in Figures 4.6(b) and (c). If the array consists of an odd number of waveguides, light only localizes in the initial waveguide as shown in Figure 4.7, as two paths that the light can traverse to any other waveguide have unequal path lengths.

For values of C_N/C that are between zero and one, the edges of the array are partially transmitting, the light localizes in four waveguides as a result of the constructive interference from the reflected and transmitted light. Figures 4.8(a)-(c) show that the

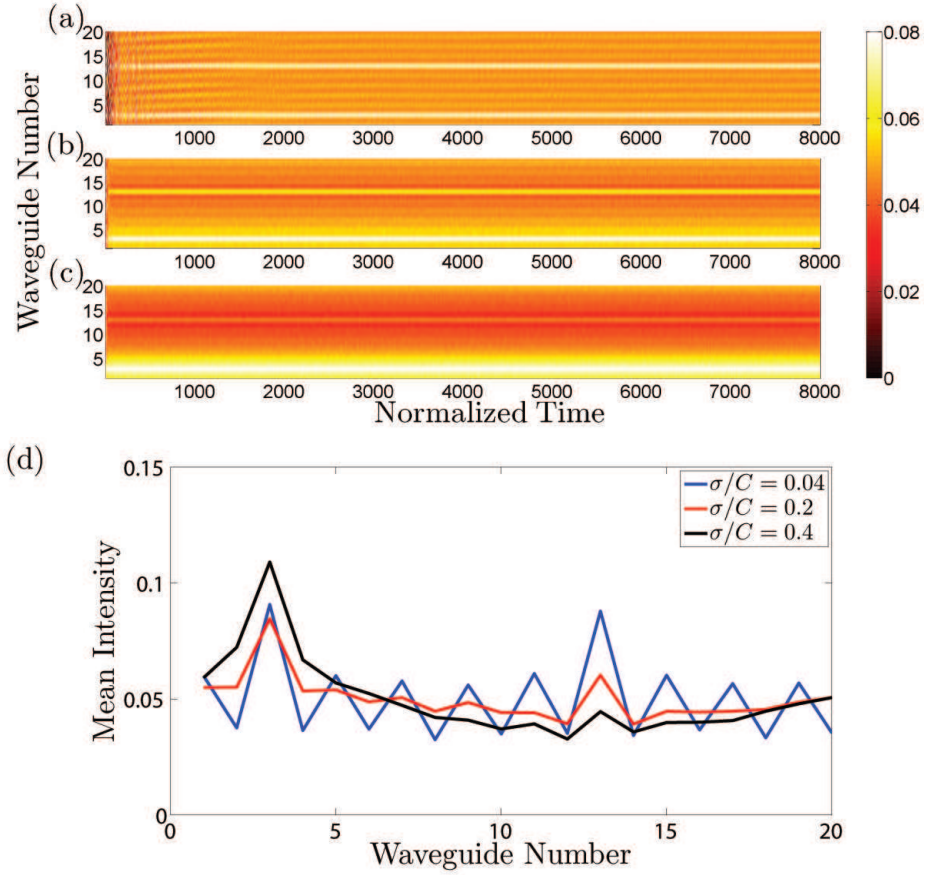

Fig. 4.6. Disorder averaged intensity evolutions with $N = 20$ waveguides for disorder strengths of (a) $\sigma/C = 0.04$, (b) $\sigma/C = 0.2$, and (c) $\sigma/C = 0.4$. The light localizes in the initial waveguide, $j_0 = 3$, and the anti-podal waveguide, $\frac{N}{2} + j_0 = 13$, as a result of constructive intference between the two possible paths that the light can travel. Panel (d) shows the steady state intensity profile for $\sigma/C = 0.04$ (blue line), $\sigma/C = 0.2$ (red line), and $\sigma/C = 0.4$ (black line). Note that as the disorder increases, the amount of light that localizes in the initial waveguide increases and the amount of light that localizes at the anti-podal waveguide decreases.

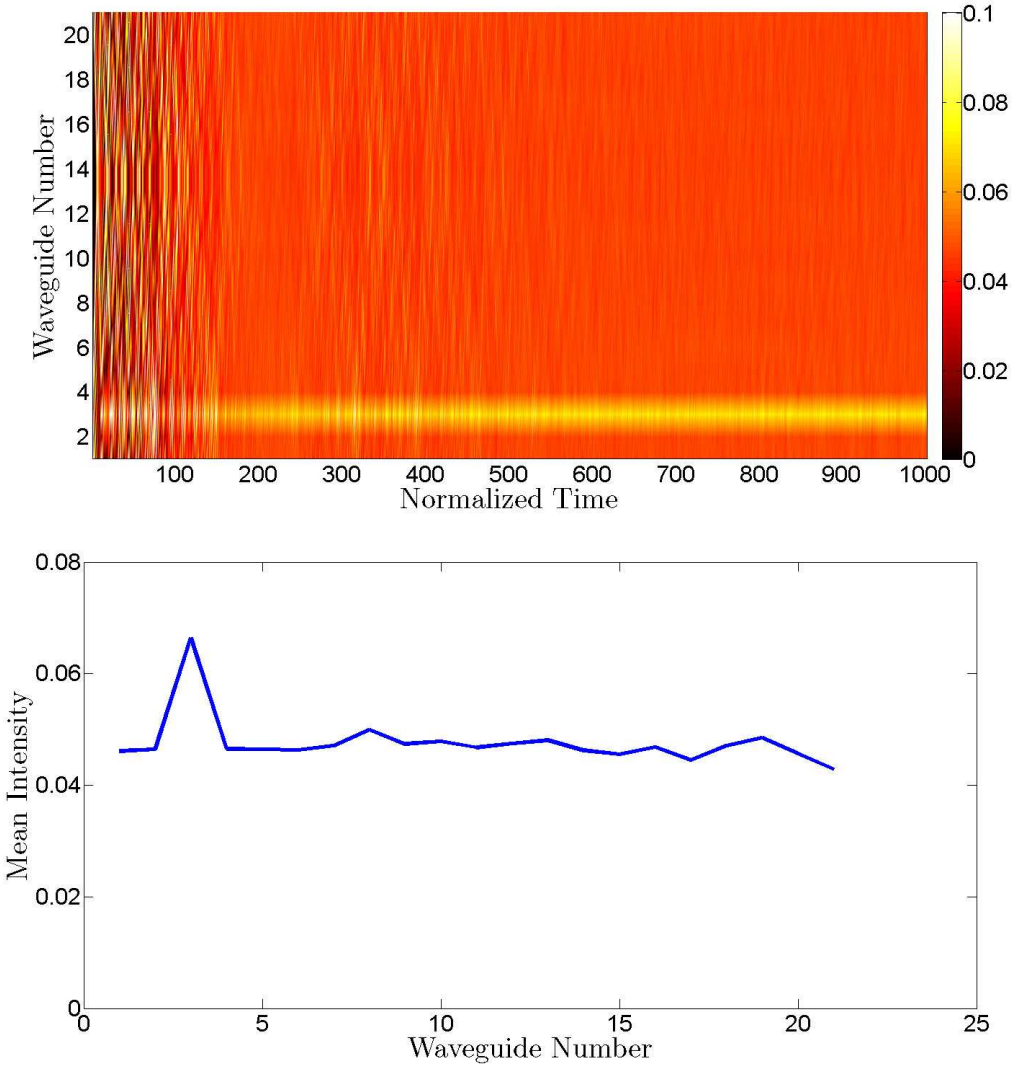

Fig. 4.7. Top panel is the disorder averaged intensity evolution with an array of $N = 21$ waveguides for disorder strengths of $\sigma/C = 0.04$. Bottom panel is the steady state intensity profile showing that for an array with an odd number of waveguides, light only localizes to the initial waveguide as the two possible paths that light travels to any other waveguide are not equidistant.

relative intensities of the four waveguides can be tuned through C_N with $\sigma/C = 0.04$ and $N_r = 1,500$ disorder realizations. For a value of $C_N = 0.3C$, there is a greater amount of light that localizes in the initial waveguide and its parity-symmetric waveguide than in the anti-podal waveguides, as shown Figure 4.8(a). Figure 4.8(b) shows that increasing the value of C_N increases the intensities at the anti-podal waveguides while the intensities at the initial waveguide and its parity-symmetric waveguide remain unchanged. Increasing the value of C_N further results in the intensities at the parity-symmetric waveguide and its anti-podal waveguide decreasing. In addition, intensity at the initial waveguide remains the same and the intensity at its anti-podal waveguide decreases as shown in Figure 4.8(c). Note that light localizes to four waveguides except when the initial position is the exact center of the array and when the initial position is equidistant from the edge of the array and its center. The center waveguide is also its parity-symmetric waveguide and its anti-podal waveguide is $j = 0$ for an array where the waveguide index is $j = 1, \cdots, N$. Therefore the light partially localizes only in the initial waveguide. An input at a waveguide that is equidistant from an array edge and the center of the array results in the light partially localizing in the initial waveguide and its parity-symmetric waveguide. This results from the fact that parity-symmetric waveguide is also an anti-podal waveguide.

So far, the primary interest of this chapter is evolution of a single particle that is injected into a single waveguide. In addition to exciting a single waveguide, multiple waveguides can also be excited simultaneously. By simultaneously exciting two waveguides, the light can produce interference patterns as well as non-trivial correlations. Bromberg and co-workers have investigated quantum and classical correlations when two photons are coupled either to the same waveguide or to adjacent waveguides [70]. In addition to disorder-free arrays, the quantum correlations have been studied in a disordered array by Lahini and co-workers [71]. The effects of disorder and α-dependent energy spectrum on an input wave packet that is localized to two waveguides with a relative phase θ between them are now explored. The phase θ determines the time-evolved intensity $I(j,t)$ in a clean array and for $\alpha = 1$, the phase information

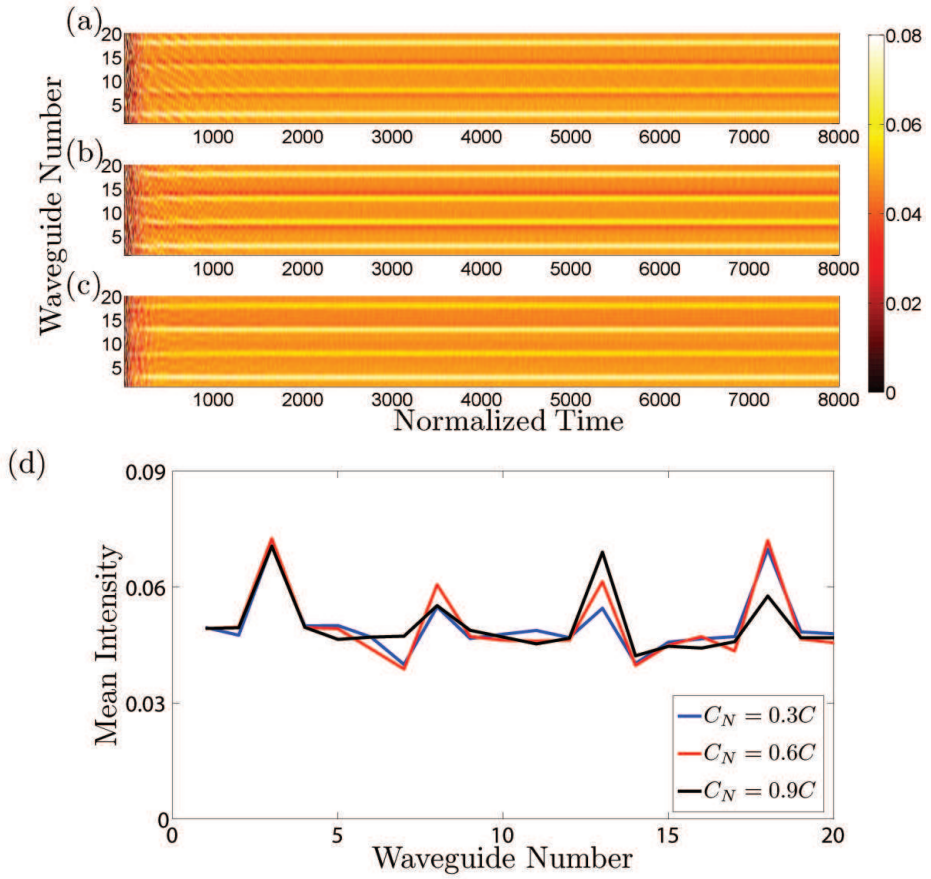

Fig. 4.8. Disorder averaged intensity evolutions with $N = 20$ waveguides for a disorder strengths of $\sigma/C = 0.04$ for an initial state of $|j_0 = 3\rangle$. The values for the coupling between waveguide $j = N$ and $j = 1$ are (a) $C_N = 0.3C$, (b) $C_N = 0.6N$, and (c) $C_N = 0.9C$. Panel (d) shows the steady state intensity profile for $C_N = 0.3C$ (blue line), $C_N = 0.6C$ (red line), and $C_N = 0.9C$ (black line). Note that light partially localizes in four waveguides due to the constructive interference that arises from the light partially reflecting off the edges of the array.

can be extracted from intensity measurements in periodic windows in time. Figure 4.9 shows the interplay between the phase θ and weak disorder, and their effect on the disorder-averaged steady state intensity profile for a non-uniform waveguide array with $N = 60$, $\alpha = 1$, and initial locations of $p = 20$ and $q = N - p = 40$.

The top panel shows the disorder-averaged intensity $I(j, t)$ for $\theta = 0$ (top), $\theta = \pi/2$ (middle), and $\theta = \pi$ (bottom) with a weak disorder, $\sigma/\Delta_\alpha^{(0)} = 0.05$, and $N_r = 10^5$. At short times $t/\tau_\alpha < 300$, the intensity shows clear signatures of θ-dependent interference and wave packet reconstruction due to equidistant energy levels of a clean $\alpha = 1$ system. At large times $t/\tau_\alpha \geq 100$, a steady state intensity profile with two peaks at initial waveguides $p = 20$ and $q = N - p = 40$ emerges. The three intensity profiles show that the phase information is encoded in the steady state intensity near the center of the waveguide array. The bottom panel shows the steady state intensity profile $I(j)$ at time $t/\tau_\alpha = 600$ as a function of the phase θ. The profiles for $\theta = 0$ (blue solid line) and $\theta = \pi$ (black dotted line) are marked by increased and suppressed intensity at the center of the waveguide array respectively, compared to when $\theta = \pi/2$ (red dashed line). Thus, the phase information, accessible only in certain periodic time windows in clean system, is accessible from the disorder-averaged steady state intensity profile. These results show that the steady state intensity $I(j)$ depends on the size of the array and relative phase θ between the two inputs, the coupling function α, and the proximity of the input state with the boundaries.

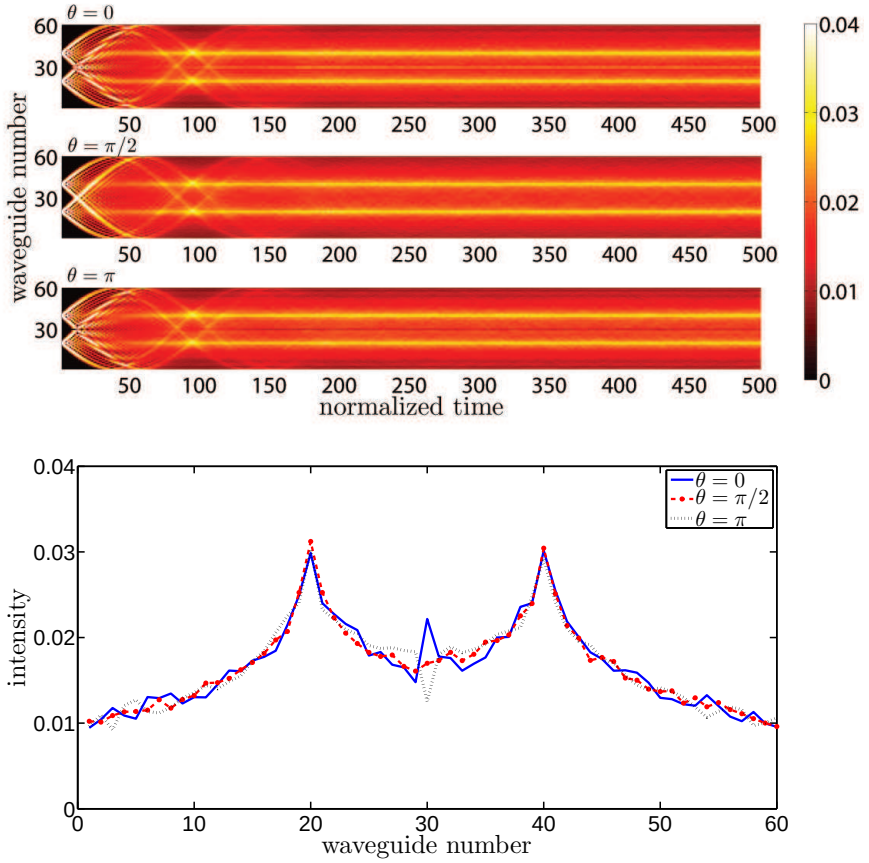

Fig. 4.9. Top panel shows intensity $I(j,t)$ as a function of θ for an array with $N = 60$ waveguides, disorder $\sigma/\Delta_\alpha^{(0)} = 0.05$, and $N_r = 10^5$ disorder realizations. The initial input state is $|\psi(0)\rangle = (|20\rangle + e^{i\theta}|40\rangle)/\sqrt{2}$. The top, middle, and bottom panels correspond to $\theta = 0$, $\theta = \pi/2$ and $\theta = \pi$ respectively. The interference pattern at short times $t/\tau_\alpha < 100$ is replaced by a steady state two peak intensity profile at times $t/\tau_\alpha \geq 100$. Bottom panel shows the corresponding steady state intensity $I(j)$ at $t/\tau_\alpha = 600$ as a function of phase θ. The intensity near the waveguide array center shows enhancement for $\theta = 0$ (blue solid line) and suppression for $\theta = \pi$ (black dotted line) when compared with the corresponding intensity for $\theta = \pi/2$ (red dashed line). In addition, the peak intensity is twice the average intensity $I_ave = 1/N \approx 0.0167$ for a single waveguide.

4.3 Intensity Correlations in the Presence of Disorder: Hermitian Versus Non-Hermitian Case

The previous section focused on localization due to a Gaussian, Hermitian disorder in the propagation constant. This results from the fact that the localization intensity profile is independent of the disorder origin (propagation constant or coupling constant) and disorder probability distribution as long as different distributions have zero mean and the same variance. Information about the origin of the disorder can be extracted from the higher-order intensity correlations; this is because an on-site disorder destroys the symmetry of the clean-system energy spectrum whereas a coupling disorder preserves it [68]. This section focuses on the exploration of the effects of a non-Hermitian, $\mathcal{PT}$-symmetric, on-site disorder on the intensity-intensity correlations. To this end, the Hamiltonian H is modified to include balanced gain ($i|\gamma|$) and loss ($-i|\gamma|$) terms [15, 72, 73],

$$H_{\mathcal{PT}} = H + \sum_{m=1}^{N} i\gamma_j (a_m^\dagger a_m - a_{\bar{m}}^\dagger a_{\bar{m}}) + \sum_m C_\alpha(j)(a_{j+1}^\dagger a_j + a_j^\dagger a_{j+1}) \tag{4.5}$$

where $1 \leq m \leq N/2$ is the position of gain waveguide and $\bar{m} = N + 1 - m$ denotes the index of the loss waveguide. The position-dependent coupling profile is given by Eq.(4.2), $C_\alpha(j) = C[j(N-j)]^{\alpha/2}$. Although $H_{\mathcal{PT}}$ is not Hermitian, it has purely real eigenvalues and relatively strong $\mathcal{PT}$ symmetric phase for $\alpha > 0$ [74]. The values of γ_m are random and uniformly distributed in such a manner as to preserve the $\mathcal{PT}$-symmetric phase of the system, which ensures the eigenvalues are purely real [75]. By comparing and contrasting the intensity-intensity correlations due to diagonal $\mathcal{PT}$-symmetric disorder and an off-diagonal Hermitian disorder in the waveguide coupling, information about how the impurities affect the energy spectrum is obtained. The disorder in the waveguide coupling is introduced via $C \to C[1 + \delta(j)]$ where the distribution for the random, position-dependent change $\delta(j)$ is a uniform distribution with zero mean and variance ς^2. By confining the limits of the uniform distribution

to weak disorder, this ensures that the scale-factor $1 + \delta(j)$ is always positive. The normalized, disorder-averaged, classical correlation matrix is defined as [68]

$$\Gamma_{jk}(t) = \frac{\langle I(j,t)I(k,t)\rangle}{\langle I(j,t)\rangle\langle I(k,t)\rangle} \tag{4.6}$$

where $I(j,t)$ is the intensity profile which depends upon the initial positions j and k. Note that $\langle\cdots\rangle$ indicates averaging over different disorder realizations. Since the $\mathcal{PT}$-symmetric Hamiltonian, Eq. (4.5), is not Hermitian, the corresponding time-evolution operator is not unitary, and therefore the total intensity $\sum_j I(j,t)$ may not be conserved as this is an open system.

Traditionally, however, instead of the entire correlation matrix Γ_{jk} with $N^2/2$ independent entries, one considers the interparticle probability function $g(\Delta_r) = N^{-1}\sum_{j=1}^{N}\Gamma_{j,j+\Delta_r} = g(-\Delta_r)$ with N independent entries. This function is able to distinguish between diagonal propagation disorder and off-diagonal coupling disorder [68]. The left-hand column in Figure 4.10 column shows the normalized two-particle correlations for (a) on-site $\mathcal{PT}$-symmetric disorder and (c) real valued, off-diagonal disorder where $\alpha = 0$. The stark differences in the normalized HBT correlations are result of the system being open in panel (a) while for panel (c), the system is closed. The right-hand column in Figure 4.10 shows correlation functions, $g(\Delta_r)$, extracted from the steady state matrix Γ_{jk} for on-site $\mathcal{PT}$-symmetric disorder, panel (b), and off-diagonal coupling disorder, panel (d). Note the oscillations in the correlation function that are present in both cases. These oscillations indicate that the energy spectrum is symmetric about is center. If the energy spectrum is not symmetric about its center as in the case when on-site disorder is Hermitian, the oscillations are not present. The similarity between the two correlation functions, and their stark contrast with the corresponding correlation function for a Hermitian on-site disorder [68], shows that the symmetry of the energy spectrum of a disordered system, rather than the origin of the disorder, is instrumental in determining the properties of $g_(\Delta_r)$.

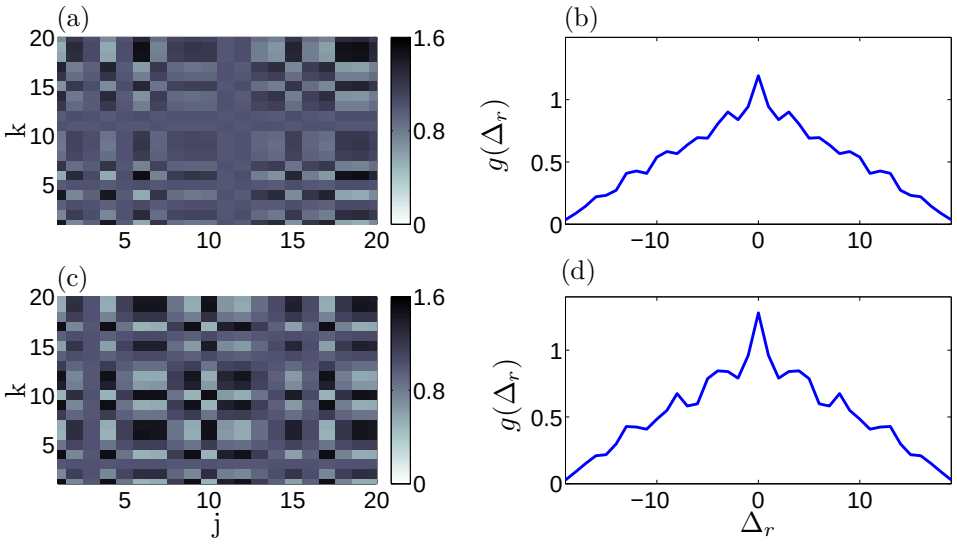

Fig. 4.10. Left-hand column shows the disorder-averaged, steady state, classical correlation matrix Γ_{jk} for a uniform array with $N = 20$ waveguides and a weak disorder $\sigma = \varsigma = 0.02\Delta_\alpha^{(0)}$; the results are averaged over $N_r = 10^4$ disorder realizations. The array is uniform, $\alpha = 0$, with $N = 20$ waveguides array with initial inputs at $j = 9$ and $j = 10$. The left-hand column in Figure 4.10 show the disorder-averaged, steady state matrix Γ_{jk} for $\mathcal{PT}$-symmetric, on-site disorder, panel (a), and coupling disorder, panel (c). Panel (a) shows the matrix for on-site, $\mathcal{PT}$-symmetric, non-Hermitian disorder; panel (c) shows the matrix for coupling, Hermitian disorder. The right-hand column shows the correlation functions $g(\Delta_r)$ extracted from the steady state, classical correlation matrix for on-site, $\mathcal{PT}$-symmetric disorder, panel (d), and off-diagonal, coupling disorder, panel (d). The similarity between the two results shows that the symmetry of the energy spectrum is instrumental to the correlation function properties.

4.4 Quantum Statistics of Anderson Localization

Lastly, the statistical aspects of Anderson localization of the output light for different input fields are of interest. To investigate how the statistics of the input fields affect the statistics of Anderson localization, a thermal field, coherent field, and a single-mode squeezed field are used as the input fields as they obey different statistics. The propagation of light inside the array is described by a tight-binding Hamiltonian given by

$$\hat{H} = \sum_{j=1}^{N} \beta_j a_j^\dagger a_j + \sum_{j=1}^{N-1} C(a_{j+1}^\dagger a_j + a_j^\dagger a_{j+1}) \tag{4.7}$$

where β_j is the linear propagation constant for waveguide j, $\hbar = 1$, and the waveguide coupling is uniform throughout. The disorder is introduced through the linear propagation constant and it follows a Gaussian distribution where Δ^2 is the variance of the distribution and the mean is zero as it is the same throughout the array and is therefore set to zero. The solutions to the Heisenberg equations for the operators a_j

$$i\frac{da_j}{dt} = \beta_j a_j + C_j(a_{j+1} + a_{j-1}) \tag{4.8}$$

can be written in terms of an input-output

$$a_j(t) = \sum_l G_{j,l}(t) a_l(t=0) \tag{4.9}$$

due to the linearity of the operators a_j. The Green's function G describes how the input transforms to the output and it depends on the parameters C and β_j and is random in nature due to disorder in β_j. Also, the Green's function in Eq. (4.9) depends on the propagation time, t, over which the light distribution evolves. All the physical quantities at the output would require averaging of the Greens function and its powers. The nature of the fields enters into Eq. (4.9) through the input $a_l(t=0)$.

One physical quantity that is measurable is the mean output intensity, I_j, at the output of the j waveguide and it is given by

$$I_j = \left\langle a_j^\dagger a_j \right\rangle = \sum_p \sum_q \langle G_{j,p}^* G_{j,q} \rangle \langle a_p^\dagger(t=0) a_q(t=0) \rangle \tag{4.10}$$

where the product of Green's functions is averaged over the realizations of β_j. For light injected into a single waveguide j_0 Eq. (4.10) simplifies to

$$I_j = \langle G^*_{j,j_0} G_{j,j_0} \rangle \langle a^\dagger_{j_0} a_{j_0} \rangle \tag{4.11}$$

where $|G_{j,j_0}|^2$ is the probability to detect light in waveguide j. In addition to mean output intensity, the fluctuations in the intensity at the output are also measurable. In 1963, Glauber introduced the function $g^{(2)}$ defined by

$$g^{(2)} = \frac{\langle a^{\dagger^2} a^2 \rangle}{\langle a^\dagger a \rangle^2} \tag{4.12}$$

which is called the degree of second-order coherence and it quantifies the intensity fluctuations [76]. Note that values of $g^{(2)}$ greater (smaller) than one correspond to bunching (antibunching) and $g^{(2)} = 0$ corresponds to perfectly coherent light [54]. Using Eq. (4.9), $g^{(2)}$ can be written in terms of the Greens function as

$$g^{(2)} = \frac{\langle |G_{l,0}|^4 \rangle \langle a_0^{\dagger^2} a_0^2 \rangle}{\langle G^*_{l.0} G_{l,0} \rangle^2 \langle a_0^\dagger a_0 \rangle^2} \tag{4.13}$$

Note that the quantum statistical quantity $g^{(2)}$ involves the averages of fourth powers of the Greens function.

The measurable quantities introduced above requires the nature of the input fields. For the input fields of interest, the quantities that are needed are given as follows:

for a coherent field,

$$\left\langle a_o^{\dagger^2} a_o^2 \right\rangle = |\alpha_o|^4 \text{ and } \left\langle a_o^\dagger a_o \right\rangle = |\alpha_o|^2 \tag{4.14}$$

for a thermal field,

$$\left\langle a_o^{\dagger^2} a_o^2 \right\rangle = 2n_0^2 \text{ and } \left\langle a_o^\dagger a_o \right\rangle = n_0, \tag{4.15}$$

and for a single-mode, squeezed field

$$\left\langle a_o^{\dagger^2} a_o^2 \right\rangle = \sinh^2 r(1 + 3\sinh^2 r) \text{ and } \left\langle a_o^\dagger a_o \right\rangle = \sinh^2 r. \tag{4.16}$$

In Eq. (4.16), r is the squeezing parameter. To compare final results for different input fields, all fields have the same average photon number, i.e. $n_0 = |\alpha_o|^2 = \sinh^2 r = 100$.

For the numerical results below, the array consists of 100 waveguides and the input light is coupled into the 50^{th} waveguide. The random disorder is generated using the Box-Mueller algorithm [69]. The output intensity is computed from the expression $I_j = \left\langle a_j^\dagger a_j \right\rangle$ where the angular brackets represent averaging over 1,000 realizations of the disorder and the quantum mechanical average over the input fields.

Figure 4.11(a) shows the mean intensity as a function of the waveguide position for all three input photon statistics when no disorder is present in the array. Increasing the disorder to $\Delta/C = 1$, suppresses the ballistic propagation and produces a narrow output intensity distribution, as shown in Figure 4.11(b). As the disorder increases further, the output field localizes faster due to increased scattering, until at a disorder of about $\Delta/C = 3$, all three output light patterns converge to a narrow distribution centered around the input waveguide, as shown in Figure 4.11(c). This characteristic property of Anderson localization has been used by Sapienza and coworkers to enhance radiation-matter interactions [77]. Note that each figure has three light distributions, but that the distributions for the three different field statistics are indistinguishable as the Green's functions control the probability to detect light at each output waveguide and are independent of the type of input field as they are only dependent on the parameters of the array and the propagation time.

Figure 4.12 shows the variance in the mean intensity of the output light at the 50^{th} waveguide for a Gaussian distribution for the disorder. It is seen that the variance in the intensity increases with disorder, as the amount of light that is localized at the initial waveguide increases. The variance is the largest for squeezed light, and least for a coherent field, which reflects the different variances of the input fields. Note that the magnitude of the variance in Figure 4.12 is sensitive to the mean number of input photons; however, the qualitative trends in the variance are similar.

To gain some additional insight on the fluctuation behavior of Anderson localization, the quantity, $g^{*(2)}$ (ratio of variance to square of the mean; $g^{*(2)} = g^{(2)}$ - 1) at the 50^{th} waveguide for different input photon statistics is shown in Figure 4.13. The mean photon number for all three inputs is 100. An interesting feature here

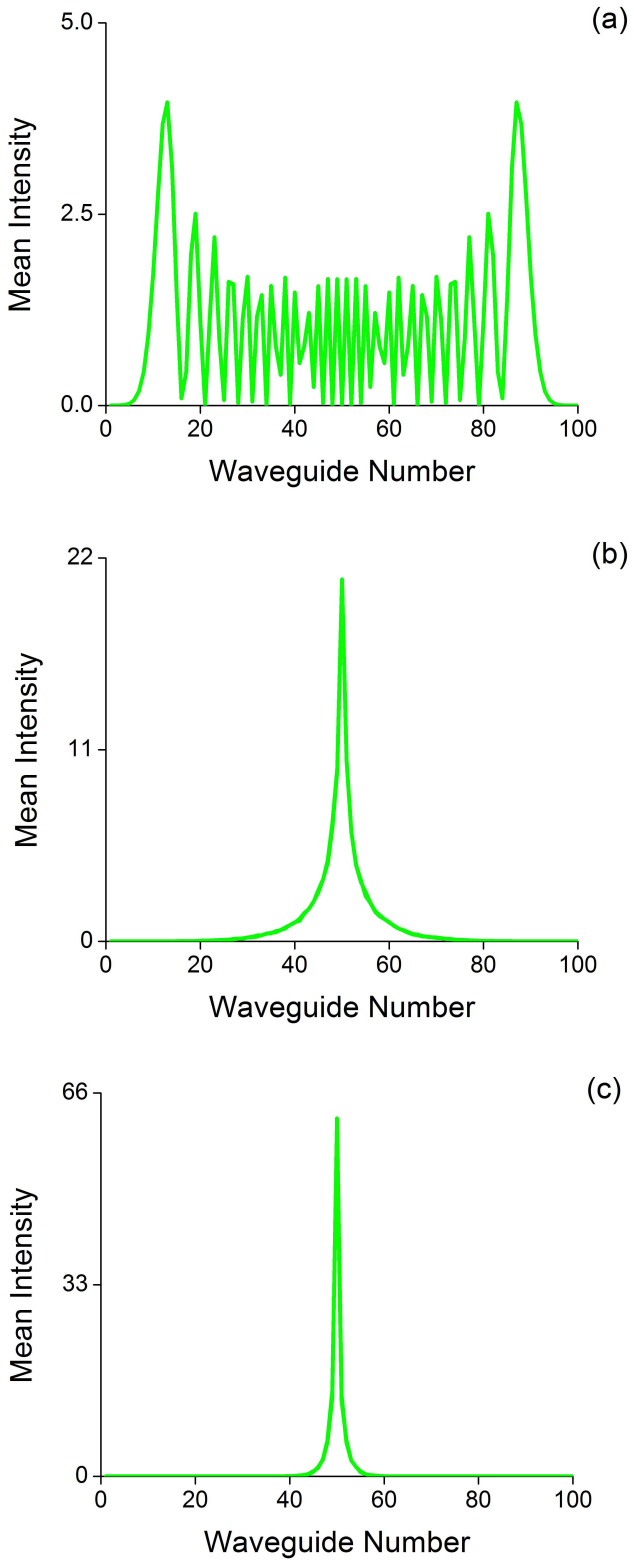

Fig. 4.11. Mean intensity versus waveguide number for disorders of (a) $\Delta/C = 0$, (b) $\Delta/C = 1$, and (c) $\Delta/C = 3$. Each plot shows three indistinguishable curves for the three different input photon statistics (coherent, thermal and squeezed). Mean photon number for all three input fields is 100 and $Ct = 20$.

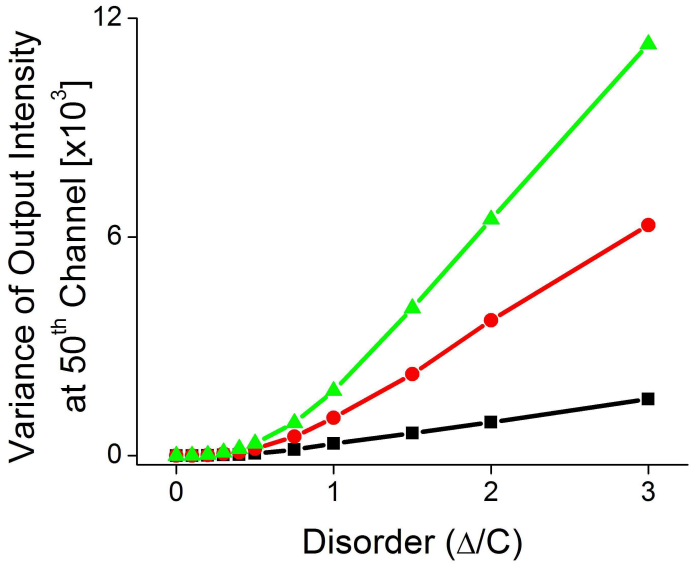

Fig. 4.12. Variance at the output of the 50^{th} waveguide versus disorder for a Gaussian disorder. Mean photon number for all three input fields is 100. Data shown are for input photon statistics of coherent field (black), thermal field (red) and single-mode, squeezed field (green).

is the enhancement of $g^{*(2)}$ by the disorder of the medium, which is a result of the suppression of the disorder-free wave packet dynamics. Consider the case of single-mode, squeezed light at the input. The normalized variance for the input light is 2, whereas it increases to more than 6 for a very small disorder. For higher disorders, i.e. after complete localization, $g^{*(2)}$ is still higher than for zero disorder. A similar enhancement of fluctuations is seen with thermal light, and to a smaller extent with coherent light input. Figure 4.14 shows the variance in the mean intensity at the 50^{th} waveguide as a function of the squeezing parameter for a disorder, $\Delta/C = 3$. For small values of r, a situation that is similar to having two photons, the variance is very small. However, with an increase in r, there is a rapid increase in the variance at the waveguide at which the Anderson localization occurs. In addition to the disorder enhancing the fluctuations of the output intensity, the disorder can also suppress the fluctuations. Consider the case when the input is a two photon Fock state. The $g^{(2)}$ function is the product of two ratios as shown in Eq. (4.13). The first ratio contains the Green's functions and provides information on the fluctuations that the disorder induces, whereas the second ratio contains the information about the type of input field. For coherent light, the second ratio is equal to 1 while for a two photon Fock state, it is equal to $\frac{1}{2}$. Thus, the normalized variance for the Fock state is smaller than for a coherent state. This result demonstrates an instance in which there is a suppression of the fluctuations due to the disorder by the nonclassical sub-Poissonian statistics of the input field.

In addition to the disorder enhancing the fluctuations of the output intensity, it minimizes uncertainty in the system. A measure of the uncertainty of the system is the entropy of the system [78]. The entropy of a classical system is defined as

$$S = -\sum_i p_i \ln p_i \tag{4.17}$$

where p_i is the probability for outcome i. For a system that is completely defined and has no uncertainty, the entropy is zero as one outcome has $p_i = \delta_{ij}$, where outcome j

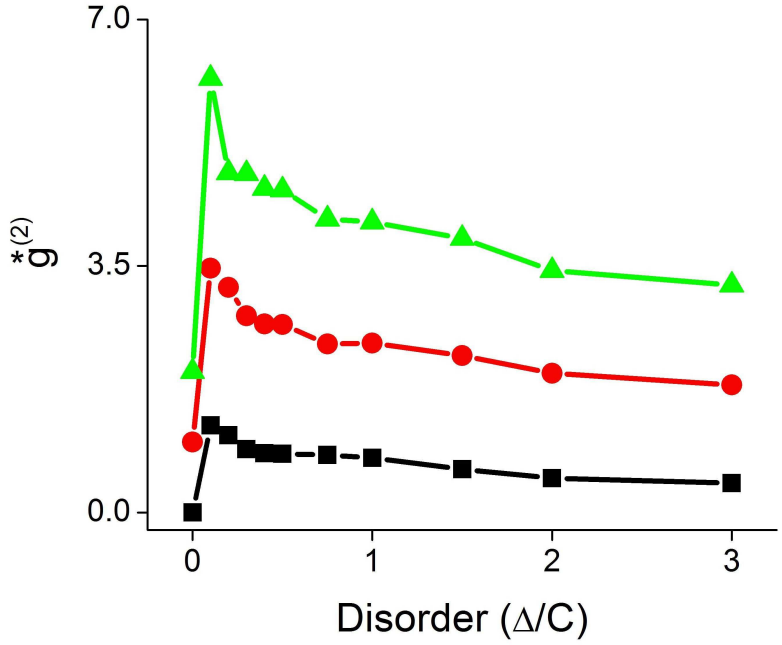

Fig. 4.13. Normalized variance versus disorder at 50^{th}waveguide for a Gaussian disorder. Mean photon number for all three input fields is 100. Curves shown are for coherent fields (black), thermal fields (red) and squeezed fields (green).

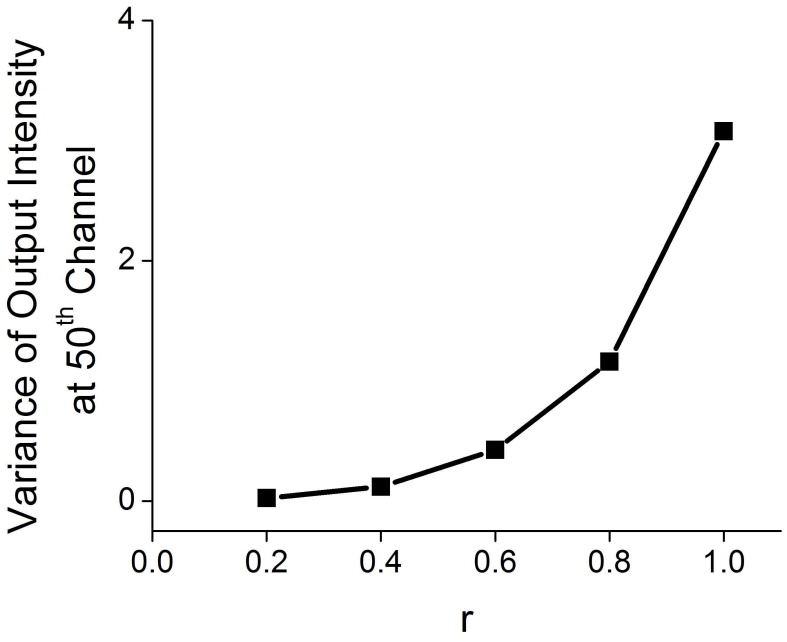

Fig. 4.14. Variance in output intensity at 50^{th} waveguide versus squeezing parameter with $\Delta/C = 3$.

is the only possible outcome. For a quantum mechanical system, the entropy of the system is given by the von Neumann entropy

$$S = -tr(\rho \ln \rho) \tag{4.18}$$

where ρ is the density matrix and tr denotes the trace. This definition of entropy has the same characteristics as the classical entropy, Eq. (4.17), in that for a pure state $S = 0$ and S is maximized when all possible states have equal probability [79]. The von Neumann entropy of a system that has undergone Anderson localization has been previously studied by Jia and co-workers for three dimensional and integer quantum hall systems [80]. The mean photon number is assumed to be one as then the intensity is identical to the probability distribution, $P_j(t) = |G_{j,j_0}(t)|^2$. Therefore, the disorder averaged von Neumann entropy is calculated as [80]

$$\langle S(t) \rangle = \langle \sum_j (|G_{j,j_0}(t)|^2 \ln(|G_{j,j_0}(t)|^2) - (1 - |G_{j,j_0}(t)|^2) \ln(1 - |G_{j,j_0}(t)|^2)) \rangle \tag{4.19}$$

where $\langle \cdots \rangle$ denotes averaging over the different realizations of disorder. Figure 4.15 shows the disorder averaged von Neumann entropy as a function of time and disorder strength with an array consisting of $N = 20$ waveguides and the initial position is $j_0 = 3$. Notice that entropy goes through a maximum as the disorder increases, which results from the suppression of the disorder-free wave packet dynamics.

To further probe the effect of input light statistics on the quantum statistical aspects of Anderson localization, site-to-site correlations defined by

$$\langle I_l(t) I_p(t) \rangle = \langle |G_{l,j_0}(t)|^2 |G_{p,j_0}(t)|^2 \rangle < a_{j_0}^{\dagger 2} a_{j_0}^2 > \tag{4.20}$$

are calculated for the case where the input light is a single-mode, squeezed field with a propagation time of $Ct = 20$ and an array consisting of $N = 100$ waveguides. For small r and no disorder in the medium, Figure 4.16(a), the magnitudes of the correlations are small, and it is apparent that in the absence of disorder, there is a good probability for the output photons to be in waveguides from 10 to 90. With an increase in the disorder, Figure 4.16(b) shows there is a superbunching of the photons into the

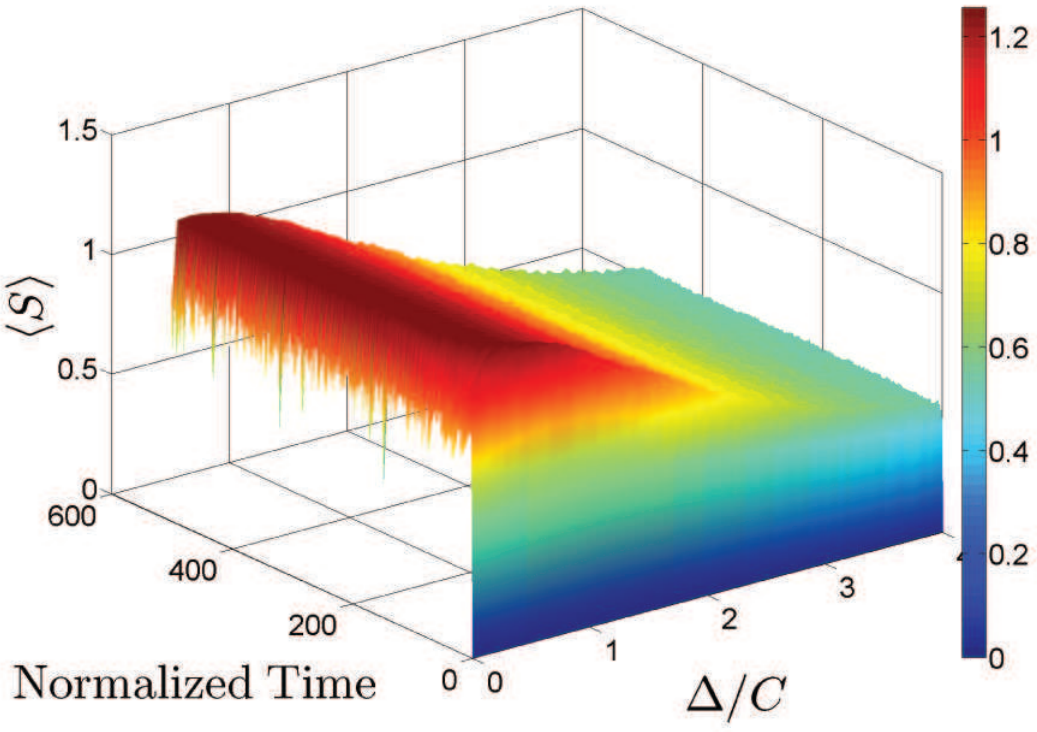

Fig. 4.15. Disorder averaged von Neumann entropy as a function of both normalized time and disorder. Note that for each disorder, $\langle S(t) = 0 \rangle$ as the input is into a single waveguide located at $j_0 = 10$ in array of $N = 20$ waveguides. Note that the entropy reaches a steady state when the wave packet reaches steady state. In addition, the entropy goes through a maximum as the disorder increases signifying that the suppression of the disorder-free wave packet dynamics.

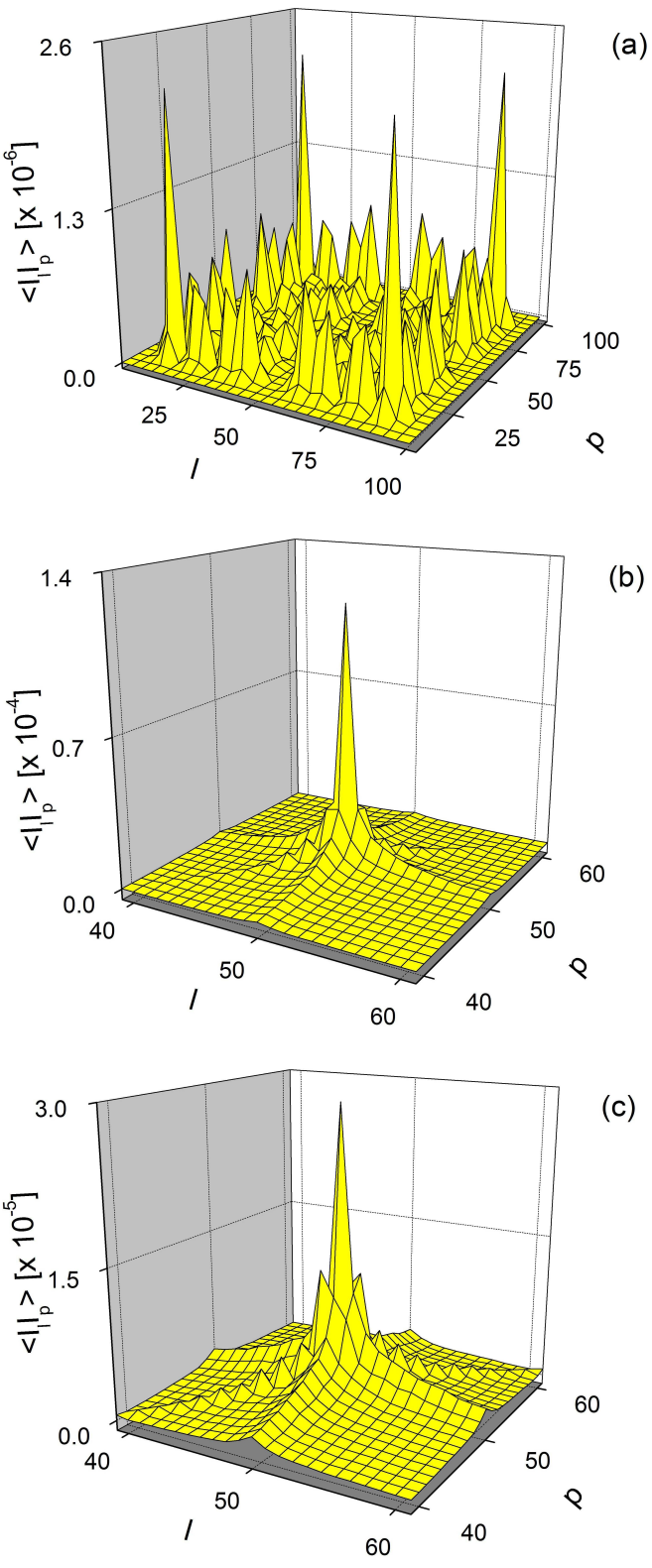

Fig. 4.16. Site-to-site correlation functions for (a) $r = 0.2$ and $\Delta/C = 0$, (b) $r = 0.2$ and $\Delta/C = 1$, and (c) $r = 1$ and $\Delta/C = 3$.

waveguide into which the input photons were launched, and a diminishing probability for the photons to be found in adjacent waveguides. Of course, the magnitudes of the correlations are still small, due to the small value of the squeezing parameter. In Figure 4.16(c) is the shown the site-to-site correlations for $r = 1$ and a disorder, $\Delta/C = 3$. The evidence for superbunching of the output photons is quite pronounced, and there is negligible probability of the photons spreading more than about five waveguides on either side of the 50^{th} waveguide.

To examine the statistical aspects of the output light even further, probability of the output light exiting the initial waveguide is investigated. As Figure 4.17 shows, the probability distribution of output light averaged over 10,000 realizations with a disorder of $\Delta/C = 3$ does not follow Gaussian statistics. The probability distribution for the output intensity is $P(I) = \frac{1}{<I>}e^{(-I/<I>)}$ if the light follows Gaussian statistics as the probability of detecting n photons follows a Poisson distribution and when $N \rightarrow \infty$, the limiting form of Poisson distribution is a Gaussian distribution [81]. This departure from Gaussian statistics results from the multiplicative noise that is in Eq. (4.8) as seen in the first term, $\beta_j a_j$. This departure from Gaussian statistics has been experimentally observed for randomly positioned scatterers in waveguides [82].

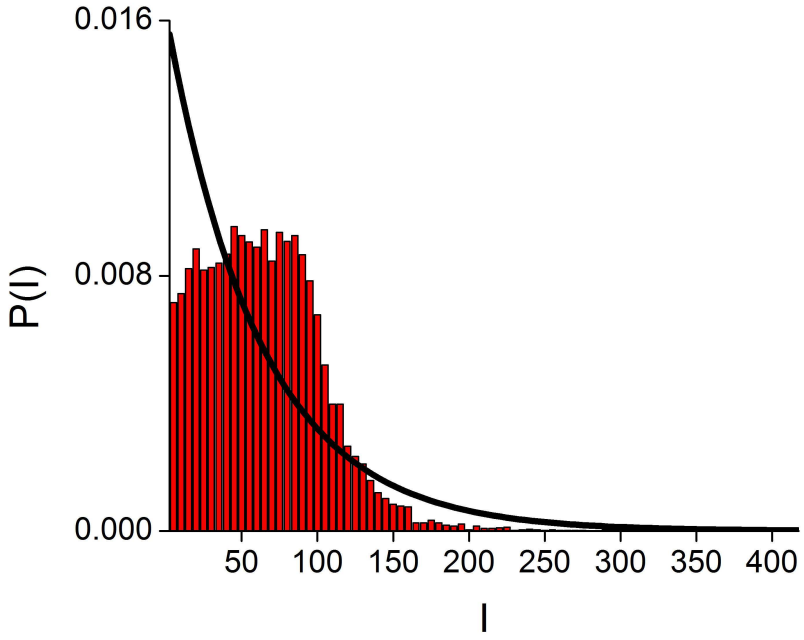

Fig. 4.17. Histogram shows the probability distribution for the output intensity at the 50^{th} waveguide when the input field is coherent with a mean photon of 100. $\Delta/C = 3$ and the medium's disorder is Gaussian. Black curve is the exponential distribution for the corresponding mean intensity.

4.5 Conclusion

This chapter explored the effects of disorder in waveguide arrays with non-uniform tunneling and non-Hermitian, on-site, $\mathcal{PT}$-symmetric disorder, by focusing on the behavior of disorder-averaged, steady state intensity profile and intensity-intensity correlations. It was found that the intensity profile $I(j,t)$ was acutely sensitive to the tunneling function C_α, the initial location of the input j_0, the array size, and proximity of the initial location to one of the edges. Additionally, it did not necessarily result in an exponential localization profile that is well known in uniform waveguide arrays [67]. In particular, it was found that when waveguide coupling was parity-symmetric and input state was localized to waveguide m_0, light localized in its parity-symmetric waveguide $N+1-m_0$, as well as its initial waveguide m_0.

The intensity peak at the parity-symmetric waveguide was the result of the competition between the interference that arose from the reflecting edges and the scattering due to the disorder. The relative heights of the two peaks were tunable through both the size of the array and the disorder strength as increasing the disorder strength suppressed the peak at the parity-symmetric waveguide, as less light reached the edges of the array. Additionally, the presence of this peak was independent of α and was a general result for any waveguide array with parity-symmetric waveguide coupling. For two inputs, the steady state intensity I_j encoded the phase-information from the two inputs for a weak disorder. In all cases, a strong disorder $\sigma/\Delta_\alpha^{(0)} \gg 1$, resulted in a localized intensity profile that was virtually identical to the initial intensity profile.

For a waveguide array with periodic boundary conditions, the wave packet evolution was found to be tunable through the periodic boundary conditions. When light was injected into a single waveguide and the edges of the array were partially reflecting, the light localized to four waveguides and the relative amount of light in the waveguides was tunable through the transmission of light at the edges for an array with an even number of waveguides. If the array had a odd number of waveguides,

light only localized to the initial waveguide as the path lengths for the two possible paths for the light to traverse the array had unequal path lengths.

Although the localization intensity profile is insensitive to the origin of the disorder, on-site or off-diagonal, higher-order intensity correlations depend upon it; in particular, Hermitian on-site and off-diagonal disorders lead to qualitatively different interparticle distance probability function $g(\Delta_r)$ [68]. Here, it was shown that a Hermitian disorder in the tunneling rate, and a non-Hermitian, $\mathcal{PT}$-symmetric, on-site disorder result in nearly identical correlation functions. Thus, the behavior of $g(\Delta_r)$ can be traced to the symmetry in the energy spectrum of a disordered Hamiltonian.

The last section of this chapter focused on how the statistics of the input fields affected the statistical aspects of Anderson localization. The three input field used were a thermal field, a coherent field and a single-mode, squeezed field. By numerically solving the Heisenberg equation for the field operators, relevant quantum statistical observables, such as the variance in the intensity fluctuations of localized light, site-to-site correlations and the Glauber $g^{(2)}$ function are calculated. We also compared the effect of the statistics associated with the disorder of the medium on Anderson localization and the associated quantum statistics.

By calculating the variance in the intensity fluctuations at the waveguide into which light localized, the fluctuations increased with disorder. The $g^{*(2)}$ function, the normalized variance, has a maximum for a finite disorder, before it tapers off for higher disorders to a value that was still greater than that for zero disorder. In addition, the entropy went through a maximum, which signified the suppression of the disorder-free wave packet dynamics. The site-to-site correlations showed that the probability of finding photons in waveguides that are adjacent to the one into which the input light was coupled diminished with increasing disorder. For sufficiently high disorder, superbunching of light occurred in the waveguide where the light localized and the output light was Gaussian even if the input light was coherent due to the multiplicative noise in the Heisenberg equation.

5. SUMMARY

In this dissertation, the evolution of light inside an array of evanescently coupled waveguides was investigated. In chapter 2, an all-optical model for phase-controlled photonic was presented. Starting with the tight-binding Hamiltonian that described the evolution of light inside the array, the propagation constant was linearly increased across the array. For a single waveguide excitation, the breathing modes of the system were visible. When adjacent waveguides were excited, the equations for $\langle j \rangle$ and $\langle j^2 \rangle$ are derived where j was the waveguide index number. These expressions were reminiscent of the equations for the mean momentum and mean energy for a system that exhibits ratchet motion. The model that described the ratchet motion was in coordinate space while for the waveguide array, it was in Fourier space. Thus, it required one to study the directed transport in site space, which was the natural space to study waveguides. The key element in achieving the directed transport was adjacent inputs that have a relative phase difference.

In chapter 3, the wave packet dynamics were investigated for an array with a site-dependent, parity-symmetric waveguide coupling profile of the form $C_\alpha(j) = [j(N-j)]^{\alpha/2}$. It was found that the shape of the energy spectrum was controlled by the parameter α. In addition, α also controlled the difference between the maximum energy and minimum energy. For $\alpha = 1$, the wave packet underwent periodic reconstruction as the energy levels have equal spacing, which was similar to the quantum harmonic oscillator. In addition, the phase information was visible in windows that were periodic while for $\alpha \neq 1$, the phase information vanished as the wave packet delocalized due to the interference from the edges of the array. When $\alpha < 0$, bound states existed at the edges of the array. In addition to the intensity evolution, the HBT correlations were also examined. They were found to be sensitive to the exponent of the coupling profile. For $\alpha = 1$, the correlations showed that for particles

at two adjacent sites, windows in time existed where the particles localized near an edge regardless of the type of particle. In addition, the locations where the particles localized oscillate in time because of the linear energy spectrum. When $\alpha = 2$, the correlations showed a distinction between fermions and bosons. For fermions, there existed windows when one fermion localized while the other was in an extended state. When particles were bosons, windows existed where they localized near one edge and a nodal region formed. This nodal region separated the regions where the bosons localized and it widened as the probability for the bosons to localize towards the center of the array increased.

Chapter 4 described the how disorder was introduced into the tight-binding model and how light localized because of this disorder. The amount of light that localized was independent of the type distribution for the disorder given that they have identical values for the mean and the variance. In addition, the introduction of disorder through either the propagation constant or the waveguide coupling produced similar light intensity profiles. When the waveguide array had a non-uniform but parity-symmetric coupling profile, it was found that the amount of light localized was dependent on the initial location due to the preferential direction for the tunneling. Additionally, it was found that the light localized to the initial waveguide and its parity-symmetric counterpart when the disorder was weak for any value of α. This resulted from the competition between the constructive interference from the boundaries and the destructive interference from the disorder. When the array had periodic boundary conditions, light localized at the initial waveguide and the parity-symmetric waveguide as well as the anti-podal waveguides. In addition, the coupling between waveguides $j = N$ and $j = 1$ tuned the relative heights of the peaks in the steady state intensity profile. When a non-Hermitian but parity-symmetric disorder was introduced into the array, it was found that it preserved symmetry of the energy spectrum as the Hamiltonian was $\mathcal{PT}$-symmetric. Lastly, the quantum statistics of the output intensity were investigated for a thermal field, coherent field, and a single-mode, squeezed field. The normalized fluctuations in the output inten-

sity increased with intensity as the system underwent a phase transition from a clean system to a system with strong disorder. The entropy of the system indicated the phase transition that took place as it went through a maximum. In addition to the increased fluctuations, the site-to-site correlations showed that the light underwent superbunching as it localized.

LIST OF REFERENCES

LIST OF REFERENCES

[1] J. C. Slater and G. F. Koster, "Simplified lcao method for the periodic potential problem," *Phys.Rev.*, vol. 94, no. 6, pp. 1498–1524, 1954.

[2] N. Ashcroft and N. Mermin, *Solid State Physics*. Saunders College, 1976.

[3] H. S. Eisenberg, Y. Silberberg, R. Morandotti, and J. S. Aitchison, "Diffraction management," *Phys. Rev. Lett.*, vol. 85, no. 9, pp. 1863–1866, 2000.

[4] A. L. Jones, "Coupling of optical fibers and scattering in fibers," *J. Opt. Soc. Am.*, vol. 55, no. 3, pp. 261–269, 1965.

[5] J. D. Jackson, *Classical Electrodynamics*. New York: Wiley, third ed., 1999.

[6] B. Saleh and M. Teich, *Fundamentals of photonics*. Wiley, second ed., 2007.

[7] V. Gantmakher, *Electrons And Disorder in Solids*. Oxford University Press, 2005.

[8] S. Datta, *Electronic Transport in Mesoscopic Systems*. Cambridge University Press, 1997.

[9] M. Segev, Y. Silberberg, and D. N. Christodoulides, "Anderson localization of light," *Nat Photon*, vol. 7, no. 3, pp. 197–204, 2013.

[10] M. Di Ventra, *Electrical transport in nanoscale systems*. Cambridge University Press, 2008.

[11] C. M. Bender and S. Boettcher, "Real spectra in non-hermitian hamiltonians having pt symmetry," *Phys. Rev. Lett.*, vol. 80, no. 24, p. 5243, 1998.

[12] C. M. Bender, "Making sense of non-hermitian hamiltonians," *Rep. Prog. Phys.*, vol. 70, no. 6, p. 947, 2007.

[13] C. M. Bender, D. C. Brody, and H. F. Jones, "Complex extension of quantum mechanics," *Phys. Rev. Lett.*, vol. 89, no. 27, p. 270401, 2002.

[14] A. Guo, G. J. Salamo, D. Duchesne, R. Morandotti, M. Volatier-Ravat, V. Aimez, G. A. Siviloglou, and D. N. Christodoulides, "Observation of pt-symmetry breaking in complex optical potentials," *Phys. Rev. Lett.*, vol. 103, no. 9, p. 093902, 2009.

[15] C. E. Rüter, K. G. Makris, R. El-Ganainy, D. N. Christodoulides, M. Segev, and D. Kip, "Observation of parity-time symmetry in optics," *Nat. Phys.*, vol. 6, no. 3, pp. 192–195, 2010.

[16] H. B. Perets, Y. Lahini, F. Pozzi, M. Sorel, R. Morandotti, and Y. Silberberg, "Realization of quantum walks with negligible decoherence in waveguide lattices," *Phys. Rev. Lett.*, vol. 100, no. 17, p. 170506, 2008.

[17] A. Peruzzo, M. Lobino, J. C. F. Matthews, N. Matsuda, A. Politi, K. Poulios, X.-Q. Zhou, Y. Lahini, N. Ismail, K. Wörhoff, Y. Bromberg, Y. Silberberg, M. G. Thompson, and J. L. OBrien, "Quantum walks of correlated photons," *Science*, vol. 329, no. 5998, pp. 1500–1503, 2010.

[18] J. Kempe, "Quantum random walks: An introductory overview," *Contemp. Phys.*, vol. 44, no. 4, pp. 307–327, 2003.

[19] P. Biagioni, G. Della Valle, M. Ornigotti, M. Finazzi, L. Du, P. Laporta, and S. Longhi, "Experimental demonstration of the optical zeno effect by scanning tunneling optical microscopy," *Opt. Express*, vol. 16, no. 6, pp. 3762–3767, 2008.

[20] H. Trompeter, T. Pertsch, F. Lederer, D. Michaelis, U. Streppel, A. Bräuer, and U. Peschel, "Visual observation of zener tunneling," *Phys. Rev.Lett.*, vol. 96, p. 023901, Jan 2006.

[21] C. Zener, "A theory of the electrical breakdown of solid dielectrics," *Proc. R. Soc. Lond. A*, vol. 145, no. 855, pp. 523–529, 1934.

[22] K. Fang, Z. Yu, and S. Fan, "Photonic aharonov-bohm effect based on dynamic modulation," *Phys. Rev. Lett.*, vol. 108, no. 15, p. 153901, 2012.

[23] E. Akkermans and G. Montambaux, *Mesoscopic Physics of Electrons and Photons*. Cambridge University Press, 2007.

[24] S. Longhi, "Photonic analog of zitterbewegung in binary waveguide arrays," *Opt. Lett.*, vol. 35, no. 2, pp. 235–237, 2010.

[25] H. M. Pilkuhn, *Relativistic Quantum Mechanics*. New York: Springer, 2003.

[26] K. Huang, "On the zitterbewegung of the dirac electron," *Am. J. Phys.*, vol. 20, no. 8, pp. 479–484, 1952.

[27] F. Bloch, "Über die quantenmechanik der elektronen in kristallgittern," *Z. Phys.*, vol. 52, no. 7, pp. 555–600, 1929.

[28] U. Peschel, T. Pertsch, and F. Lederer, "Optical bloch oscillations in waveguide arrays," *Opt. Lett.*, vol. 23, no. 21, pp. 1701–1703, 1998.

[29] D. N. Christodoulides and R. I. Joseph, "Discrete self-focusing in nonlinear arrays of coupled waveguides," *Opt. Lett.*, vol. 13, no. 9, pp. 794–796, 1988.

[30] H. S. Eisenberg, Y. Silberberg, R. Morandotti, A. R. Boyd, and J. S. Aitchison, "Discrete spatial optical solitons in waveguide arrays," *Phys. Rev. Lett.*, vol. 81, pp. 3383–3386, Oct 1998.

[31] R. Morandotti, U. Peschel, J. S. Aitchison, H. S. Eisenberg, and Y. Silberberg, "Dynamics of discrete solitons in optical waveguide arrays," *Phys. Rev. Lett.*, vol. 83, no. 14, pp. 2726–2729, 1999.

[32] Y. V. Bludov, V. V. Konotop, and N. Akhmediev, "Rogue waves as spatial energy concentrators in arrays of nonlinear waveguides," *Opt. Lett.*, vol. 34, no. 19, pp. 3015–3017, 2009.

[33] Y. Lahini, E. Frumker, Y. Silberberg, S. Droulias, K. Hizanidis, R. Morandotti, and D. N. Christodoulides, "Discrete x-wave formation in nonlinear waveguide arrays," *Phys. Rev. Lett.*, vol. 98, no. 2, p. 023901, 2007.

[34] M. V. Smoluchowski, "Experimentell nachweisbare, der Üblichen thermodynamik widersprechende molekularphenomene," *Phys. Z.*, vol. 13, pp. 1069–1080, 1912.

[35] R. Feynman, R. Leighton, and M. Sands, *The Feynman Lectures on Physics*, vol. 1. Boston: Addison-Wesley, second ed., 1963.

[36] R. D. Astumian, "Thermodynamics and kinetics of a brownian motor," *Science*, vol. 276, no. 5314, pp. 917–922, 1997.

[37] M. O. Magnasco, "Forced thermal ratchets," *Phys. Rev. Lett.*, vol. 71, no. 10, pp. 1477–1481, 1993.

[38] M. Bier, "Brownian ratchets in physics and biology," *Contemp. Phys.*, vol. 38, no. 6, pp. 371–379, 1997.

[39] J. S. Bader, M. W. Deem, R. W. Hammond, S. A. Henck, J. W. Simpson, and J. M. Rothberg, "A brownian-ratchet dna pump with applications to single-nucleotide polymorphism genotyping," *Appl. Phys. A*, vol. 75, no. 2, pp. 275–278, 2002.

[40] P. Reimann, M. Grifoni, and P. Hänggi, "Quantum ratchets," *Phys. Rev. Lett.*, vol. 79, pp. 10–13, Jul 1997.

[41] V. Ramareddy, *Quantum chaos using delta kicked systems.* PhD thesis, Oklahoma State University, 2008.

[42] H. Linke, T. E. Humphrey, A. Löfgren, A. O. Sushkov, R. Newbury, R. P. Taylor, and P. Omling, "Experimental tunneling ratchets," *Science*, vol. 286, no. 5448, pp. 2314–2317, 1999.

[43] I. Dana, V. Ramareddy, I. Talukdar, and G. S. Summy, "Experimental realization of quantum-resonance ratchets at arbitrary quasimomenta," *Phys. Rev. Lett.*, vol. 100, no. 2, p. 024103, 2008.

[44] A. Rai, G. S. Agarwal, and J. H. H. Perk, "Transport and quantum walk of nonclassical light in coupled waveguides," *Phys. Rev. A*, vol. 78, no. 4, p. 042304, 2008.

[45] A. Perez-Leija, H. Moya-Cessa, A. Szameit, and D. N. Christodoulides, "Glauber-fock photonic lattices," *Opt. Lett.*, vol. 35, no. 14, pp. 2409–2411, 2010.

[46] Y. N. Joglekar and A. Saxena, "Robust pt-symmetric chain and properties of its hermitian counterpart," *Phys. Rev. A*, vol. 83, no. 5, p. 050101, 2011.

[47] M. Bellec, G. M. Nikolopoulos, and S. Tzortzakis, "Faithful communication hamiltonian in photonic lattices," *Opt. Lett.*, vol. 37, no. 21, pp. 4504–4506, 2012.

[48] S. Longhi, "Periodic wave packet reconstruction in truncated tight-binding lattices," *Phys. Rev. B*, vol. 82, no. 4, p. 041106, 2010.

[49] A. Szameit, Y. V. Kartashov, P. Zeil, F. Dreisow, M. Heinrich, R. Keil, S. Nolte, A. Tnnermann, V. A. Vysloukh, and L. Torner, "Wave localization at the boundary of disordered photonic lattices," *Opt. Lett.*, vol. 35, no. 8, pp. 1172–1174, 2010.

[50] K. G. Makris and D. N. Christodoulides, "Method of images in optical discrete systems," *Phys. Rev. E*, vol. 73, no. 3, p. 036616, 2006.

[51] R. Loudon, *The Quantum Theory of Light*. Oxford University Press, third ed., 2000.

[52] Y. Bromberg, Y. Lahini, R. Morandotti, and Y. Silberberg, "Quantum and classical correlations in waveguide lattices," *Phys. Rev. Lett.*, vol. 102, no. 25, p. 253904, 2009.

[53] R. Hanbury Brown and R. Q. Twiss, "A test of a new type of stellar interferometer on sirius," *Nature*, vol. 178, no. 4541, pp. 1046–1048, 1956.

[54] A. Fox, *Quantum Optics: An Introduction*. Oxford master series in physics, Oxford University Press, 2006.

[55] P. Drude, "Zur elektronentheorie der metalle," *Ann. Phys.*, vol. 306, no. 3, pp. 566–613, 1900.

[56] A. Ioffe and A. Regel, "Non-crystalline, amorphous and liquid electronic semiconductors," *Prog. Semicond.*, vol. 4, pp. 237–291, 1960.

[57] E. Abrahams, P. W. Anderson, D. C. Licciardello, and T. V. Ramakrishnan, "Scaling theory of localization: Absence of quantum diffusion in two dimensions," *Phys. Rev. Lett.*, vol. 42, no. 10, pp. 673–676, 1979.

[58] P. A. Lee and T. V. Ramakrishnan, "Disordered electronic systems," *Rev. Mod. Phys.*, vol. 57, pp. 287–337, Apr 1985.

[59] P. W. Anderson, "Absence of diffusion in certain random lattices," *Phys. Rev.*, vol. 109, no. 5, pp. 1492–1505, 1958.

[60] A. Amir, Y. Lahini, and H. B. Perets, "Classical diffusion of a quantum particle in a noisy environment," *Phys. Rev. E*, vol. 79, p. 050105, May 2009.

[61] L. Levi, T. Schwartz, M. Segev, and S. Fishman, "Breakdown of anderson localization due to dynamic disorder," in *Conference on Lasers and Electro-Optics/International Quantum Electronics Conference*, p. IThD2, 2009.

[62] A. Lagendijk, B. van Tiggelen, and D. S. Wiersma, "Fifty-years of anderson localization," *Phys. Today*, vol. 62, pp. 24–29, August 2009.

[63] R. L. Weaver, "Anderson localization of ultrasound," *Wave Motion*, vol. 12, no. 2, pp. 129–142, 1990.

[64] A. Aspect and M. Inguscio, "Anderson localization of ultracold atoms," *Physics Today*, vol. 62, no. 8, pp. 30–35, 2009.

[65] S. John, "Strong localization of photons in certain disordered dielectric superlattices," *Phys. Rev. Lett.*, vol. 58, no. 23, p. 2486, 1987.

[66] S. John, "Localization of light," *Phys. Today*, vol. 44, pp. 32–40, 1991.

[67] Y. Lahini, A. Avidan, F. Pozzi, M. Sorel, R. Morandotti, D. N. Christodoulides, and Y. Silberberg, "Anderson localization and nonlinearity in one-dimensional disordered photonic lattices," *Phys. Rev. Lett.*, vol. 100, no. 1, p. 013906, 2008.

[68] Y. Lahini, Y. Bromberg, Y. Shechtman, A. Szameit, D. N. Christodoulides, R. Morandotti, and Y. Silberberg, "Hanbury brown and twiss correlations of anderson localized waves," *Phys. Rev. A*, vol. 84, no. 4, p. 041806, 2011.

[69] G. E. P. Box and M. E. Muller, "A note on the generation of random normal deviates," *Ann. Math. Stat.*, vol. 29, no. 2, pp. 610–611, 1958.

[70] Y. Bromberg, Y. Lahini, and Y. Silberberg, "Bloch oscillations of path-entangled photons," *Phys. Rev. Lett.*, vol. 105, no. 26, p. 263604, 2010.

[71] Y. Lahini, Y. Bromberg, D. N. Christodoulides, and Y. Silberberg, "Quantum correlations in two-particle anderson localization," *Phys. Rev. Lett.*, vol. 105, no. 16, p. 163905, 2010.

[72] K. G. Makris, R. El-Ganainy, D. N. Christodoulides, and Z. H. Musslimani, "Beam dynamics in $\mathcal{PT}$ symmetric optical lattices," *Phys. Rev. Lett.*, vol. 100, no. 10, p. 103904, 2008.

[73] T. Kottos, "Optical physics: Broken symmetry makes light work," *Nat. Phys.*, vol. 6, no. 3, pp. 166–167, 2010.

[74] D. D. Scott and Y. N. Joglekar, "Degrees and signatures of broken $\mathcal{PT}$ symmetry in nonuniform lattices," *Phys. Rev. A*, vol. 83, p. 050102, 2011.

[75] Y. N. Joglekar, "Mapping between hamiltonians with attractive and repulsive potentials on a lattice," *Phys. Rev. A*, vol. 82, no. 4, p. 044101, 2010.

[76] R. J. Glauber, "The quantum theory of optical coherence," *Phys. Rev.*, vol. 130, no. 6, p. 2529, 1963.

[77] L. Sapienza, H. Thyrrestrup, S. Stobbe, P. D. Garcia, S. Smolka, and P. Lodahl, "Cavity quantum electrodynamics with anderson-localized modes," *Science*, vol. 327, no. 5971, pp. 1352–1355, 2010.

[78] T. M. Cover and J. A. Thomas, *Elements of information theory*. Wiley, second ed., 2012.

[79] L. Landau and E. Lifshitz, *Statistical Physics*. Course of Theoretical Physics, Elsevier Science, 1996.

[80] X. Jia, A. R. Subramaniam, I. A. Gruzberg, and S. Chakravarty, "Entanglement entropy and multifractality at localization transitions," *Phys. Rev. B*, vol. 77, no. 1, p. 014208, 2008.

[81] J. A. Rice, *Mathematical statistics and data analysis*. Duxbury Press, 1995.

[82] M. Stoytchev and A. Z. Genack, "Measurement of the probability distribution of total transmission in random waveguides," *Phys. Rev. Lett.*, vol. 79, p. 309, 1997.

APPENDIX

APPENDIX

```
%fast - A fast program to simulate quantum walking
    clear all, help fast; % Clear memory and print header
    tic; % Start timer
    %*********************************************************************
    %* Open and read value for different values of D and alpha
    fid = fopen('delta.txt','r'); % Opens delta file for reading
    VD = fscanf(fid, '%g %g', [1, inf]);% Reads in data as one row
    fclose(fid); % Closes file
    LD = length(VD); % Obtains total number of values for D
    fid1 = fopen('alpha.txt','r'); % Opens alpha file for reading
    VD1 = fscanf(fid1, '%g %g',[1,inf]); % Reads in data as one row
    fclose(fid1); %Closes file
    AD = length(VD1); % Obtains number of values for alpha
    %*********************************************************************
    % Program Options
    Bdistr = 3; % =1 for constant, =2 for Rectangular, =3 for Gaussian, =4 for
a linear ramp, =5 for PT symmetric impurities, =6 triangle form, =7 for periodic
potential, =8 for long-range correlated disorder
    BStat = 2; % =1 if values of B are to be stored for statistical analysis, =2 otherwise
    Cdistr = 1; % =1 for constant, =2 for Rectangular, =3 for Gaussian, =4 for parity
symmetry, =5 for Glauber-Fock lattice, =6 random parity symmetry
    CStat = 2; % =1 if values of C are to be stored for statistical analysis, =2 otherwise
    field = 2; % =1 for thermal, =2 for coherent, =3 for squeezed, and =4 for electron
```

```
BWStat = 2; % =1 for bandwidth values to be stored for statistical analysis, =2 otherwise
NI = 1; % Number of particles input, 1 or 2
Timescale = 1; % =1 for normalized time scale, =2 for unnormalized time scale
ND = 1; % =1 for Normalized Disorder, =2 otherwise
PT = 2; % Type of particle, = 1 for bosons and =2 for fermions
NS = 2; % = 1 if a NOON state, 2 otherwise
STS = 2; % =1 to calculate site-to-site corr. =2 if not desired
QuCorr = 2; % =1 to calculate, =2 if calculation not desired
HBT = 2; % =1 to calculate, =2 if calculation not desired
NormHBT = 2; % =1 to normalize HBT, =2 otherwise
Ratchet = 2; % =1 for rachet data, =2 if not desired
HIST = 2; % =1 for intensity histogram, =2 if not desired
CalcG = 2; % =1 to sum over diagonals in HBT matrix, =2 otherwise
Entropy = 2; % =1 to calculate, =2 otherwise
Periodic = 2; % =1 for periodic boundary conditions, =2 for closed boundary conditions
FFT = 2; % =1 to calculate FFT of intensity at initial site, =2 otherwise
IPR = 2; % =1 to calculate inverse population ratio, =2 otherwise
Movie = 2; % =1 to make movie on STS, =2 otherwise
%**************************************************************************
% Safety conditional to ensure proper flags are tripped
if(CalcG==1)
HBT=1;
NormHBT=1;
end
if(HBT==2)
NormHBT=2;
CalcG=2;
```

```
end
if(Bdistr==1||Bdistr==6||Bdistr==7)
ND=2;
end
%**************************************************************************
% Initialize parameters (step size, coefficients, etc.)
frac = 5000; % Normalized propagation distance
npoints = 5000; % Number of points to record
CA = 1; % Tunneling rate between two adjacent sites
BA = 0; % Average value of beta, value does not change spread
N = 20; % Number of waveguides
NA = 1.e0; % Number of times to run program
if(Bdistr==2||Bdistr==3||Bdistr==5||Bdistr==8||Cdistr==2||Cdistr==3||Cdistr==6)
NA=1.e3; % # of realizations
end
nbar = 1.e0; % Average number of Photons
gamma = 1.e-1; % PT-symmetric potential
LB = 1; % Lower bound for PT-symmetric impurities
UB = floor(N/2); % Upper bound for PT-symmtric impurities
Dell= 0.01; % Defines range of distribution for random parity symmetric tunneling
rho = 0; % Used for long-range correlated disorder
CN = 1; % Coupling coefficient between waveguide N and waveguide 1
%r = asinh(sqrt(nbar)); % Squeezing parameter
%**************************************************************************
% Initial Position and phase difference
po1 = 3; % Position of first photon
po2 = 2; % Position of second photon
angle = 217; % Angle in degrees
phi = (angle/180)*pi; % Phase difference of two inputs
```

```
rf = 1.e-2; % Slope of linear ramp for Bdistr and Cdistr
%*************************************************************************
% Initialize Global Storage vectors
G2=zeros(1,LD);
Var=zeros(1,LD);
S = zeros(npoints+1,LD);
if(BWStat==1)
BW=zeros(1,NA);
end
if(BStat==1)
BB=zeros(1,N);
end
if(CStat==1)
CC=zeros(1,NA*N);
end
if AD>LD
II=zeros(1,AD);
else
II=zeros(1,LD);
II1=zeros(1,LD);
end
if(FFT==1)
IFFT= zeros(1,npoints);
end
if(Ratchet==1)
guide = zeros(1,N);
end
%*************************************************************************
% Determine coefficients for field averages
```

```
if(field == 1)
coeff1 = 2*(nbar^2);
coeff2 = nbar;
end
if(field == 2)
coeff1 = nbar^2;
coeff2 = nbar;
end
if(field==3)
coeff1 = (sinh(r)^2)*(1+3*(sinh(r)^2));
coeff2 = sinh(r)^2;
end
if(field == 4)
coeff1 = 1;
coeff2 = 1;
end
if(field>4)
fprintf('Intensities are incorrect\n');
end
%**************************************************************************
% Repeat Program for Various Values of D
for qq=1:AD
for q=1:LD
De = VD(q);
alpha= VD1(qq);
% Create output files
%mytable1 = fopen(['6test.txt'],'wt'); % Labels output files with proper D value
if(HIST==1)
```

```
mytable2 = fopen([num2str(alpha),'HIST',num2str(De),'.txt'],'wt'); % Histogram
file
end
if(Ratchet==1)
mytable3 = fopen([num2str(angle),'Ratchetgamma','.txt'],'wt'); %Ratchet data
file
end
if(AD||LD>1)
% mytable4 = fopen(['Figure0','.txt'],'wt');
end
if(Entropy==1)
%mytable5 = fopen('ENTROPY.txt','wt');
end
% Initialize storage vector
C = zeros(1,N); % Coupling Constants
B = zeros(1,N); % On-site Eigen values
A0 = zeros(N,1); % Initial state of first photon
AA0 = zeros(N,1); % Initial state of second photon
A = zeros(N,1); % Amplitude of states for first photon
A1 = zeros(N,N);
AA = zeros(N,1); % Amplitude of states for second photon
ave=zeros(1,N); % Initialize temporary storage vector
GPlot = zeros(1,N); % Initialize temporary storage vector
T = zeros(1,N); % Initialize temporary storage vector
M = zeros(1,N); % Initialize temporary storage vector
Y = zeros(1,N); % Initialize temporary storage vector
YPlot = zeros(1,N); % Initialize temporary storage vector
G = zeros(1,N); % Initialize temporary storage vector
R = zeros(1,npoints+1); % Initialize IPR vector
```

```
Z = zeros(1,N); % Initialize temporary storage vector
Q = zeros(1,N); % Initialize temporary storage vector
QQ = zeros(1,N); % Initialize temporarty storage vector
PP = zeros(1,N); % Initialize temporary storage vector
PPP = zeros(1,N); % Initialize temporary storage vector
G1 = zeros(1,N); % Initialize temporary storage vector
I = zeros(1,N); %Initialize temporary storage vector
g = zeros(1,2*N-1);
S1 = zeros(1,N); % Initialize temporary storage vector
T1 = zeros(1,N); % Initialize temporary storage vector
A3 = zeros(1,N); % Initialize temporary storage vector
IP = zeros(1,N); % Initialize temporary storage vector
IP2 = zeros(1,N-2); % Initialize temporary storage vector
IPlot = zeros(N,N); % Initialize Correlation matrix
IPlot1 = zeros(N,N); % Initialize Correlation matrix for two photons
IPlot2 = zeros(N,N); % Initialize Correlation matrix for two photons
IPlot2A = zeros(N,N); % Initialize temporary storage vector
IJR = zeros(npoints,1); % Storage used for rachet effect examination
IJ = zeros(N,npoints+1);
VPP = zeros(1,N); % Variance vector for total intensity with two photons
VNPP = zeros(1,N); % Normalized variance vector for total intensity with two
photons
H = zeros(N,N); % Hamiltonian
guide = zeros(1,N);
gn = zeros(1,N);
Energy = zeros(1,npoints+1);
Momentum = zeros(1,npoints+1);
pos_var = zeros(1,npoints+1);
time = zeros(npoints+1,1); % Used to record time for plotting ratchet
```

```
hplot = zeros(1,NA); % Used for histogram
Intensity = zeros(npoints+1,1);
if(Movie==1)
STSPlot=zeros(N,N,npoints);
end
%*****************************************************************
% Main Loop
for x=1:NA
t=0; % Start every run at t =0;
%Create Beta and couppling vectors
if (x<2||Bdistr==2||Bdistr==3||Bdistr==5)% Only recreate vectors if they are random or this is first realization
for ii=1:N
a = rand(); % Uniformly Distributed
b = rand(); % Uniformly Distributed
if (Bdistr==1)
B(ii) = BA ; % Constant
end
if (Bdistr==2)
B(ii) = BA + De*(-1+(2*a)); % Rectangular distribution
end
if(Bdistr==3)
B(ii) = BA + De*sqrt(-2*log(a))*cos(2*pi*b);% Gaussian distribution
end
if(Bdistr==4)
B(ii)=rf*(-13+ii);
end
if(Bdistr==5)
a=rand();
```

```
if(ii<=UB&&ii>=LB)
%B(ii)=sqrt(-1)*gamma*(-1+2*a);
%B(ii)=((-1)^ii)*sqrt(-1)*gamma;
B(ii)=sqrt(-1)*sin(2*pi*ii/(N+1));
if(ii<=N/2)
B(N+1-ii)=-B(ii);
end
end
end
if(Bdistr==6)
if(ii<(N+1)/2)
B(ii)=-ii;
B(N+1-ii)=B(ii);
end
end
if(Bdistr==7)
B(ii)=cos(pi*(sqrt(5)+1)*ii);
end
if(Bdistr==8)
for k=1:N/2
B(ii)=(sqrt(k^(-rho)*(2*pi/N)^(1-rho))*cos(2*pi*ii*k/N+2*pi*rand()))+B(ii);
end
end
if (Cdistr==1)
C(ii) = CA ; % Constant
end
if (Cdistr==2)
C(ii) = CA + De*(-1+(2*a)); % Rectangular distribution
end
```

```
if(Cdistr==3)
C(ii) = CA + De*sqrt(-2*log(a))*cos(2*pi*b); % Gaussian distribution
end
if(Cdistr==4)
C(ii)=CA*((ii)*(N-ii))^(0.5*alpha); % Non-hermitian mapping
C(N)=0;
end
if(Cdistr==5)
C(ii)=sqrt(ii); % Glauber-Fock lattice
end
if(Cdistr==6)
if(ii<=N/2)
CA = (1-Dell)+2*Dell*a;
C(ii)= CA*(ii*(N-ii))^(0.5*alpha);
C(N-ii)=C(ii);
end
end
%Label waveguides for ratchet and apply linear gradient to beta
if(Ratchet==1)
guide(ii) = -13+ii;
end
end
end
%Boundary Conditions
A0(po1)=1;
if(NI==2)
AA0(po2)=1;
end
for j=1:N
```

```
IJ(j,1)=((A0(j)+AA0(j))^2)/(NI*NA)+IJ(j,1);
end
if(NI>2)
fprintf('Incorrect number of particles input')
break
end
%Put in break so that program terminates if distr >2
if(or(Bdistr,Cdistr)>7)
fprintf('Bdistr or C distr >7\n')
break
end
% Create disorder-free Hamiltonian
for i=1:N
for j=1:N
if (i==j)
H(i,j)= BA;
elseif(or(i+1==j,i-1==j))
CDF=C(i);
H(i,j)=CDF;
H(j,i)=CDF;
end
if(Periodic==1)
if(i==N)
theta = 0*pi;
H(1,i)=CN*CA*exp(sqrt(-1)*theta);
H(i,1)=CN*CA*exp(sqrt(-1)*theta);
end
end
end
```

```
end
% Find eigenvalues and eigenvectors
[V,D] = eig(H);
bw0 = max(max(D))-min(min(D));
%A0=VV(15,:)';
%Create Hamiltonian
if(ND==2)
for i=1:N
for j=1:N
if (i==j)
H(i,j)= B(i);
if(BStat==1)
BB(i)=B(i)/NA+BB(i);
end
else
H(i,j)= 0;
end
if(or(i+1==j,i-1==j))
H(i,j)=C(j);
H(j,i)=C(j);
end
end
end
% Apply periodic boundary conditions if desired
if(Periodic==1)
if(i==N)
theta = 0*pi;
H(1,i)=CN*CA*exp(sqrt(-1)*theta);
H(i,1)=CN*CA*exp(sqrt(-1)*theta);
```

```
end
end
% Find proper eigenvectors
[V,D] = eig(H);
end
% Normalize disorder
if (ND==1)
De1=bw0*De;
for i=1:N
a = rand();
b = rand();
if (Bdistr==2)
B(i) = BA + De1*(-1+(2*a)); % Rectangular distribution
end
if(Bdistr==3)
B(i) = BA + De1*sqrt(-2*log(a))*cos(2*pi*b); % Gaussian distribution
end
if(Bdistr==5)
if(i<=UB&&i>=LB)
B(i)=sqrt(-1)*gamma*(-1+2*a)*De1;
%B(i)=sqrt(-1)*gamma;
if(i<=N/2)
B(N+1-i)=-1*B(i);
end
end
end
if(BStat==1)
BB(i)=B(i)/NA+1;
end
```

```
end
for i=1:N
for j=1:N
if (i==j)
H(i,j)= B(i);
elseif(or(i+1==j,i-1==j))
H(i,j)=C(j);
H(j,i)=C(j);
end
end
% Apply periodic boundary conditions if desired
if(Periodic==1)
if(i==N)
theta=0*pi;
H(1,i)=CN*exp(sqrt(-1)*theta);
H(i,1)=CN*exp(sqrt(-1)*theta);
end
end
end
[V,D] = eig(H);
end
bw = max(diag(D))-min(diag(D));
if(BWStat==1)
BW(x)=bw;
end
if(x<2)
for i=1:N
Intensity(1) = ((abs(A0(i)+exp(sqrt(-1)*phi)*AA0(i))^2))/NI+Intensity(1);
R(1)= (abs(A0(i))^4)+R(1);
```

```
if(Ratchet==1)
time(1)=0;
Momentum(1) = (abs(A0(i)+exp(sqrt(-1)*phi)*AA0(i))^2)*guide(i)+Momentum(1);
Energy(1) = (abs(A0(i)+exp(sqrt(-1)*phi)*AA0(i))^2)*((guide(i))^2)+Momentum(1);
pos_var(1) = Energy(1)-Momentum(1)^2;
end
end
end
t=0; %Initialize time
for istep=1:npoints
if(Timescale==1)
dt =(1/bw0)*(frac/npoints);
t = (dt + t);
time(istep+1)= t;
end
if(Timescale==2)
dt = (frac/npoints);
t = dt + t;
time(istep+1)=t;
end
for i=1:N
for j=1:N
if(i==j)
A1(i,i)=exp(-1*sqrt(-1)*D(i,i)*t);
else
A1(i,j)=0;
end
end
end
```

```
% Apply Evolution Operator
A=V*A1*V'*A0;
AA=V*A1*V'*AA0;
I=0;
for i=1:N
I=(abs(A(i)+exp(sqrt(-1)*phi)*AA(i))^2)+I;
end
for i=1:N
Intensity(istep+1) = (abs(A(i)+exp(sqrt(-1)*phi)*AA(i))^2)/(NI*NA)+Intensity(istep+1);
IJ(i,istep+1) = (abs(A(i)+exp(sqrt(-1)*phi)*AA(i))^2)/(NA*NI*I)+IJ(i,istep+1);
IJR(istep)=IJR(istep)+(-51+i)*(abs(A(i)+exp(sqrt(-1)*phi)*AA(i))^2);
if(IPR==1)
R(istep+1) = (abs(A(i))^4)/NA+R(istep+1);
end
if(Movie==1)
for q=1:N
STSPlot(i,q,istep)=STSPlot(i,q,istep)+(coeff2^2)*(abs(A(i)^2)*(abs(A(q))^2))/NA;
end
end
if(Ratchet==1)
Momentum(istep+1) = (abs(A(i)+exp(sqrt(-1)*phi)*AA(i))^2)*guide(i)+Momentum(istep+1);
Energy(istep+1) = (abs(A(i)+exp(sqrt(-1)*phi)*AA(i))^2)*((guide(i))^2)+Energy(istep+1);
if(x==NA)
pos_var(istep+1) = Energy(istep+1)-Momentum(istep+1)^2;
end
end
end
if(Entropy==1);
for i=1:N
```

```
if(IJ(j,istep+1)~=1 && IJ(j,istep+1)~=0)
S(istep+1,q)=S(istep+1,q)-(IJ(i,istep+1).*log(IJ(i,istep+1))-(1-IJ(i,istep+1)).*log(1-
IJ(i,istep+1)))/NA;
end
end
end
if(FFT==1)
IFFT(istep)=abs(A(po1))^2;
end
end
if(STS==1)
for l=1:N
for p=1:N
IPlot(p,l)=IPlot(p,l)+(coeff2^2)*(abs(A(p)^2)*(abs(A(l))^2))/NA;
end
end
end
if(QuCorr==1)
for l=1:N
for p=1:N
if (PT==1)
if(NS==2)
if(po1==po2)
IPlot1(p,l)=IPlot1(p,l)+0.5*(coeff2^2)*(abs(A(p)*AA(l)+A(l)*AA(p))^2)/NA; %
0.5 come from normalization of wavefunction for two bosons at same input
else
IPlot1(p,l)=IPlot1(p,l)+(coeff2^2)*(abs(A(p)*AA(l)+A(l)*AA(p))^2)/NA; % Sym-
metric for Bosons
end
```

```
    end
    if(NS==1)
    IPlot1(p,l)=IPlot1(p,l)+1*(abs(A(p)*AA(l)+exp(sqrt(-1)*phi)*A(l)*AA(p))^2)/NA;
    end
    end
    if(PT==2)
    IPlot1(p,l)=IPlot1(p,l)+(coeff2^2)*(abs(A(p)*AA(l)-A(l)*AA(p))^2)/NA; % Anti-
symmetric for fermions
    end
    end
    end
    end
    if(HBT==1)
    for l=1:N
    for p=1:N
    IPlot2(p,l)= IPlot2(p,l)+((abs(A(p)*AA(l)+A(l)*AA(p))^2)+(abs(A(p)*A(l))^2)+(abs(AA(p)*
    end
    end
    end
    for n=1:N
    G(n) = (abs(A(n)+exp(sqrt(-1)*phi)*AA(n))^2)/(NA*NI)+G(n);% Put intensity
into storage vector
    %G(n) = (abs(A(n))^2)/NA+G(n);
    M(n) = (abs(A(n)+exp(sqrt(-1)*phi)*AA(n))^4)/NA+M(n); %Put inensity squared
into storage vector
    G1(n) = (abs(AA(n))^2)/NA+G1(n);% Put intensity into storage vector
    IP(n) = IP(n) + (abs(A(n)+A1(n))^2);
    GPlot(n) = G(n)/coeff2;
    end
```

```
if(HIST==1)
hplot(x)= abs(A(N+1-po1));
end
for k=1:N
PP(k) = PP(k)/NA;
PPP(k) = PPP(k)/NA;
IP(k) = IP(k)/NA;
Y(k) = M(k)-(G(k)^2); % Calculate the variance of each lattice point
YPlot(k) = Y(k)/(coeff2*coeff2);
IP2(k)= PP(k)/(PPP(k)^2);
VPP(k) = PP(k)-(PPP(k)^2);
VNPP(k) = VPP(k)/(PPP(k)^2);
Z(k) = sqrt(Y(k)); % Calculate the standard deviation of each lattice point
end
for k=1:N
Q(k) = Y(k)/(G(k)^2); % g2*
%I Var(I) g2*
%fprintf(mytable1, '%g %g %g \n',G(k),Y(k),Q(k)); % Print to file test.txt
end
end
if(NormHBT==1)
for p=1:N
for q=1:N
IPlot2A(p,q)=IPlot2(p,q)/(G(p)*G(q));
end
end
end
if(CalcG==1)
k=1;
```

```
for dr=(-N+1):(N-1)
for p=1:N
if(p+dr<N+1&&p+dr>0)
g(k)=IPlot2A(p,p+dr);
end
end
%fprintf(mytable1, '%g\n',g(k));
k=k+1;
end
end
%end
if(Entropy==1)
%Ent(qq)=sum(S);
end
if (LD>1)
II(q)=G(N+1-po1);
II1(q)=G(po1);
elseif (AD >1)
II(qq)=G(po1);
end
%dlmwrite([num2str(field),'ctest',num2str(D),'.txt'], IPlot)% Single photon correlation
%dlmwrite(['6two',num2str(0),'.txt'], IJ,'delimiter','\t') ;% Intensity Evolution
if(STS==1)
dlmwrite([num2str(alpha),'STSCdelta',num2str(De),'.txt'],IPlot,'delimiter','\t'); % Site-to-site corr.
end
if(HBT==1)
```

```
%dlmwrite([num2str(alpha),'HBTdelta',num2str(De),'.txt'], IJR,'delimiter','\t') %
HBT correlation
end
if(Ratchet==1)
for k=1:istep
fprintf(mytable3, '%g %g %g \n',time(k),Momentum(k),Energy(k)); % Print ratchet
file
end
fclose(mytable3);
end
if(HIST==1)
for k=1:NA
fprintf(mytable2, '%g\n',hplot(k)); % Print ratchet file
fclose(mytable2);
end
end
%dlmwrite([num2str(PT),'Time.txt'], time ,'delimiter','\t')
%dlmwrite('Zplot.txt',Zplot)
if (LD >1 && rem(q,ceil(.1*LD))==0)
fprintf('Finished %g out of %g delta values\n',q,LD)
end
if (AD >1 && rem(qq,AD)==0)
fprintf('Finished %g out of %g alpha values\n',qq,AD)
end
end
end
if (Entropy==1)
% L=length(Ent);
%for i=1:L
```

```
%fprintf(mytable5, '%g\n',Ent(i));
%end
end
if LD >1
%for p=1:LD
%fprintf(mytable4, '%g\n',II(p));
%end
end
if AD>1
for p=1:AD
fprintf(mytable4, '%g\n',II(p));
end
end
%*************************************************************************
% Calculate FFT
if(FFT==1)
NFFT = 2^nextpow2(npoints); % Next power of 2 from length L
Fs = 1/(dt); % Sampling frequeny
%* Creating temporary storage vectors
X=zeros(1,NFFT/2+1);
IIII=zeros(npoints,1);
%Subtract DC component from data
for i=1:npoints
IIII(i)=IFFT(1,i)-mean(IFFT(1,:));
end
%* Calculate the FFT
L = length(I);
Y = 2*abs(fft(IIII,NFFT))/L;
%* Calculate power spectrum
```

```
for i=1:(NFFT/2+1)
X(i)=abs(Y(i));
end
%*Creating frequency vector
f = Fs/2*linspace(0,1,NFFT/2+1);
end
%************************************************************************
% Make movie of STS
if(Movie==1)
figure('Renderer','zbuffer')
numframes=npoints;
M=moviein(numframes); % create the movie matrix
set(gca,'NextPlot','replacechildren')
for i=1:numframes
surf(STSPlot(:,:,i));
%colorbar
caxis([0 1]);
axis([0, N+1, 0, N+1, 0, 1]);
M(i)=getframe;
end
%Create movie
movie(M,1,7.5);
%Export movie to AVI format
mov=movie2avi(M,'movie.avi','compression','none','fps',10 );
mov=mov(M);
end
%************************************************************************
%* Close output stream
%fclose(mytable1);
```

```
if(Entropy==1)
% fclose(mytable5);
end
%fclose(mytable4);
% Print to file test.txt
%*************************************************************************
%Close g2 output file
%for q =1:LD
%fprintf(mytable4,'%g %g %g \n%',VD(q),G2(q),Var(q)); % Print g2 to file
%end
%fclose(mytable4);
% Stop timer and display time elasped
toc;
```

VITA

VITA

Clinton E. Thompson

EDUCATION

- **Ph.D. Physics** Purdue University, Indianapolis, IN, Expected: May 2014, DISSERTATION: *Quantum Physics Inspired Optical Effects in Evanescently Coupled Waveguides*
- **M.S. Physics** Purdue University, Indianapolis, IN, May 2010
- **B.S. Physics (Magna Cum Laude), Minor Mathematics** Indiana State University, Terre Haute, IN, May 2006

TEACHING EXPERIENCE

- **Indiana University-Purdue University Indianapolis , Indianapolis, IN (Aug. 2009 – present)** Taught introductory physics labs. Tutored undergraduate students. Assisted with introductory physics recitations.
- **Northern Illinois University, DeKalb, IL (Aug. 2006 – May 2008)** Taught and set-up equipment for introductory physics labs. Tutored undergraduate students.
- **Indiana State University, Terre Haute, IN (Sept. 2002 – May 2006)** Assisted lab instructors and set-up equipment for introductory physics labs. Tutored undergraduate students.

PUBLICATIONS

- Y. N. Joglekar, **C. Thompson**, D. D. Scott and G. Vemuri, "Optical waveguide arrays: quantum effects and PT symmetry breaking", Eur. Phys. J. App. Phys. **63**, 30001 (2013).
- **C. Thompson**, G. Vemuri, "Quantum Physics Inspired Optical Effects in Tight-Binding Lattices", in New Trend in Atomic, Molecular and Optical Physics 2013, Springer.
- **C. Thompson**, Y. N. Joglekar, G. Vemuri, "Disorder effects in tunable waveguide arrays with parity-symmetric tunneling", Phys. Rev. A **86**, 043822 (2012).
- **C. Thompson**, G. Vemuri, and G. S. Agarwal, "Quantum physics inspired optical effects in tight-binding lattices: Phase-controlled photonic transport", Phys. Rev. B **84**, 214302 (2011).
- Y. N. Joglekar, **C. Thompson**, and G. Vemuri, "Tunable waveguide lattices with nonuniform parity-symmetric tunneling", Phys. Rev. A **83**, 063817 (2011).
- **C. Thompson**, G. Vemuri, and G. S. Agarwal, "Anderson localization with second quantized fields in a coupled array of waveguides", Phys. Rev. A **82**, 053805 (2010).

PRESENTATIONS

- "Quantum Physics Inspired Optical Effects in Tight-Binding Lattices", *Oral Presentation*, United States Naval Research Laboratory, Washington DC, December 2013.
- "Quantum Physics Inspired Optical Effects in Tight-Binding Lattices", *Oral Presentation*, MIT Lincoln Laboratory, Lexington, MA, November 2013.
- "All-Optical Quantum Ratchet", *Oral Presentation,* Annual Meeting of the American Physical Science Division of Atomic, Molecular, and Optical Physics, Atlanta, GA, June 2011.

- "Quantized Statistical Aspects of Anderson Localization with Second Quantized Fields", *Oral Presentation,* Fall 2010 Meeting of the American Physical Society Prairie Section, Chicago, IL, November 2010.
- "Detection of a Sub-Threshold Signal by Addition of Noise", *Poster Presentation,* Fall 2010 Meeting of the American Physical Society Prairie Section, Chicago, IL, November 2010.
- "Space-Charge Limiting of a Photoinjected Electron Pulse", *Poster Presentation,* Spring 2006 Meeting of the American Physical Society Ohio Section, Detroit, MI, April 2006.

HONORS AND AWARDS

- Outstanding Physics Graduate Student, 2013
- Purdue Research Investment Fund Fellowship, August 2012 – present
- GAANN Fellowship, January 2009 – August 2012
- Outstanding Graduating Senior, 2006
- Outstanding Physics Teaching Assistant, 2005

PROFESSIONAL MEMBERSHIPS

- Optical Society of America, 2011-present
- American Physical Society, 2010-present